Measurement of the drift velocities of electrons and holes in high-ohmic <100> silicon

Master-Arbeit

von

Christian Scharf

Fachbereich Physik

Universität Hamburg

Februar 2014

1. Gutachter: Prof. Dr. Erika Garutti

2. Gutachter: Prof. Dr. Robert Klanner

Abstract

Measurements of the drift velocities of electrons and holes as a function of the electric field and the temperature in high-ohmic silicon of <100> crystal orientation are presented. Significant differences between our results and literature values are observed. A new parametrization of the mobility is introduced. Current transients of n-type pad diodes, generated by fast laser pulses, were investigated in order to determine the drift velocity of electrons and holes separately. Two diodes of high-ohmic silicon (1.5 kΩcm and 5.5 kΩcm) from different manufacturers were investigated as cross check. The drift velocities were determined at electric fields ranging from 5 kV/cm to 50 kV/cm at temperatures ranging from 233 K to 333 K. The mobility parameters were obtained by fitting a simulation of charge drift in silicon to the measurements. Using the convolution theorem the response function of the read-out circuit was determined with the Fourier transforms of the measurement and the simulation.

The simulated transient current pulses with the new mobility parametrization are consistent with the measured ones for the temperature and electric field range investigated here. Additionally, the mobility results from the fit are consistent with the mobility determined using the simpler time-of-flight method in the field range where this method is applicable. However, our measurements show a difference of up to 14 % to the <100> values by Canali et al. (1971). The difference to the <111> mobility parametrization by Jacoboni et al. (1977) is up to 24 % while this parametrization is widely used for simulations of the <100> direction due to the lack of data for <100> silicon.

Kurzfassung

Diese Arbeit befasst sich mit der Messung der Driftgeschwindigkeit von Elektronen und Löchern in Abhängigkeit von der Temperatur und dem elektrischen Feld in hochohmigem Silizium der Kristallorientierung <100>. Die Ergebnisse dieser Arbeit zeigen große Unterschiede zu Werten aus der Literatur. Eine neue Parametrisierung der Mobilität wird vorgestellt. Von kurzen Laserpulsen erzeugte Strom-Transienten von n-Typ Flächendioden wurden gemessen, um die Driftgeschwindigkeit von Elektronen und Löchern separat zu bestimmen. Zwei Dioden unterschiedlicher Hersteller aus hochohmigem (1.5 kΩcm und 5.5 kΩcm) Silizium wurden zum Vergleich untersucht. Die Driftgeschwindigkeit wurde für elektrische Felder zwischen 5 kV/cm und 50 kV/cm bei Temperaturen zwischen 233 K und 233 K bestimmt. Die Parameter der Mobilität wurden durch die Anpassung einer Simulation der Bewegung von Ladungsträgern im elektrischen Feld in Silizium an die Messungen bestimmt. Mithilfe des Faltungstheorems wurde die Antwortfunktion des Ausleseschaltkreises aus den Fouriertransformierten der Messung und der Simulation bestimmt.

Die simulierten und gemessenen Transienten stimmen bei allen untersuchten Temperaturen und elektrischen Feldern nahezu überein. In dem Feldbereich, in dem die einfachere Time-Of-Flight-Methode (Flugzeit-Methode) anwendbar ist, stimmen die Ergebnisse aus der Anpassung weitestgehend mit den Ergebnissen der Time-Of-Flight-Methode überein. Allerdings zeigen unsere Messungen eine Abweichung von bis zu 14 % zu den Messwerten von Canali et al. (1971) für die <100> Orientierung. Die Abweichung zu den Literaturwerten von Jacoboni et al. (1975) für die <111> Orientierung liegt bei bis zu 24 %, wobei diese Werte aufgrund der wenigen verfügbaren Daten in Simulationen meist auch für die <100> Orientierung genutzt werden.

Contents

Abstract iii

1. Introduction 1

2. Charge transport in silicon diodes 2
2.1. Silicon diodes 2
2.2. Charge transport 4
2.2.1. Generation of free charge carriers 4
2.2.2. Drift and diffusion 5

3. Experimental techniques 6
3.1. Test structures 6
3.2. The Transient Current Technique 7
3.2.1. Laser properties 8
3.2.2. Transient current pulses 9
3.2.3. Temperature control 10

4. Analysis 11
4.1. The time-of-flight method 11
4.2. Transient current pulse simulation 13
4.2.1. Initial charge distribution 14
4.2.2. The electric field 15
4.2.3. Signal formation 16
4.2.4. Read-out circuit convolution 17
4.2.5. Fitting 20

5. Results 22
5.1. Mobility parametrization 22
5.1.1. Parametrization in the literature 22
5.1.2. An approach to find a better description 23
5.1.2.1. The transport model 23
5.1.2.2. The new parametrization 25

5.1.3. Comparison with measurements 26
5.1.3.1. Modified parametrization for the mobility of holes . 26
5.1.3.2. Comparison of the drift velocities obtained from different sensors 28
5.1.3.3. Comparison of simulated and measured current pulse shapes 29
5.2. Temperature dependence 35
5.2.1. Single temperature results 35
5.2.2. Global fit results 35
5.2.3. Comparison with the literature values 38
5.3. Discussion 40
5.3.1. Sources of error 41

6. Conclusion **46**

A. Appendix **50**
A.1. Laser pulse time spectra 50
A.2. Correlation matrix 50
A.3. Current pulse shapes 50

List of Figures **65**

List of Tables **67**

Bibliography **68**

1. Introduction

In high energy physics (HEP) an essential part of the experiments are particle tracking detectors. State-of-the-art tracking detectors consist of several layers of highly segmented silicon devices, namely pixel and strip sensors. A charged particle moving through the tracking detector creates electron-hole pairs in the silicon. In an applied electric field the charge carriers drift to the read-out electrodes. A signal is generated and the layering as well as the high segmentation allow the reconstruction of the track of the charged particle. During their time of service the tracking detectors experience a very high particle fluence which damages the silicon. For HEP experiments the decrease of the charge carrier lifetimes of electrons and holes $\tau_{e,h}$, the change of the electric field $E(x)$, and the increase of the leakage current are the most severe consequences. Since $\tau_{e,h}$ decreases less charge is collected and, in interaction with the increasing leakage current, the signal-to-noise ratio decreases. In the search for radiation hard silicon sensors the effects of radiation damage on silicon have to be evaluated.

The original aim of this thesis was to separately determine $E(x)$ and $\tau_{e,h}(x)$ in irradiated silicon pad diodes as a function of the position, the temperature, and the applied bias voltage. Measured current transients were analyzed by fitting the parameters of a simulation of charge drift in silicon. Measurements on non-irradiated sensors were performed for a calibration of the simulation. However, large differences between the measurements and the simulation were observed. Finally it was realized that the literature drift velocity of electrons and holes for the <111> crystal orientation is not valid, despite being widely used, for the <100> orientation. The drift velocity for <100> crystal orientation is a fundamental property of silicon. Nonetheless, it is not well studied and quantified in the literature, and literature values yield significantly wrong results. Consequently, we investigated the carrier drift velocity in high-ohmic silicon of <100> orientation as a function of the electric field and the temperature in order to allow for precise simulations of <100> silicon devices. The drift velocity for high-ohmic silicon of <100> orientation is of particular interest for CMS [5] where this material is used for the tracking detector. The results of this thesis are a step towards achieving the original aim, the determination of $E(x)$ and $\tau_{e,h}(x)$ in irradiated silicon sensors.

2. Charge transport in silicon diodes

This chapter gives a short introduction to the principles of a p-n silicon diode and the drift and diffusion of charge carriers in silicon.

2.1. Silicon diodes

Silicon is a group IV element of the periodic table and an intrinsic semiconductor. The band gap of silicon is indirect with an energy of $E_g = 1.12\,\mathrm{eV}$ at $T = 300\,\mathrm{K}$. By introducing group III or V elements into the silicon crystal energy levels close to the energy of the valence or the conduction band are created ($\Delta E \approx 45\,\mathrm{meV}$ for silicon doped with phosphorus), a process called doping. Already at low temperatures the additional energy levels are ionized and the concentration of free charge carriers in the silicon crystal is changed. The concentration of free charge carriers in intrinsic silicon ($\sim 10^{10}\,\mathrm{cm}^{-3}$ at $T = 300\,\mathrm{K}$) is usually several orders of magnitude lower than the effective doping concentration $N_{eff} = |N_D - N_A|$. Therefore, the free charge carrier concentration in doped silicon is approximately N_{eff}. Here N_D denominates the concentration of donors (group V atoms) and N_A the concentration of acceptors (group III atoms). The majority charge carriers are electrons for n-type ($N_D > N_A$) and holes for p-type silicon ($N_D < N_A$).

If the doping of silicon changes rapidly from n-type to p-type, a space charge region is formed at the boundary, the so-called p-n junction. The free electrons of the n-type silicon and the free holes of the p-type silicon diffuse and combine until equilibrium is reached. Only the ionized doping atoms remain as fixed charges. Consequently, there are no free charge carriers in this region, and the region is also called depletion region (see Figure 2.1(a)). Because of the fixed charges (positive for n-type and negative for p-type) an electric field is present at the p-n junction (fig. 2.1(b)). The corresponding electrostatic potential is the built-in potential Ψ_{bi} (fig. 2.1(c)). The Fermi energy E_F is close to the valence band for the p-type region and close to the conduction band for the n-type region. Therefore, the valence and the conduction bands are bent at the p-n junction as shown in Figure 2.1(d).

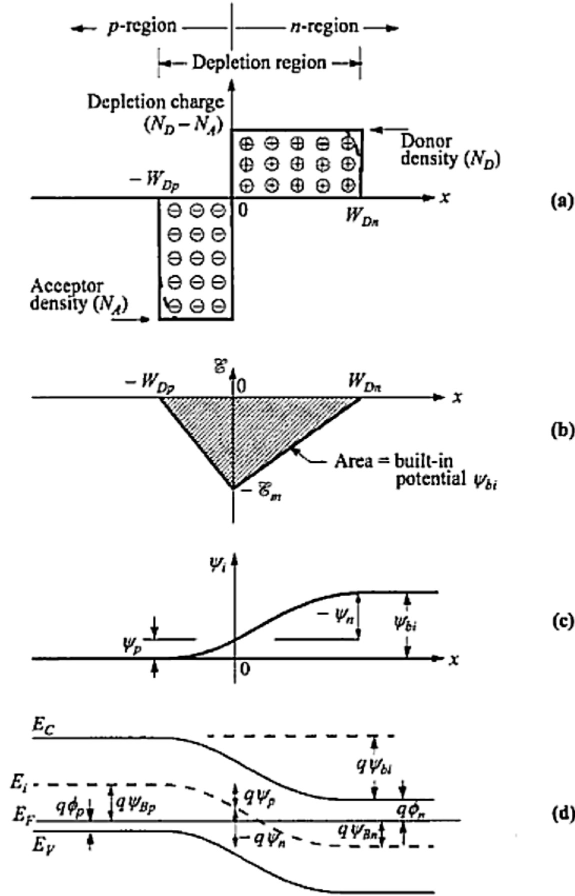

Figure 2.1.: An abrupt asymmetric p-n junction in thermal equilibrium. (a) dopant distribution, (b) field distribution, (c) potential variation, and (d) energy band diagram. Taken from [29].

A silicon diode is basically a p-n junction with two contacts. Application of an external bias voltage U_{bias} causes the depletion region to increase if the polarity of U_{bias} is + for the n-type part and − for the p-type part. This is called reverse bias. On the other hand, the depletion region decreases if the polarity is inverted. This is called forward bias. For reverse bias the electrical current is very low and is called leakage current.

For the detection of incident radiation an asymmetric junction is used (situation depicted in fig. 2.1). In this thesis p-on-n type silicon diodes were investigated, meaning a thin, highly doped p^+ layer (implant) is followed by the thick, lightly doped n-type bulk and a thin n^+ rear implant serving as a contact[1]. A reverse bias is applied causing the width of the depletion region in the n bulk W_{Dn} to increase. The width of the depletion region in the p^+ implant W_{Dp} stays very thin ($\frac{W_{Dp}}{W_{Dn}} = \frac{N_D}{N_A}$). Therefore, the p^+ implant is neglected in the following equations

[1]The $^+$ denominates high N_{eff}.

and N_{eff} denominates the constant effective doping concentration of the n bulk.

The Poisson equation is

$$\frac{d^2\Phi(x)}{dx^2} = -\frac{\rho}{\epsilon\epsilon_0} \tag{2.1}$$

with the space charge density $\rho = e_0 N_{eff}$, the relative permittivity $\epsilon \approx 11.7$ for silicon, the vacuum permittivity ϵ_0, and the elementary charge e_0. The electric field of the depletion zone is

$$E(x) = \frac{e_0 N_{eff}}{\epsilon\epsilon_0} \cdot (W_{Dn} - x) \tag{2.2}$$

using the boundary condition $E(x = W_{Dn}) = -\frac{d}{dx}\Phi(x = W_{Dn}) = 0$ (see fig. 2.1(b)). Integration of equation 2.2 yields the potential. For our measurements $U_{bias} \gg \Psi_{bi}$, so the built-in potential is neglected in the following. At the depletion voltage

$$U_{dep} = \frac{e_0 N_{eff} \cdot w^2}{2\epsilon\epsilon_0} \tag{2.3}$$

the whole n bulk is depleted and the width of the depletion region is $W_{Dn} = w$ the active thickness of the diode. This characteristic voltage is called full depletion voltage. For all measurements discussed here U_{bias} was above U_{dep}, so the diode was fully depleted. The capacitance of the diode at full depletion is

$$C(U_{bias} \geq U_{dep}) = \epsilon\epsilon_0 \cdot \frac{A}{w} \tag{2.4}$$

with the area of the diode A. Using eqn. 2.2 and eqn. 2.3 the electric field becomes

$$E(x) = \frac{1}{w}\left(U_{bias} + U_{dep}(1 - \frac{2x}{w})\right) \tag{2.5}$$

for $U_{bias} \geq U_{dep}$.

2.2. Charge transport

2.2.1. Generation of free charge carriers

Free charge carriers are constantly generated thermally with the generation rate depending strongly on the impurity and defect concentration of the silicon material and the temperature. In a commercial silicon crystal a certain impurity and defect concentration is always present. Certain impurities and defects generate energy levels in the middle of the band gap. From these energy levels free charge

carriers (electron-hole pairs) can be thermally excited to the conduction or valence band, for electrons and holes respectively. Free charge carriers that are thermally generated inside the depleted region result in the leakage current.

On the other hand, incident radiation can excite electron-hole pairs directly. The mean energy needed to create an electron-hole pair in silicon is 3.6 eV. This energy is higher than E_g because additional phonon excitation is needed for the generation of an electron-hole pair. In this thesis laser light is used for the generation of electron-hole pairs. The energy of the photons used $\hbar\omega \approx E_g$ is similar to the band gap energy. Therefore, additional thermal phonons are needed to excite electron-hole pairs and the attenuation coefficient depends on the temperature.

2.2.2. Drift and diffusion

Free charge carriers are constantly moving with the thermal velocity v_{th} and scattered at phonons as well as ionized impurities. The resulting Brownian movement can be described using the Einstein relation [13] $D_{e,h} = \mu_{e,h} \cdot \frac{k_B T}{e_0}$ with the charge carrier mobility $\mu_{e,h}$. Following [7], the time evolution of the distribution of N_0 charge carriers initially at $t = 0$ and $x = x_0$ in absence of an electric field is

$$N(x,t) = \frac{N_0}{\sqrt{4\pi D \cdot t}} \cdot \exp\left(-\frac{(x-x_0)^2}{4D \cdot t}\right) \tag{2.6}$$

in one spatial dimension. If an electric field is applied, the charge carriers are accelerated and the drift velocity is

$$v_d^{e,h}(E) = \mu_{e,h} \cdot E \tag{2.7}$$

and the instantaneously induced current by a drifting charge inside the depleted region of the diode is

$$I = e_0 \cdot \frac{v_d^{e,h}}{w} \tag{2.8}$$

according to the Ramo theorem [24] for an infinite plate capacitor.

The drift velocity was investigated in this thesis by measuring the induced current of drifting electrons and holes. A parametrization of the carrier mobility $\mu_{e,h} = \mu_{e,h}(E,T)$ is presented in section 5.1.2.2. The underlying drift model is discussed in section 5.1.2.1.

3. Experimental techniques

3.1. Test structures

For this thesis two silicon pad diodes from different manufacturers were investigated. Only one diode was used for the systematic measurements. The other diode was used as cross check.

The test structures are p^+-on-n silicon diodes with an n^+ rear contact. Figure 3.1 shows an exemplary cross section for the type of diode we investigated. The front contact (pad) and the rear contact are made of aluminum. Vias are connecting the aluminum contacts to the front and rear implants through a thin SiO_2 isolation layer. For illumination with laser light there is a window in the pad contact and the rear contact is an aluminum grid. A guard ring is present but was not connected for the measurements performed here. The silicon crystals of $<100>$ orientation for the diodes were grown with the float-zone process in order to achieve a very low impurity concentration. The effective doping of the n bulk is about $N_{eff} = 10^{12}\,\text{cm}^{-3}$.

The standard diode used for most of the measurements was manufactured by Hamamatsu [2] (HPK). The material was thinned by polishing and the target value of the active thickness was $w = 200\,\mu\text{m}$. Capacitance measurements of similar structures from the same wafer placed the active thickness at $203.7 \pm 3.0\,\mu\text{m}$. The physical thickness was measured directly to $204\,\mu\text{m}$ and by dielectric measurement

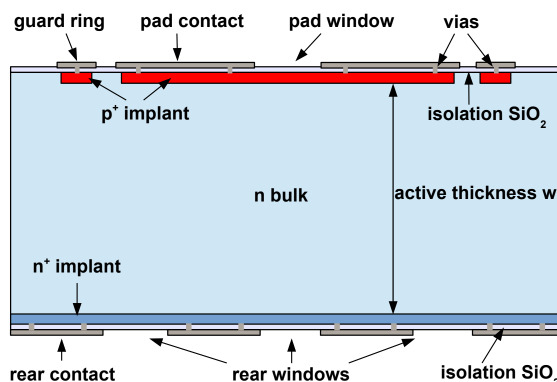

Figure 3.1.: Schematic cross section of a silicon diode (not to scale).

Manufacturer	HPK	CiS
w [µm]	200	287
U_{dep} [V]	87.5	48.2
N_{eff} [cm^{-3}]	$2.9 \cdot 10^{12}$	$0.8 \cdot 10^{12}$
A [mm^2]	4.4	25
$C(U_{bias} \approx U_{dep})$ [pF]	2.7	9.3

Table 3.1.: Physical properties of the test structures we investigated. A refers to the pad area.

to 205 µm. Using measurements of similar structures from the same batch the thickness of the inactive front and rear implants was estimated to be 2.2 µm each (see [31]). With a physical thickness (including the inactive implants) of 204.5 µm the active thickness was assumed to be $w = 200$ µm.

The other diode used for cross check was manufactured by CiS [1] and the target value of the active thickness was 280 ± 15 µm. Capacitance measurements placed the active thickness at 284 µm. The physical thickness was measured directly to 292 µm and by dielectric measurement to 291 µm. Using the same estimation as for the 200 µm HPK diode the active thickness was assumed to be $w = 287$ µm. However, for the CiS diode there are no measurements concerning the implant thickness. Detailed properties for both diodes are given in Table 3.1.

3.2. The Transient Current Technique

The drift of charge carriers was measured by employing the Transient Current Technique (TCT). Free charge carriers are generated almost instantaneously inside the sensor (the diode) by short pulses of laser light. The free charge carriers drift in an applied electric field and induce a current

$$I(t) \propto e_0 \cdot v_d(E) \tag{3.1}$$

with their drift velocity $v_d(E)$. The transient current $I(t)$ is recorded with a fast oscilloscope. A Peltier element is used to control the temperature of the sensor.

For a measurement the sensor is placed on a gold plated chuck with a hole for rear illumination. The chuck is contacting the rear side of the sensor. For the front side pad contact a needle is used. The position of the laser spot on the sensor can be adjusted. After the laser was adjusted the setup is closed and flooded with dry air (for $T < 300$ K). The measurement is started as soon as the measurement temperature is reached and remains stable within ± 0.2 K. The bias voltage U_{bias} is supplied to the pad of the sensor while the rear contact is on ground potential. U_{bias} is ramped in steps of 10 V to a maximum voltage of 1000 V. For each recorded

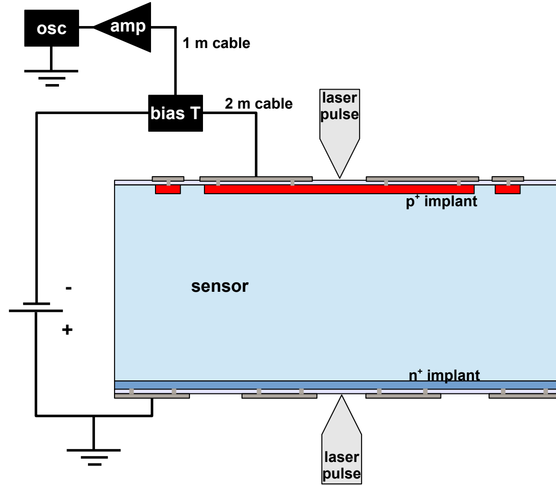

Figure 3.2.: Simplified illustration of the TCT setup. The sensor is illuminated through the front or rear windows. The signal is transmitted from the pad of the sensor via 3 m cables, amplified, and finally recorded by an oscilloscope. The bias voltage is supplied to the pad of the sensor.

transient current pulse 512 measurements are averaged in order to decrease the noise.

The signal is transmitted via 50 Ω cables with a total length of 3 m and a bias tee and then amplified. The signal is recorded by a Tektronix DPO 4104 oscilloscope [30] with a bandwidth of 1 GHz and a sampling rate of 5 GHz. The rise time is 500 ps for the 200 µm sensor and with 800 ps longer for the 287 µm sensor due to its higher capacitance. A schematic illustration of the setup is shown in Figure 3.2.

3.2.1. Laser properties

Two different wavelength lasers are used: a red laser with $\lambda = 675\,\text{nm}$ and a spectral width of $FWHM_\lambda = 3\,\text{nm}$, and an infrared laser with $\lambda = 1063\,\text{nm}$ and $FWHM_\lambda = 7\,\text{nm}$[1]. Basic features of the setup are fast laser pulses to allow the assumption the charge is generated instantaneously; and low light intensity, hence low charge carrier density. High charge carrier densities distort the electric field inside the sensor because of space charge effects (plasma effects, see [33]).

The $FWHM$ of the laser pulse is 44 ps for the infrared laser and 31 ps for the red laser. The profiles of the laser pulses are shown in appendix A.1. A pulse frequency of 200 Hz is used. The laser tune is 50 % and an optical filter of 5 dB (at $\lambda \approx 1400\,\text{nm}$) is used to further decrease the laser intensity. Additionally, the laser light is exiting the glass fiber without focusing, and the diameter of the laser spot is 300 µm at the surface of the sensor. For this setup both lasers create about

[1] With the full width at half maximum $FWHM$. Data according to the owner's manual [6].

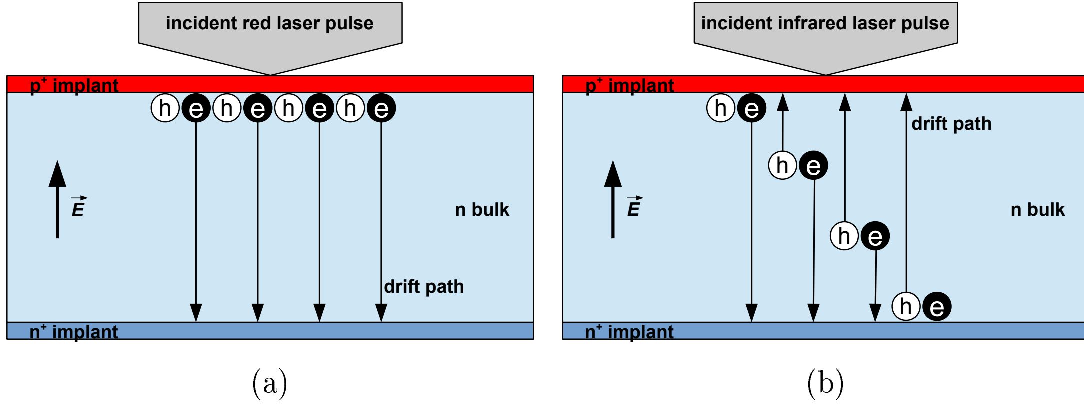

(a) (b)

Figure 3.3.: Schematic of the initial distribution of electron-hole pairs and subsequent charge carrier drift in an electric field $\vec{E}$. Shown here is front illumination with the red (a) and the infrared (b) laser.

$N_{eh} = 10^6$ electron-hole pairs per pulse.

3.2.2. Transient current pulses

The attenuation length of red laser light is $\Lambda_{670\,\mathrm{nm}}(T = 300\,\mathrm{K}) \approx 3.3\,\mu\mathrm{m}$ in silicon. Therefore, electron-hole pairs are created close to the surface of the sensor. For pulsed illumination of the junction (front p^+ implant) of an n-type sensor the generated holes are collected within $\sim 0.2\,\mathrm{ns}$ at the p^+ contact, drifting just a few micrometer. In contrast, the generated electrons drift through the whole sensor to the rear n^+ contact as shown in Figure 3.3(a). The resulting transient current pulse is generated almost solely by the drift of electrons (see Figure 3.4). Likewise, for illumination of the rear n^+ contact the generated electrons are collected very fast at the n^+ contact. The transient is now generated mainly by the drift of holes through the sensor to the junction.

It should be noted that charge carriers are generated not only in the depleted bulk of the sensor, but in the front and rear implant as well. By diffusion these charge carriers can enter the depleted region and contribute to the signal, but the lifetime of these carriers is limited.

Transients generated by an infrared laser pulse are different since the attenuation length in silicon of $\Lambda_{1060\,\mathrm{nm}}(T = 300\,\mathrm{K}) \approx 1500\,\mu\mathrm{m}$ is well above the sensor thickness. Therefore, the infra red light penetrates the whole sensor and reflection at the rear of the sensor occurs. Electron-hole pairs are generated in the whole sensor volume along the path of the light (Figure 3.3(b)). The generated signal is a superposition of electron and hole drift[2].

[2] A transient simulation for the infrared laser is shown in Figure 4.4.

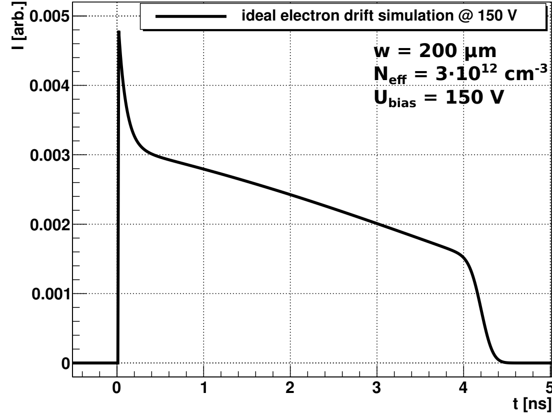

Figure 3.4.: Simulation of a transient current pulse for the situation depicted in Figure 3.3(a). The holes are collected within 0.2 ns while the electrons drift through the whole sensor to the rear contact. The signal is decreasing since the electric field is linear with the maximum value at the front side.

3.2.3. Temperature control

The temperature is controlled with a Peltier element and measured inside the chuck. There is a certain temperature gradient within the sensor. A vertical gradient is present because the surrounding air initially is at room temperature. Additionally, the setup is flooded with room temperature dry air for measurements at low temperatures. The volumetric flow rate is up to $3\,{}^{l}/_{\mathrm{min}}$. Heating of the sensor by means of the flow rate of the dry air was evaluated by measuring the leakage current of an irradiated diode which is a strong function of the temperature. Measurements were performed at low chuck temperatures and at different flow rates. Heating of the sensor was minimized to $\Delta T_{max} = 0.5\,\mathrm{K}$ at $T = 253\,\mathrm{K}$ by using low flow rates and diffusing the dry air in the setup.

Additionally, a horizontal gradient is present because of the hole in the chuck for rear illumination. The hole is centered below the pad of the sensor. Therefore, this region of the sensor has no direct thermal contact to the chuck. Leakage current generates heat in this region. However, the low leakage current of the sensors of several 10 pA at $T = 273\,\mathrm{K}$ and $U_{bias} = 1000\,\mathrm{V}$ corresponds to a heating power of just several 10 nW. Because of the low leakage current and the high thermal conductivity of silicon the horizontal gradient is supposedly very low.

4. Analysis

4.1. The time-of-flight method

In this section the determination of the charge carrier drift velocity from the TCT measurements using the time-of-flight (tof) method is presented[1]. It is a rather simple method to obtain the time of flight t_{tof} which in this case describes the duration of a TCT current pulse initiated by the red laser. Since the red laser is used only one type of charge carriers drifts through the whole sensor and t_{tof} is obtained separately for electrons and holes. Assuming operation above full depletion ($U_{bias} > U_{dep}$) and the electric field constant inside the sensor the drift velocity is

$$v_d^{e,h}(E) \quad = \quad \frac{w}{t_{tof}^{e,h}} \tag{4.1}$$

with the active sensor thickness w.

In the bulk of a silicon sensor with a uniform effective doping concentration $N_{eff}(x) = const$ the electric field is not constant but linear. The mean electric field inside the sensor is $\overline{E}(U_{bias}) = \frac{U_{bias}}{w}$ with the applied bias voltage U_{bias}. The minimum and maximum values of the electric field are $E(U_{bias})_{max,min} = \frac{U_{bias} \pm U_{dep}}{w}$. For a linear electric field $t_{tof} = \int_0^w \frac{dx}{v_d(E(x))}$ is only a measure of the apparent velocity

$$v_{app}(\overline{E}(U_{bias})) \quad = \quad \frac{w}{t_{tof}} \tag{4.2}$$

which differs from $v_d\big(\overline{E}(U_{bias})\big)$ particularly for low electric field values, where the gradient $\frac{dv_d}{dE}$ is large. Therefore, the validity of this method is limited to high U_{bias}.

The signal is distorted by several effects, so t_{tof} is obtained - different to the method used in the literature - as the time difference between the points of maximum slope ($\frac{d^2I}{dt^2} = 0$) at the rising and falling edge of the current pulse as shown in Figure 4.1. The sampling interval of the oscilloscope of $\delta t = 200\,\mathrm{ps}$ is too large to allow an accurate measurement of t_{tof} for short current pulses of a few nanosec-

[1] For a detailed description and discussion of the tof method see [10].

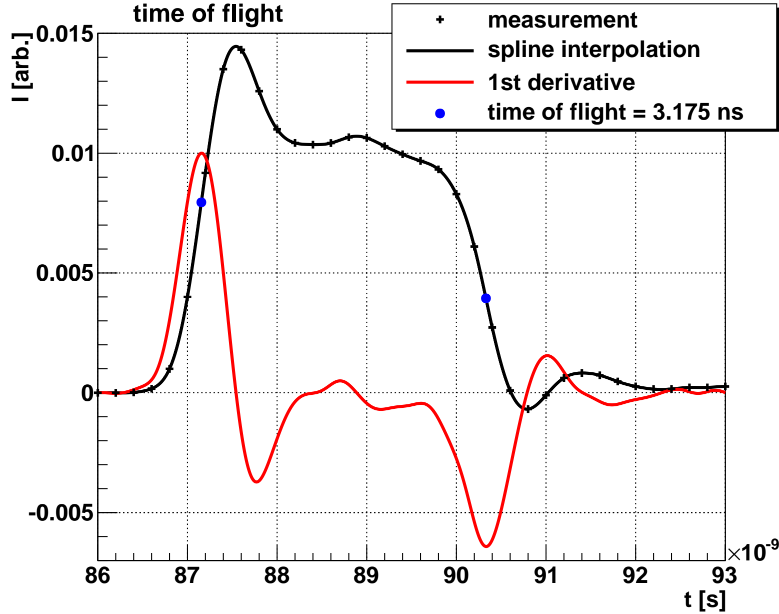

Figure 4.1.: Determination of t_{tof} at the maximum values of $|\frac{dI}{dt}|$ for the rising and falling edges of the signal (blue dots) for electron drift in the 200 µm sensor at $U_{bias} = 200\,\text{V}$ and $T = 313\,\text{K}$.

onds directly. Therefore, a spline interpolation of the signal is used to calculate the points of maximum slope.

In the literature [10, 9, 17, 22] the full width at half maximum $FWHM$ was used to determine t_{tof}. This can not be applied for the sensors investigated here because $E_{max} - E_{min}$ is large in comparison to the sensors discussed in the literature. Additionally, the capacitance of our sensors is up to nine times above the capacitance of the sensors discussed in the literature, and the recorded current pulses are very short at high bias voltages ($t_{tof} \approx 2\,\text{ns}$). However, our approach is even more accurate than the $FWHM$ method for very long and uniform pulses comparing ${}^{v_{app}(\overline{E})}/_{v_d(\overline{E})}$ extracted from simulations for the $w = 287\,\mu\text{m}$ thickness high resistivity sensor with a more uniform electric field. Assuming a constant electric field both methods have shown equally accurate results in the simulations for the 287 µm sensor while the maximum slope method has shown a better accuracy for the 200 µm sensor (for shorter pulses).

Distortion of the signal occurs due to the time spectrum of the laser pulse which is to first approximation a Gaussian function with $FWHM = 44(31)\,\text{ps}$ for the red (infrared) laser. At the points of maximum slope there is no broadening of the current pulse by the laser pulse. The distortion is the integral of the Gaussian function, the error function $\text{erf}(x)$, with the maximum slope at the maximum value of the Gaussian (the center of the laser pulse). However, the current pulse

is slightly prolonged at the points of maximum slope since the rise time of the laser pulse is slightly shorter than the fall time (see appendix A.1). The diffusion length is small in comparison to the thickness of the sensors and it is assumed to be equal in and against the drift direction. Therefore, the center of gravity of the drifting charge cloud, hence the current pulse length at the points of maximum slope, is not affected by diffusion. The main problem are the effects of the sensor capacitance and the read-out circuit which lead to a more complicated asymmetric distortion[2].

In order to determine the error of t_{tof} related to the effects discussed here simulations were performed for high electric fields of $\overline{E} \geq 15\,\mathrm{kV/cm}$ where the gradient $\frac{dv_d}{dE}$ is sufficiently small. Accordingly, the error for $\overline{E} \geq 15\,\mathrm{kV/cm}$ was estimated to be 1 % for the sensors investigated in this thesis.

4.2. Transient current pulse simulation

For the analysis of the TCT measurements a one-dimensional simulation of charge transport in silicon is used. The original simulation code was written by Julian Becker in 2010 and modified for this thesis. A more detailed description of the simulation can be found in Becker's PhD thesis [7]. This section follows chapter 7 of Becker's thesis.

For the simulation a one dimensional spatial grid with a cell size of $\Delta x = 100\,\mathrm{nm}$ and a step size of $\Delta t = 10\,\mathrm{ps}$ in the time domain is used. It is always checked whether the charge carriers move at least into the next grid cell within one time step[3] $v_d \cdot \Delta t > \Delta x/2$, meaning whether there is current, and whether charge is conserved. In the simulation first an initial charge distribution at $t = 0$ is calculated, and then the subsequent drift and diffusion of the charge carriers in an electric field are computed. The drifting charge carriers induce a signal proportional to their drift velocity until they are stopped and removed at the read-out contacts. Figure 4.2 shows one time step of the simulation. When all charge carriers are collected the induced current pulse is convolved with the response function of the read-out circuit. The convolved current pulses are compared to the measured TCT spectra and certain parameters of the simulation are fitted in order to obtain the optimum description of the measurements.

[2]See section 4.2.4.
[3]This is not true for a few simulations discussed here. See section 5.3.1.

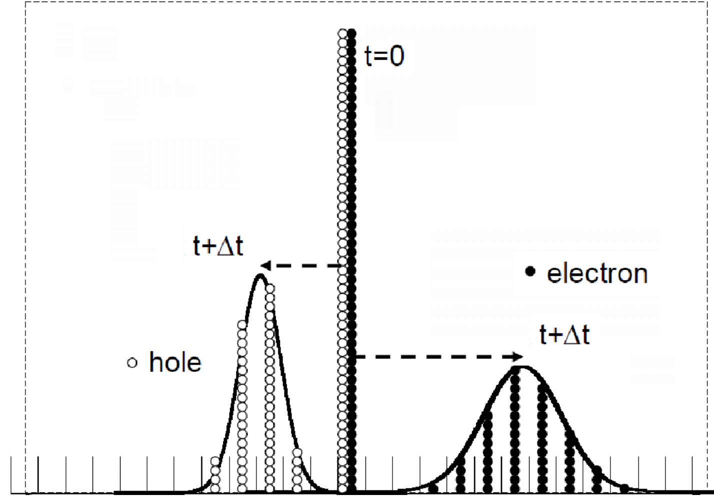

Figure 4.2.: One time step of the simulation. At $t = 0$ the same amount of electrons and holes is in one single cell. After one time step Δt the electrons and holes have drifted in opposite directions in the electric field. The charge distribution is widened by the diffusion of the charge carriers. Taken from [7].

λ [nm]	a_1 [cm^{-1}]	a_2 [cm^{-1}K^{-1}]	$\alpha_s^{-1}(T = 300\,\text{K})$ [µm]
670	720	7.6	3.3
1060	-59.4	0.24	794

Table 4.1.: Temperature coefficients a_1 and a_2 taken from [19] with the original data from [20, 12] for the attenuation coefficient $\alpha_s(T) = a_1 + b_2 \cdot T$ at different photon wavelengths λ.

4.2.1. Initial charge distribution

The charge generation by a laser pulse is assumed to be instantaneous. Accordingly, the initial spatial distribution of charge carriers is simulated as

$$N_{e,h}(x, t = 0) \quad = \quad \alpha_s N_{tot} \cdot e^{-\alpha_s x} \tag{4.3}$$

with the attenuation coefficient α_s and the total number of electron-hole pairs generated N_{tot}, which is proportional to the intensity of the laser light. Electrons and holes are generated in pairs; therefore, they are generated in equal numbers. The temperature dependence of α_s is modeled as $\alpha_s(T) = a_1 + a_2 \cdot T$ with values of a_1 and a_2 given in Table 4.1. The model parameters for wavelengths of 670 nm and 1060 nm are used instead of the exact laser wavelength (675 nm and 1063 nm) since these parameters are poorly known. For the infrared laser little impact on the simulated pulse shapes is seen when varying these parameters. For the red laser differences are noticeable but not with respect to the current pulse length.

For the infrared laser reflection at the rear of the sensor changes the initial

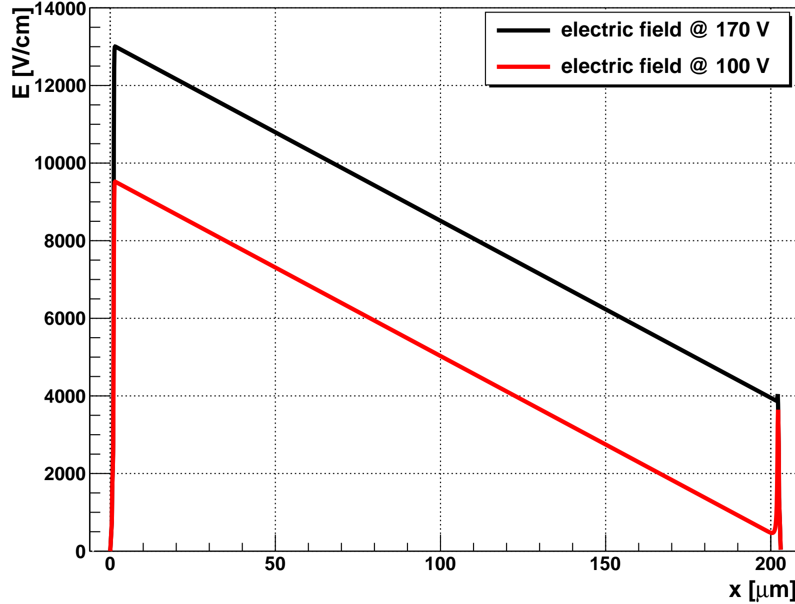

Figure 4.3.: Electric field from a TCAD simulation for a diode with a total thickness of 203 μm including 1.5 μm each for the junction and the rear implant at different U_{bias}. The bulk doping is $N_{eff} = 3 \cdot 10^{12}\,\text{cm}^{-3}$ and the junction and rear implant doping is $N_{eff} = 3 \cdot 10^{19}\,\text{cm}^{-3}$. Note the peak in the electric field at the rear implant ($x \approx 203\,\mu\text{m}$). Simulation by J. Schwandt.

charge distribution for higher temperatures where $\alpha_s^{-1} \approx w$ and the initial charge distribution is no longer exponential according to equation 4.3. Reflection is not taken into account because even at $T = 333\,\text{K}$ the effect on the simulated current pulse shape is small. Additionally, the exact reflection coefficient at the rear of the sensor is not known and depends on the position of the laser spot on the sensor.

4.2.2. The electric field

With the assumption $N_{eff}(x) = const$ throughout the sensor the electric field in the sensor takes a linear form (equation 2.5) with the maximum field at the p-n junction at $x = 0$ for the fully depleted sensor ($U_{bias} > U_{dep}$). The assumption $N_{eff}(x) = const$ is generally not correct for the junction and the rear implant where N_{eff} changes rapidly within about 2 μm from $10^{12}\,\text{cm}^{-3}$ to $10^{19}\,\text{cm}^{-3}$. For low bias voltages a spike in the electric field at the rear implant is expected. A TCAD [28] simulation of the electric field including the junction and the rear contact is shown in Figure 4.3. The simulated field profile was implemented but no considerable change was noticed. Hence the linear field model (eqn. 2.5) is used in the simulation for the sake of simplicity.

The p-n junction and the rear implant are treated as electrodes that do not

contribute to the active sensor thickness w. The so-called built-in potential of the p-n junction as well as the potential of the rear n$^-$-n$^+$ junction are neglected, but would add to the bias voltage.

4.2.3. Signal formation

Quoting [7] „the induced current is calculated according to the Ramo theorem [24]. The induced current (normalized to the elementary charge e_0) can be approximated by"

$$I(t+\Delta t) = \sum_i \left[I_e(x_i, t+\Delta t) - I_h(x_i, t+\Delta t)\right] \tag{4.4}$$

$$I_{e,h}(x_i, t+\Delta t) = \Phi_w(x_i) \cdot \frac{e_0}{\Delta t} \cdot \left[N_{e,h}(x_i, t+\Delta t) - N_{e,h}(x_i, t)\right] \tag{4.5}$$

with the weighting potential of parallel plate capacitor[4] $\Phi_w(x_i) = 1 - {}^{x_i}/_{w}$ and the number of electrons or holes $N_{e,h}(x_i, t)$ at the time t. The number of charge carriers after one time step Δt is

$$N_{e,h}(x_i, t+\Delta t) = \sum_j N_{e,h}(x_j^*, t) \cdot A(x_i, x_j^*) \tag{4.6}$$

with the position x_j^* at t and the movement of carriers $A(x_i, x_j^*)$ within one time step Δt due to charge drift in the electric field and diffusion. The mean charge drift in the electric field is

$$\delta x(x_i) = \pm\overline{\mu_{e,h}}(x_i)\overline{E}(x_i)\Delta t \tag{4.7}$$

with the charge carrier mobility $\mu_{e,h}(x_i)$ and the sign taking into account the opposite directions of electron and hole drift. Different mobility models $\mu_{e,h}(E,T)$ are implemented in the simulation. The average values of $\mu_{e,h}$ and E are calculated for the traveled distance (number of grid cells) if more than one grid cell is traversed within one time step.

Drift and diffusion are calculated for each grid cell as

$$A(x_i, x_j^*) = \frac{1}{2} \cdot \left[\mathrm{erf}\left(\frac{x_j^* + \delta x(x_i) - x_i + {}^{\Delta x}/_2}{\sqrt{2}\sigma_{e,h}(x_i)}\right) - \mathrm{erf}\left(\frac{x_j^* + \delta x(x_i) - x_i - {}^{\Delta x}/_2}{\sqrt{2}\sigma_{e,h}(x_i)}\right)\right] \tag{4.8}$$

[4] Commonly used for a pad diode in reverse bias.

where the charge distribution is the integral of a Gaussian function shifted by δx with the standard deviation $\sigma_{e,h}(x_i) = \sqrt{2 \cdot D_{e,h}(x_i)\Delta t}$ from the beginning of the cell $x_i - \frac{\Delta x}{2}$ to the end of the cell $x_i + \frac{\Delta x}{2}$. For the diffusion constant the Einstein relation [13] for charged particles $D_{e,h}(x_i) = \frac{\mu(x_i) \cdot k_B T}{e_0}$ is used so the standard deviation becomes

$$\sigma_{e,h}(x_i) = \sqrt{2 \cdot \overline{\mu_{e,h}}(x_i) \cdot \frac{k_B T}{e_0} \cdot \Delta t} \tag{4.9}$$

again with the average value of the mobility.

Effects like the trapping of charge carriers and charge multiplication in very high electric fields are implemented in the simulation program but were not applied for the simulations presented in this thesis.

4.2.4. Read-out circuit convolution

Up to now the transient response of the read-out circuit is neglected in the simulation. The signal is altered by many effects such as parasitic capacities, inductance, reflections, external electromagnetic radiation, and noise. Strong contributions are due to the capacitance of the sensor under test and the limited bandwidth of the oscilloscope, both exhibiting low pass characteristics. Additionally, the charge deposition by the laser is not instantaneous, but the laser pulse exhibits a certain spectrum. All these effects, except for random ones like varying external radiation and noise, are accounted for by the convolution of the simulated current pulse with the response function of the setup.

The response function of the electronics was at first obtained by a SPICE [4] simulation of the read-out circuit, but the quality of the SPICE simulation and the description of the current pulses was poor. Instead of simulating the electronic circuit the convolution theorem [18]

$$\mathcal{F}\{f \star g\} = \mathcal{F}\{f\} \cdot \mathcal{F}\{g\} \tag{4.10}$$

is used to determine the response function of the read-out circuit. Here f is the simulation, g the response function of the circuit, and $f \star g$ is their convolution. $\mathcal{F}\{f\}$ denotes the Fourier transform of f. Since the data is discrete the fast Fourier transform is used for the calculations. Assuming the simulation to be correct the measurement can be described by $(f \star g) + \epsilon$ with an additional noise term ϵ. Accordingly, the simulated current pulse before the read-out circuit convolution

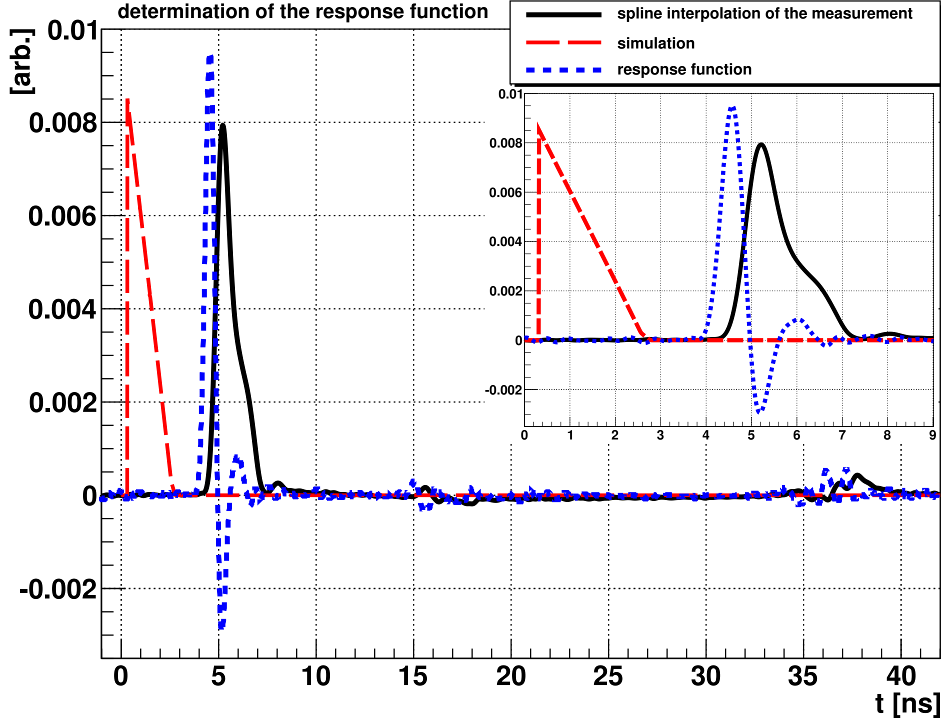

Figure 4.4.: Determination of the response function (blue) using a spline interpolation of the measured current pulse (black) and the simulated current pulse (red) for the 200 µm sensor illuminated through the pad window with the infrared laser at $T = 313\,\mathrm{K}$ and $U_{bias} = 1000\,\mathrm{V}$. The inset shows the situation for $t = 0\,\mathrm{ns}$ to $9\,\mathrm{ns}$.

and the measured current pulse are used to obtain the response function[5]

$$conv = \mathcal{F}^{-1}\left(\frac{\mathcal{F}\{measurement\}}{\mathcal{F}\{simulation\}}\right) \tag{4.11}$$

where the noise term is neglected. Actually, noise limits the accuracy of the calculated response function. But for the part of the response function relevant to the current pulse shape the signal-to-noise ratio is usually high compared to the region after the pulse, where much smaller reflections of the current pulse are located (see Figure 4.4).

In order to get a good estimate of the response function the current pulse used should be fast, so the contribution of the read-out circuit to the pulse shape is large[6]. A spline interpolation of the measured pulse shapes with a sampling interval of 10 ps is used for the determination of *conv* since the sampling interval of the oscilloscope $\delta t = 200\,\mathrm{ps}$ is much larger than the time step size $\Delta t = 10\,\mathrm{ps}$ of the simulation. This leads to a trade-off between short pulses for a high contri-

[5]Or convolution function *conv*.

[6]The convolution of an infinitely fast signal $\delta(x - x')$ is $\delta(x - x') \star conv(x) = conv(x - x')$.

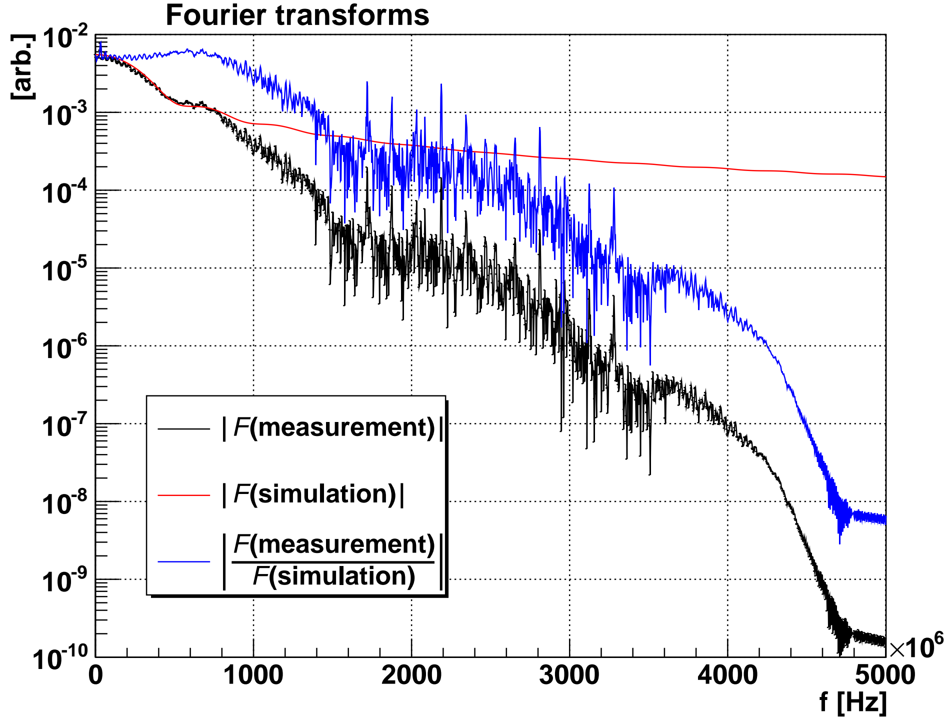

Figure 4.5.: Absolute values of the Fourier transforms of the spline interpolation of the measured current pulse (black), the simulated current pulse (red), and the ratio of them both $|\mathcal{F}\{conv\}|$ corresponding to Figure 4.4.

bution of the electronics and long pulses for many sampling points, hence a good interpolation. For this thesis the best results were achieved for fast pulses at the highest possible bias voltage of $U_{bias} = 1000\,\mathrm{V}$. For the analyses the response functions for both sensors were determined at $T = 313\,\mathrm{K}$ and $U_{bias} = 1000\,\mathrm{V}$ for front illumination with the infrared laser. These response functions were used for all temperatures investigated and for both the red and the infrared laser.

Figure 4.4 shows the simulated current pulse, the spline interpolation of the measured current pulse, and the response function determined from both of them including the region after the signal, where reflections are observed. Figure 4.5 shows the corresponding absolute values of the Fourier transforms of the measurement, the simulation, and $|\mathcal{F}\{conv\}| = \left|\frac{\mathcal{F}\{measurement\}}{\mathcal{F}\{simulation\}}\right|$. For high frequencies $f > 1\,\mathrm{GHz}$ the absolute value of the Fourier transform of the measurement is much smaller than the absolute value of the Fourier transform of the simulation. Consequently, there is minor contribution of high frequencies (noise, spline interpolation) to $|\mathcal{F}\{conv\}|$.

The current pulse generated by the infrared laser was chosen since the theoretical current before convolution (see fig. 4.4) increases very fast and then immediately decreases. Additionally, electron and hole drift contribute equally to the signal and possible differences are averaged. In Figure 4.6 an exemplary simulated current

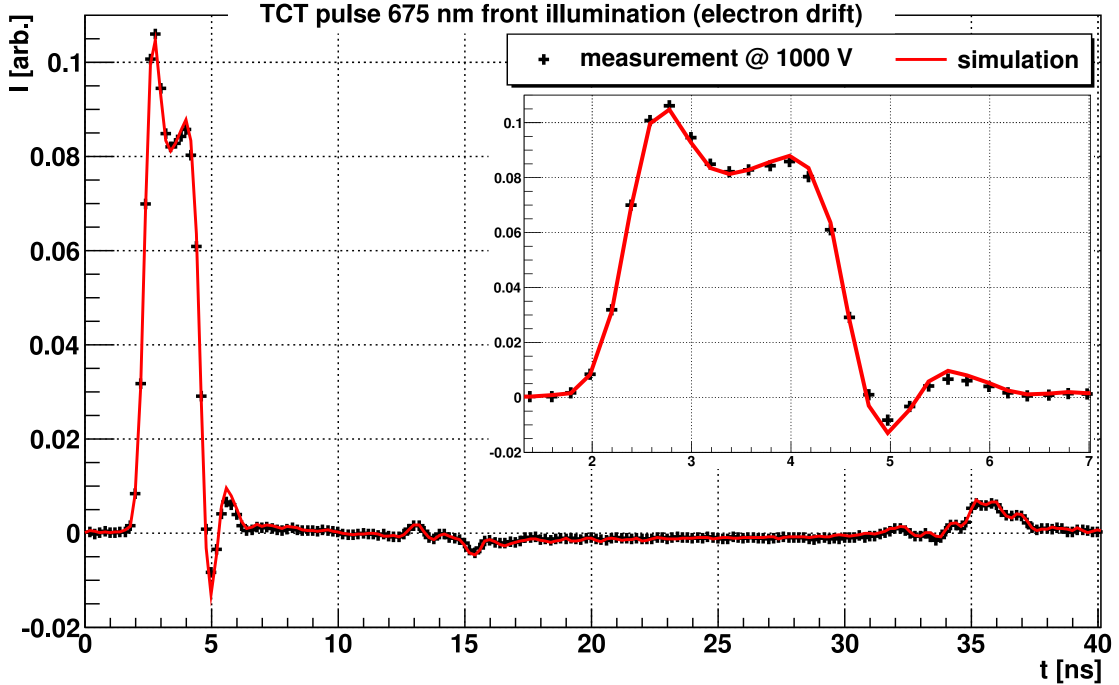

Figure 4.6.: Example for the performance of the convolution method. Shown is the measured TCT spectrum (crosses) for electron drift and the simulation (red line) with the response function obtained from the measurement for the infrared laser. Note the description of the reflection of the current pulse on the right. The inset shows a closeup of the pulse.

pulse convolved with the response function (obtained as described) is compared to the measured one for front illumination with the red laser.

4.2.5. Fitting

Certain parameters of the simulation, namely parameters of the charge carrier mobility, were fitted to find the best description of the measured data. For this purpose

$$\chi^2(\alpha) = \sum_{i=1}^{n} \left(\frac{f(x_i, \alpha) - m_i}{\sigma_i} \right)^2 \tag{4.12}$$

was minimized using the Migrad algorithm of the ROOT [3] package Minuit. Here α denotes the vector of free fit parameters and σ_i the measurement errors. The sum over the number of individual measurements n of the squared difference between the simulation $f(x_i, \alpha)$ and the measurement m_i reaches its minimum for the best fitting parameters α.

According to the number of individual measurement points the error σ_i was

chosen around 0.1, so $\chi^2(\alpha)$ was always in the order of 10 while the number of degrees of freedom was $n \approx 1.6 \cdot 10^5$. Therefore, the Minuit error of the best fit parameters was relative. The fit was performed taking 50 ns of the measurement into account. The current pulse starts at $t = 2$ ns and the simulated one was synchronized accordingly. All points with $f(x_i, \alpha) \neq 0$, including the reflection, were used for the calculation of $\chi^2(\alpha)$. For a realistic error estimation $\chi^2(\alpha) \approx n$ was very large and the fit algorithm did not converge (see below).

For the calculation of $\chi^2(\alpha)$ the sampling interval of the individual measurement points of $\delta t = 200$ ps was used. Since the simulation time step size, in other words the time bin size, $\Delta t = 10$ ps is much shorter than δt, the simulation was synchronized with the measurement in steps of Δt without further interpolation. However, this causes discontinuities of $\chi^2(\alpha)$ when the synchronization is suddenly shifted by Δt following variations of the free parameters α. These discontinuities are probably the reason the fit algorithm did not converge for realistic errors.

For the synchronized simulation $f(x_i, \alpha)$ the very value of the simulation for the individual time bin t_i at the center of the measurement sampling interval δt was used. The average value of the simulation time bins within $\pm\frac{\delta t}{2}$ was not used because the sample acquisition time of the oscilloscope is assumed to be much shorter than the sampling interval of $\delta t = 200$ ps[7]. Consequently, the measured current at a certain time $I(t_i)$ is assumed to be the true current at that very time rather than the sum $\overline{I}(t_i) = \frac{\Delta t}{\delta t} \cdot \sum_{i=(t_i - \delta t/2)/\Delta t}^{(t_i + \delta t/2)/\Delta t} I(t_i)$.

Two different kinds of fits were performed for the analyses. Global fits were performed, where all measurements for different bias voltages and front and rear illumination with the red laser as well as illumination with the infrared laser were fitted at once for all temperatures investigated. This means about $1.6 \cdot 10^5$ individual measurement points were evaluated for one fit. Additionally, range fits were performed meaning only a small voltage/temperature range or even single voltages/temperatures were fitted for only one or more types of laser illumination. The range fits were performed in order to investigate the charge carrier mobility for a small electric field/temperature range, with less dependency on the parametrization, for cross check of the global fit results.

[7] The documentation [30] does not mention the acquisition time.

5. Results

5.1. Mobility parametrization

5.1.1. Parametrization in the literature

TCT measurements on non-irradiated silicon sensors in <100> crystal orientation were performed. The observed current pulse length was not well described in the simulation using the parametrization of the drift velocity by Caughey and Thomas [11]:

$$v_d^{e,h} = \frac{\mu_0^{e,h} \cdot E}{(1 + (\frac{v_s^{e,h} \cdot E}{\mu_0^{e,h}})^{\beta_{e,h}})^{1/\beta_{e,h}}} \tag{5.1}$$

where μ_0 denominates the low field mobility, v_s the saturation velocity, and β is a fit parameter close to 1. Parameter values for the <111> crystal orientation published by Jacoboni et al. [17] were used - despite the anisotropy of carrier drift in silicon with respect to the crystallographic direction [10] - because there are few publications on carrier drift in the <100> direction.

Figure 5.1 shows measurements of the $w = 200\,\mu\text{m}$ and the corresponding simulations with the Jacoboni parameters for $U_{bias} = 1000\,\text{V}$ at $T = 313\,\text{K}$. While the simulated electron drift is faster, the simulated hole drift is slower than the corresponding measurement. This applies to the whole electric field range of $\overline{E} = (5 - 50)\,\text{kV/cm}$ investigated for the 200 µm sensor and, due to the different sign of the deviations for electrons and holes, can not be attributed to a wrong estimation of the sensor thickness w. Fitting the Caughey-Thomas parametrization to the measurements resulted in non-scientific values for μ_0^h and v_s^h, hence the parametrization does not yield a reasonable description of our measurements.

Looking at the literature there is a wide spread in the reported low field mobilities [14] and saturation velocities [8, 10, 26] for electrons and holes in <111> crystal direction. Just recently, parameter values for the Caughey-Thomas parametrization in <100> direction were published by Becker [8], obtained with the same simulation used here. These values describe the electron drift measurements well, but

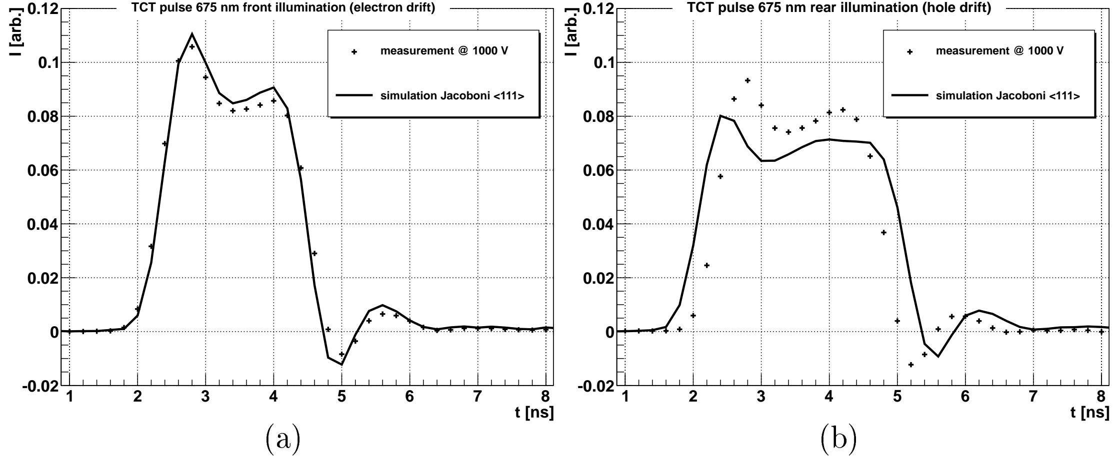

Figure 5.1.: TCT measurements (crosses) of the 200 µm sensor at $T = 313\,\mathrm{K}$ and $\overline{E} = 50\,\mathrm{kV/cm}$ in <100> crystal orientation for electron drift (a) and hole drift (b). The measurements are compared to the simulations (solid lines) using the Jacoboni [17] parameters for <111> crystal orientation.

still do not describe the hole drift for high electric field values of several $10\,\mathrm{kV/cm}$, that were not investigated by Becker. It should be noted that a slightly different parametrization was derived by Hänsch [16] and quantified extensively for <111> crystal orientation [26, 23], but yields no improvement over the Caughey-Thomas parametrization.

5.1.2. An approach to find a better description

The time of flight measurements by Canali [10] were analyzed in order to explain the differences between our measurements and the literature data. Figure 5.2 shows the experimental values and the parametrization (eqn. 5.1) for <111> orientation. Especially for holes at low temperatures and high fields there are differences between the measurements and the parametrization. This discrepancy lead us to a slightly different parametrization of the drift velocity. Here the underlying simple transport model based on Grove [15] is presented and the modified parametrization is introduced.

5.1.2.1. The transport model

Without an external electric field the free charge carriers experience random Brownian motion characterized by the thermal velocity $v_{th} = \sqrt{\frac{2k_BT}{m^*_{e,h}}}$ with the Boltzmann constant k_B and the effective mass of the charge carriers $m^*_{e,h}$. If an external electric field is present, a charge carrier is accelerated until a collision takes place. In our case of high purity silicon the collision rate $1/\tau_{coll}$ with the mean time between collisions τ_{coll} is dominated by lattice scattering [15] and independent of N_{eff}. In

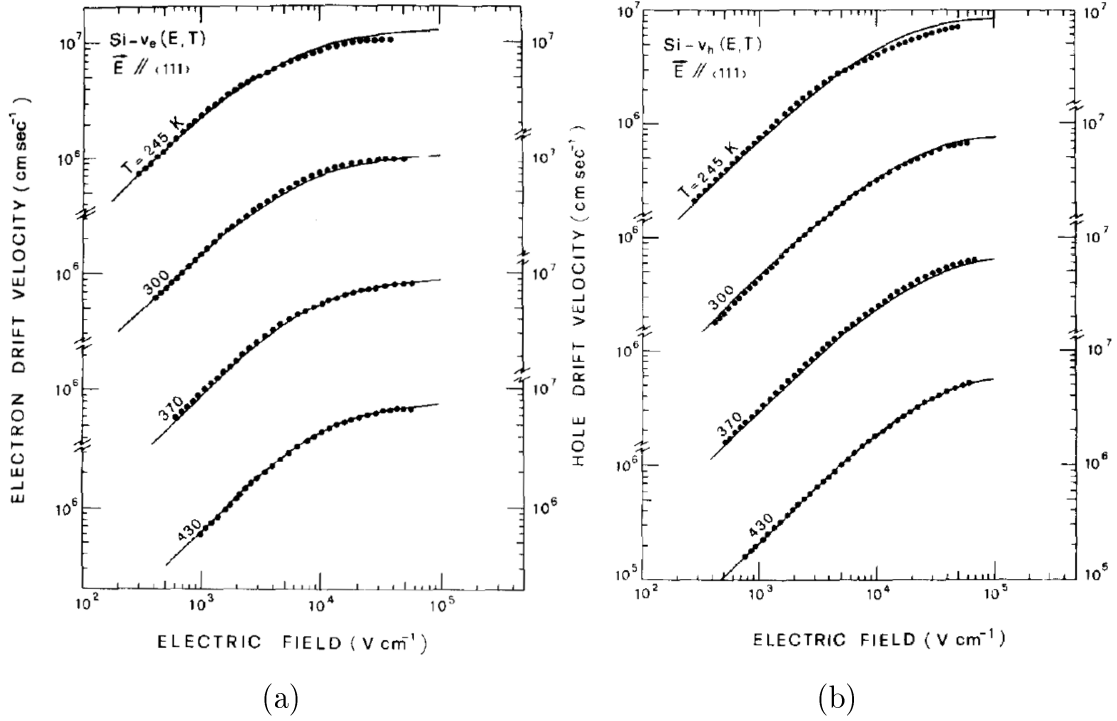

Figure 5.2.: Experimental values (points) and the parametrization (solid lines) for <111> crystal orientation for electrons (a) and for holes (b). Taken from [17] with data from [10, 9].

this model the velocity of the charge carriers is assumed to be $v(t = \tau_{coll}) = 0$ immediately after a collision, and the carrier is accelerated again until the next collision takes place. The mean drift velocity becomes

$$v_d(E) \quad = \tfrac{1}{2}a \cdot t = \quad \frac{qE}{2m^*} \cdot \tau_{coll} = \mu_0 \cdot E \tag{5.2}$$

with the low field mobility μ_0. In the case of very low electric fields the drift velocity is much smaller than the thermal velocity[1] and the collision rate is constant $^1/_{\mu_0} \propto {}^1/_{\tau_{coll}(v_{th})}$.

For an electric field above a certain value E_0 the charge carriers gain enough energy for the emission of optical phonons [17]. With increasing carrier energy the probability of an emission increases. Therefore, the mobility becomes a function of the electric field

$$^1/_{\mu(E \geq E_0)} \quad \propto \quad {}^1/_{\tau_{coll}} + {}^1/_{\tau_e(E)} \tag{5.3}$$

with the phonon emission rate $^1/_{\tau_e(E)}$. This leads to the saturation of the electron drift velocity at very high electric fields [17] where the energy loss from phonon emission becomes equal to the energy gain from the electric field. This model

[1] $v_{th}^{e,h}(T = 300\,\mathrm{K}) \approx 10^7\,\mathrm{cm/s}$.

is oversimplified and there are many effects at high fields [17] apart from optical phonon emission that are not taken into account here.

5.1.2.2. The new parametrization

The inverse mobility calculated from the Canali measurements is shown in Figure 5.3. The model prediction of constant mobility for low electric fields is reproduced by the measurements, and the phonon emission rate depends to a good approximation linearly on E. A simple parametrization based on these findings is introduced:

$$^1/_{\mu(E)} \quad = \begin{cases} ^1/_{\mu_0} & E < E_0 \\ ^1/_{\mu_0} + ^1/_{v_{sat}} \cdot (E - E_0) & E \geq E_0 \end{cases} \tag{5.4}$$

where the mobility is constant for low electric fields

$$\mu(E \quad < \quad E_0) = \mu_0 \tag{5.5}$$

and the Trofimenkoff [32] parametrization[2] for higher electric fields

$$\mu(E \quad \geq \quad E_0) = \frac{\mu_0}{1 + \frac{\mu_0}{v_{sat}} \cdot (E - E_0)} \tag{5.6}$$

with an electric field offset E_0.

This parametrization is not continuously differentiable because of the discontinuity at $E = E_0$, but the parametrization

$$^1/_{\mu(E\,[\mathrm{V/m}])} \quad = \quad ^1/_{\mu_0} + \frac{E - E_0}{2v_{sat}} \cdot (1 + \tanh(E - E_0)) \tag{5.7}$$

is, with a negligible deviation[3] to equation 5.4 close to $E = E_0$. Note that E has to be in units of V/m as the hyperbolic tangent depends on the scale. However, the original expression 5.4 with the maximum criterion was used for further analysis.

It should be noted that the constant part of the mobility μ_0 is known as the ohmic region of the drift velocity $v_d(E) = \mu_0 \cdot E$. It was quantified for example by Ottaviani [22] to hold up to $E = 2\,\mathrm{kV/cm}$ for electrons in silicon at $T = 300\,\mathrm{K}$ (see fig. 5.3). So this new parametrization just adds the constant ohmic part of $\mu(E)$

[2] In 1967 Caughey and Thomas added the exponent $\beta_{e,h}$ - that we now drop - to the Trofimenkoff parametrization published in 1965.

[3] The relative deviation is $\sim 10^{-3}\,\%$.

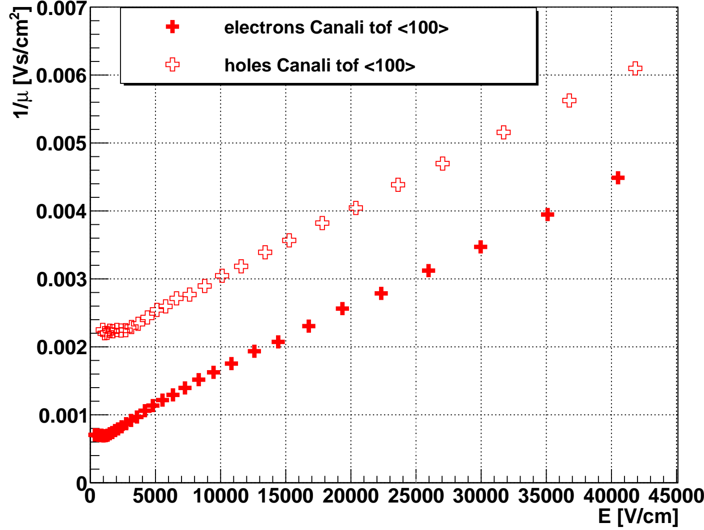

Figure 5.3.: Inverse mobility for electrons (filled) and holes (open) calculated from time of flight measurements performed by Canali et al. [10] at $T = 300\,\mathrm{K}$ for the $<$100$>$ crystal orientation. Shown here are not the actual measurements but the values we extracted from plots of [10].

to the Trofimenkoff parametrization published in 1965. However, the sensitivity of our measurements ($\overline{E}_{min} = 2.4\,\mathrm{kV/cm}$) to the low field mobility is very limited and due to strong correlations of the parameters we were not able to determine the low field mobility. Therefore, the parameter μ_0 of the following analyses is just a fit parameter and must not be mistaken for the low field mobility as it is used in the literature. Nevertheless, the expression μ_0 is used because the parameter μ_0 is expected to become the low field mobility if our measurements were sensitive to lower electric fields.

5.1.3. Comparison with measurements

Here the new parametrization was used for the simulation and was fitted to the TCT measurements performed for this thesis. The best fit parameters obtained for single temperatures are compared to the time of flight results.

5.1.3.1. Modified parametrization for the mobility of holes

Analysis of the simulated and the measured TCT spectra for hole drift indicates that the linear expression (eqn. 5.4) is not sufficient to describe the mobility of holes. Figure 5.4 shows the TCT spectra for the 200 μm sensor at different bias voltages at $T = 233\,\mathrm{K}$. The pulse length of the simulated spectra is too long for low and for high electric fields, but too short in between. In order to describe the

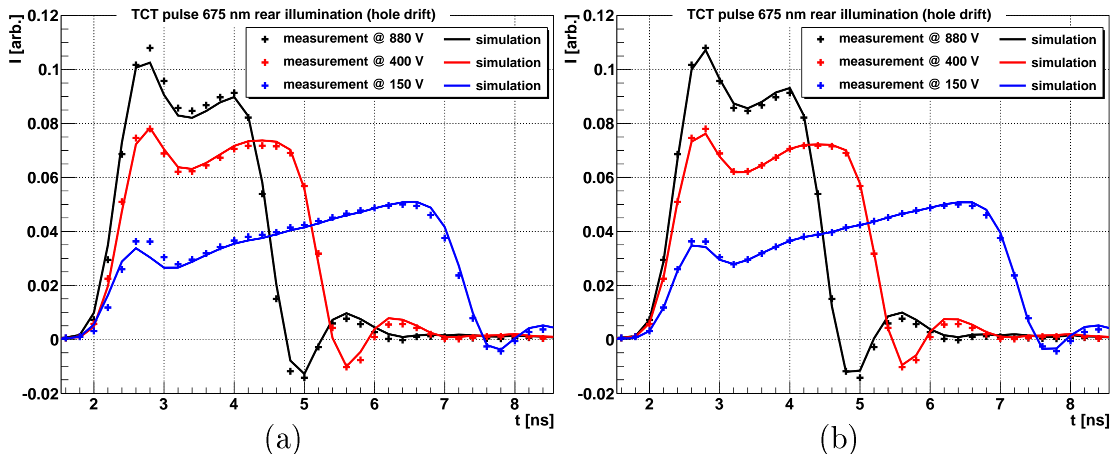

Figure 5.4.: TCT spectra for hole drift at $T = 233\,\mathrm{K}$. (a) shows the simulation (lines) using the linear parametrization (eqn. 5.4). The drift time is too long compared to the measurements (crosses) for $U_{bias} = 150\,\mathrm{V}$ and $U_{bias} = 880\,\mathrm{V}$. Contrary the drift time of the simulation is too short for $U_{bias} = 400\,\mathrm{V}$. (b) shows the simulations using eqn. 5.8.

observed pulse length equation 5.4 was modified and a quadratic term was added:

$$1/\mu_h(E) = \begin{cases} 1/\mu_0^h & E < E_0 \\ 1/\mu_0^h + b \cdot (E - E_0) + c \cdot (E - E_0)^2 & E \geq E_0 \end{cases} \tag{5.8}$$

where the parameters b and c are introduced. Parameter b corresponds to an inverse velocity and for $c = 0$ the parameter becomes $b = 1/v_{sat}$.

This approach is not suitable for very high electric fields because $v_d(E)$ would increase to infinity. However, if $\overline{E} \gtrsim 100\,\mathrm{kV/cm}$, the charge carriers acquire enough energy to generate new electron-hole pairs[4], and the model which was introduced in section 5.1.2.1 has to be extended. Further measurements have to be performed in order to determine the electric field range where it is still reasonable to use equation 5.8. In the present measurements the quadratic approximation holds up to $\overline{E} = 50\,\mathrm{kV/cm}$ and was used for the mobility of holes in all further analyses. Preliminary tests were performed using a different sensor suggesting the model holds up to $\overline{E} = 70\,\mathrm{kV/cm}$ which is close to the onset[5] of impact ionization. Equation 5.8 implies that the drift velocity of holes would surpass the electron drift velocity above a certain electric field. For the best fitting parameters at $T = 313\,\mathrm{K}$ this would happen for $E > 60\,\mathrm{kV/cm}$.

[4]A process called impact ionization. For further reading see [21].
[5]Starting at $\overline{E} \approx 90$ kV/cm.

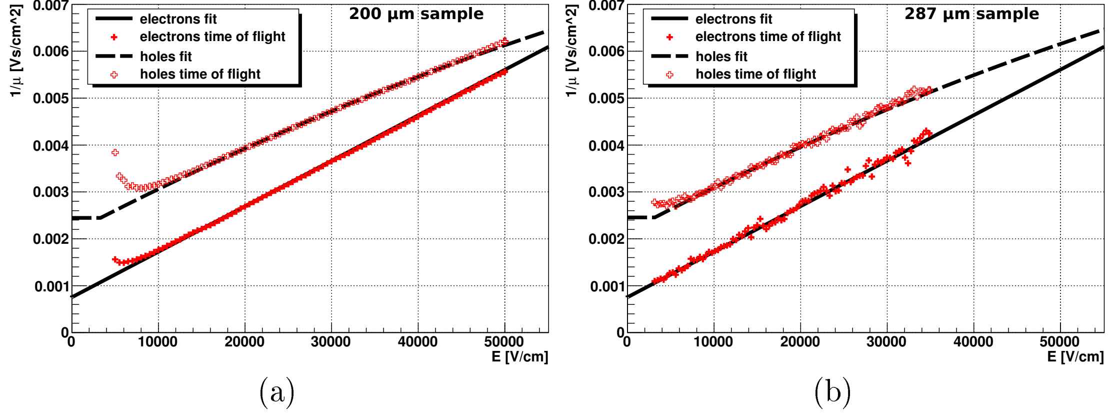

Figure 5.5.: Inverse mobility of electrons (solid lines) and holes (dashed lines) at $T = 313\,\mathrm{K}$ from the fit and the tof method (crosses) for the 200 µm sensor (a) and the 287 µm sensor (b).

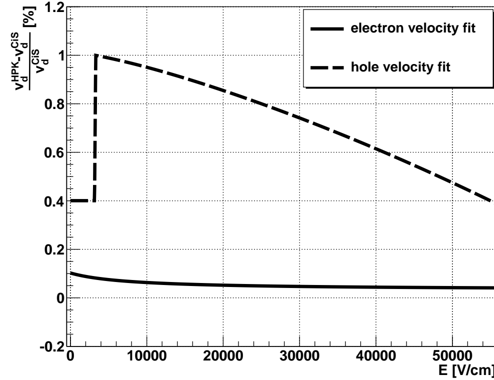

Figure 5.6.: Difference between the drift velocity of each sensor for the best fitting parameters at $T = 313\,\mathrm{K}$ as $\frac{v_d^{\mathrm{HPK}} - v_d^{\mathrm{CiS}}}{v_d^{\mathrm{CiS}}}$ in percent.

5.1.3.2. Comparison of the drift velocities obtained from different sensors

Figure 5.5 shows the results of the inverse mobility at $T = 313\,\mathrm{K}$ for both sensors investigated: the $w = 200\,\mu\mathrm{m}$ Hamamatsu (HPK) sensor and the $w = 287\,\mu\mathrm{m}$ CiS sensor. The results from the fit (lines) were obtained by fitting all measured U_{bias} at once and the tof results (crosses) were obtained for each current pulse at each U_{bias} separately. The results of the best fit are consistent with the tof results except for low electric fields, where the tof method is not applicable. Additionally, the difference between the results of the drift velocity $v_d(E) = E \cdot \mu(E)$ for both sensors is 1 % as shown in Figure 5.6.

The lower drift velocity of both electrons and holes observed for the CiS sensor suggests that the estimation of the sensor thickness is slightly wrong. Fixing the mobility parameters obtained for the 200 µm HPK sensor, the thickness is fitted as $w = 287.6\,\mu\mathrm{m}$ for the CiS sensor.

Due to the different thicknesses and depletion voltages of the sensors, the investigated range of the mean electric field was $\overline{E} = (5 - 50)\,\mathrm{kV/cm}$ for the 200 µm sensor and $\overline{E} = (2.4 - 35)\,\mathrm{kV/cm}$ for the 287 µm sensor. For both sensors the minimum electric field was $E_{min} \approx 0.7\,\mathrm{kV/cm}$ at the lowest bias voltage. However, only half of the sensor experiences $E < \overline{E}$ for the model of a linear electric field, and this model is least justified in the low field region (see section 4.3). Therefore, the sensitivity of the measurements was limited for $E < 5\,\mathrm{kV/cm}$ for the 200 µm sensor and for $E < 2.4\,\mathrm{kV/cm}$ for the 287 µm sensor.

It should be noted that the 287 µm CiS sensor was measured at a lower laser intensity and the measurement was corrected for the baseline (see section 5.3.1). Therefore, the signal-to-noise ratio is worse than for the 200 µm HPK sensor, which accounts for the higher statistical error of the tof results for the CiS sensor. Then again, the systematic error of the tof results is lower for the CiS sensor, especially at low electric fields. The higher thickness leads to longer current pulses and the lower N_{eff} leads to more uniform current pulses. Both effects improve the systematic error of the tof results.

5.1.3.3. Comparison of simulated and measured current pulse shapes

Here the simulated current pulses for the fit parameters obtained at $T = 313\,\mathrm{K}$ are compared to the measurements. In general, the measured current pulses for the different lasers are very well described by the new model, but some problems remain.

Electron drift

The pulse shapes for electron drift are shown in Figure 5.7. For both sensors the drift time is very well described except for the 200 µm sensor at $U_{bias} = 100\,\mathrm{V}$, where the duration of the simulated pulse is too long. The electric field seems to be different from the simulated linear field. Another reason could be an underestimation of the drift velocity of electrons at low electric fields; however, for the 287 µm sensor the drift at low fields is well described. Therefore, the assumption of a linear electric field might not be justified for the 200 µm sensor at $U_{bias} = 100\,\mathrm{V}$.

At high bias voltages the maximum and minimum values as well as the falling edge of the current pulse of the 200 µm sensor are not perfectly described. There are three possible explanations:
(i) The diffusion is calculated using the Einstein relation which is not valid for high electric fields. According to Jacoboni [17] the diffusivity of electrons in silicon

is highly anisotropic. At high fields the diffusivity is probably underestimated and the Einstein relation is a worse approximation for the <100> orientation than for the <111> orientation. A better description of the current pulses can be achieved by increasing the diffusion constant at high fields (χ^2 is reduced by more than 50 %). However, the diffusion was not further investigated.
(ii) Charge carriers are generated not only in the active bulk of the sensor, but in the front p^+ implant as well. The lifetime of the electrons generated in the front implant might be sufficient for the carriers to diffuse, with a certain delay, into the active, depleted region where the electric field is present. The minority carrier lifetime of electrons is in the order of a few nanoseconds at room temperature for $N_{eff} \approx 10^{19}\,\mathrm{cm}^{-3}$ [27]. Therefore, some charge carriers are released with a delay from the implant and contribute to the current pulse.
(iii) The response function was determined for illumination with the infrared laser. The time spectra of the laser pulses are slightly different for the red and the infrared lasers. There might be an afterpulse for the red laser that leads to a delayed carrier generation (see appendix A.1 for the laser profiles). The documentation [6] of the red laser shows a time spectrum recorded with a streak camera not exhibiting an afterpulse, and a time spectrum recorded with an oscilloscope exhibiting an afterpulse. For the oscilloscope measurement the afterpulse is delayed by about 45 ps and the maximum intensity is about 17 % of the main pulse.

All these effects should be seen for hole drift as well, but to a lesser extent since the duration of the current pulses is slightly longer. Additionally, plasma effects (see hole drift below) could be an explanation, but no evidence of plasma effects was found at low U_{bias} for electron drift.

Hole drift

For the hole drift (Figure 5.8) the drift time and the response function describe the measurements very well. Noticeable differences arise for the 200 µm sensor. The ringing effect after the signal is overestimated for $U_{bias} > 100\,\mathrm{V}$ which is seen for electron drift as well. The reason for this is not clear. The initial rise is not well described at intermediate U_{bias}. This is probably caused by a wrong attenuation coefficient α_s for the red laser light of $\lambda = 675\,\mathrm{nm}$. The description of the measurement is improved (for electron drift as well) by adjusting α_s ($-20\,\%$ at $T = 313\,\mathrm{K}$).

The differences between the simulation and the measurement at high U_{bias} are much lower than for the electron drift. Therefore, the points discussed for electron drift can be evaluated:

(i) There is no data in the literature that we know of for the diffusivity of holes in <100> direction at high fields. But the approximation of using the Einstein relation seems to be sufficient for our purpose.
(ii) The minority carrier lifetime of holes in the rear n^+ implant is in the order of a few 100 ps at room temperature for $N_{eff} \approx 10^{19}\,\mathrm{cm}^{-3}$ [25]. Therefore, it is much shorter than the lifetime of electrons in the front implant. Additionally, the diffusivity of holes is lower than that of electrons. The effect of delayed diffusion of charge carriers from the implant to the depleted region is probably less pronounced for holes than for electrons.
(iii) The difference between the time spectra of the red and infrared laser is probably a minor issue. Evidence of a possible afterpulse is not observed.

At $U_{bias} = 100\,\mathrm{V}$ the plasma effect is possibly visible. A high charge carrier density[6] modifies the electric field. The inner region of the charge cloud generated by the laser pulse is shielded from the external field[7]. There is no evidence for plasma effects for the 287 µm sensor which was measured at low laser intensity, hence low charge carrier density. However, this effect could be partly attributed to a wrong electric field model for the 200 µm sensor at $U_{bias} = 100\,\mathrm{V}$ as discussed for electron drift.

Infrared illumination

For the infrared laser the same laser intensity was used for both sensors. The charge carriers are generated over the whole thickness of the sensor instead of just the first few micrometer as with the red laser. The charge carrier density is low and plasma effects are not expected. Only a small fraction of the charge carriers is generated outside the active area. Therefore, diffusion of charge carriers from the implants into the depleted region is negligible. Figure 5.9 shows the current pulses. The difference between the measurements and the simulations is small except for the 287 µm sensor at $U_{bias} = 100\,\mathrm{V}$ there a kink is observed in the measured current pulses at $t \approx 10\,\mathrm{ns}$. The reason is probably a wrong synchronization of the baseline since the kink disappears if the baseline is not corrected for (the baseline is shown in fig. 5.13). There might have been problems with the trigger for this measurement, as the red and the infrared lasers use different trigger units and the baseline was measured with the trigger unit of the red laser. Nevertheless, baseline correction was used for this measurement since the global match of the measurement and the simulation was improved.

[6] $N_{e,h} \approx 5 \cdot 10^{12}\,\mathrm{cm}^{-3}$ for the red laser at standard intensity.
[7] For further reading see [33].

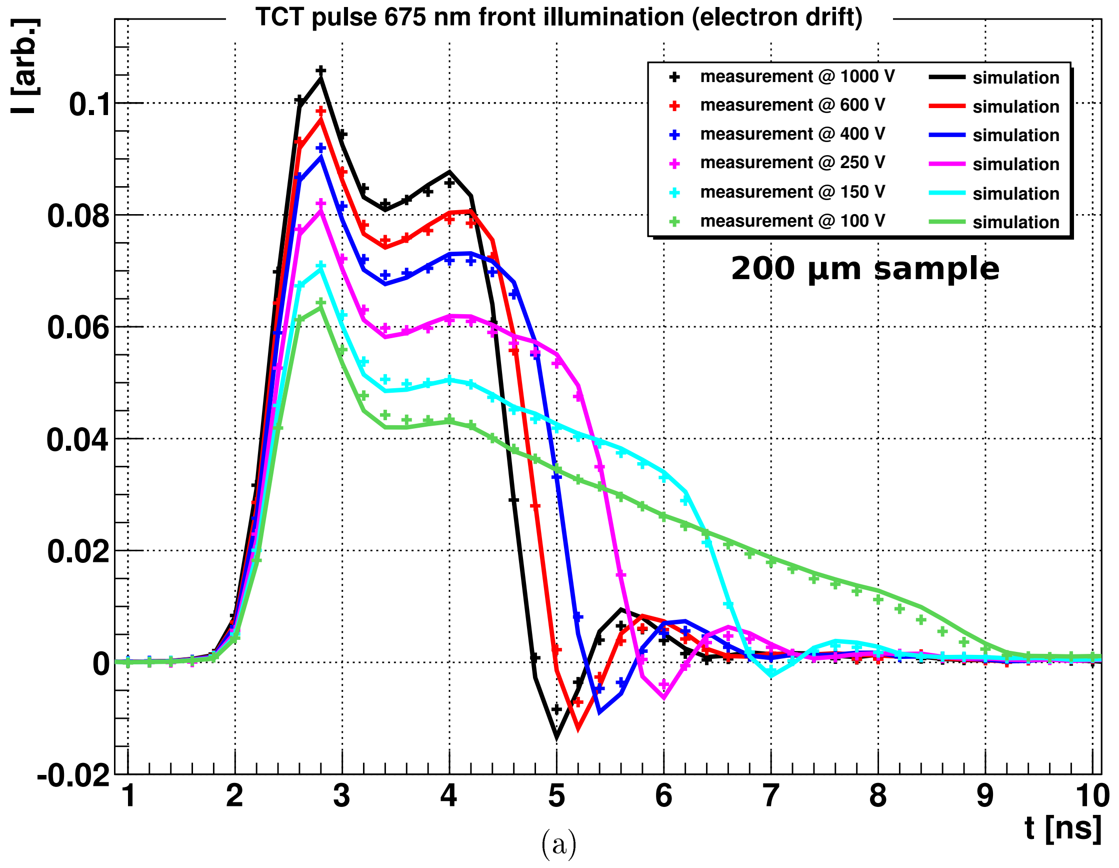

(a)

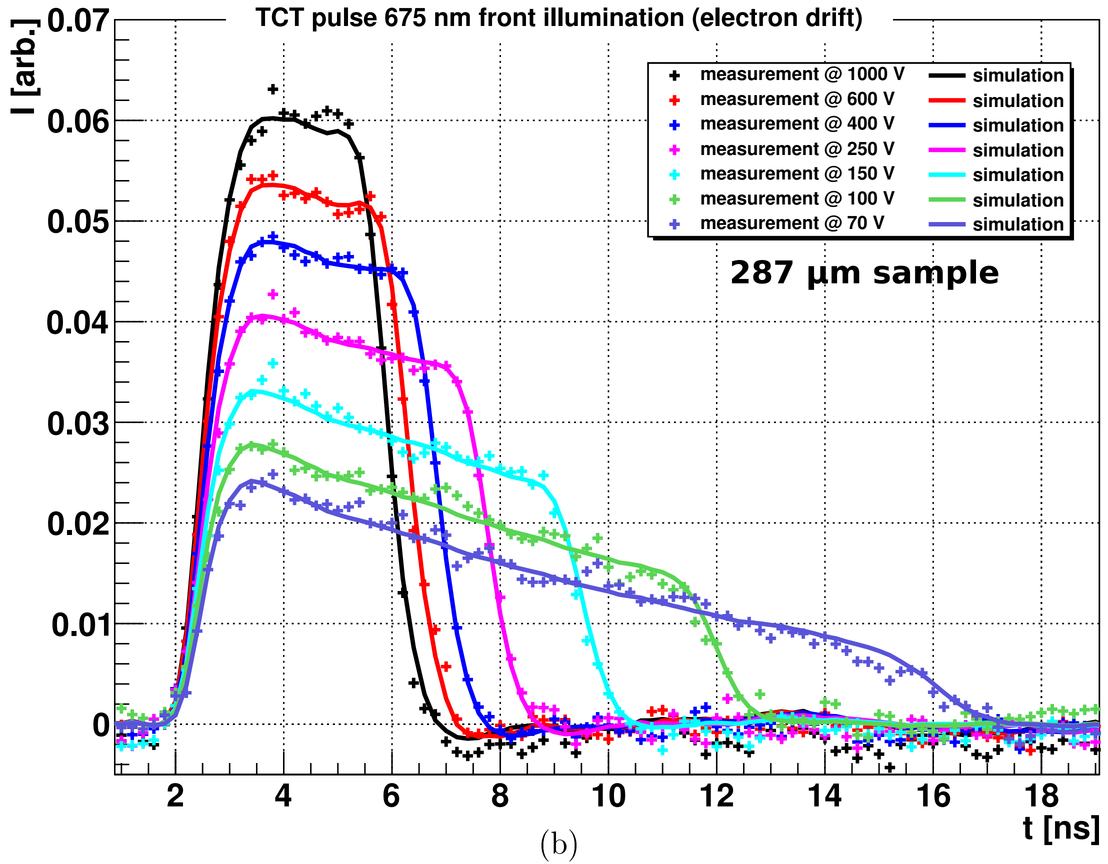

(b)

Figure 5.7.: TCT spectra (crosses) and drift simulation (lines) with the parameters obtained from the fit for electron drift at different bias voltages for the 200 µm sensor (a) and the 287 µm sensor (b).

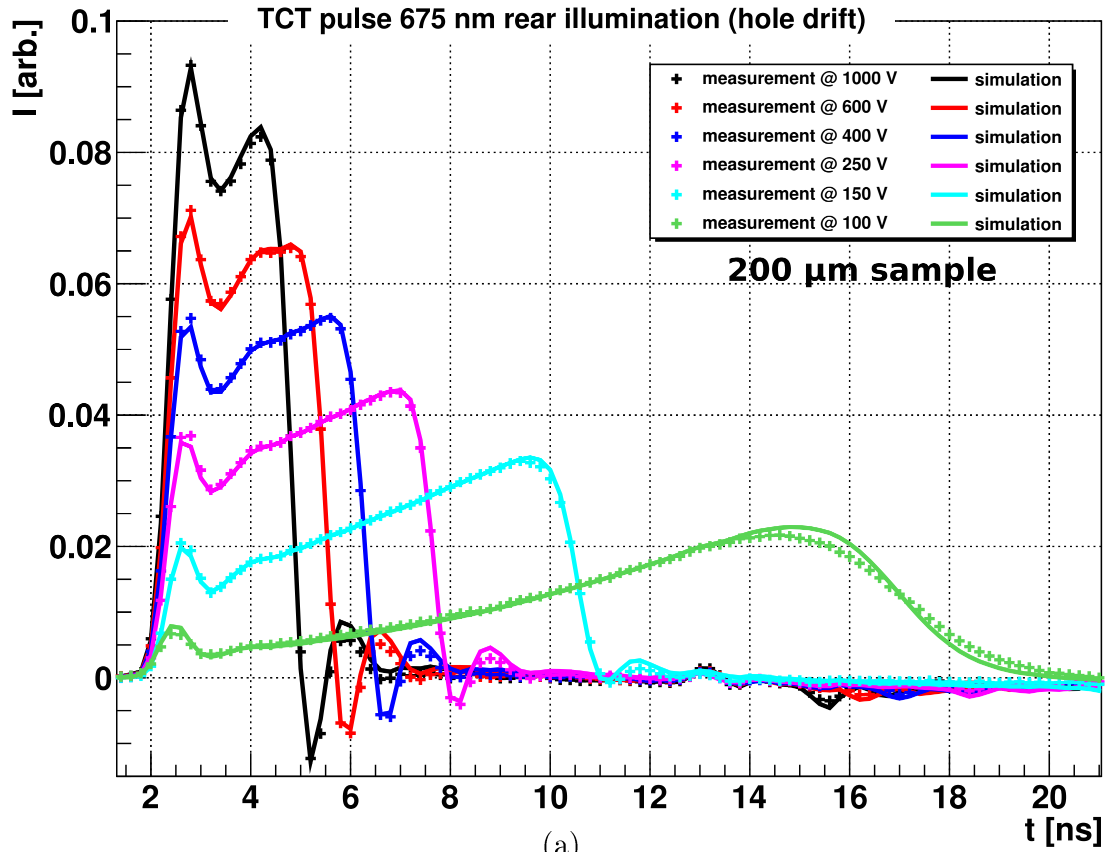

(a)

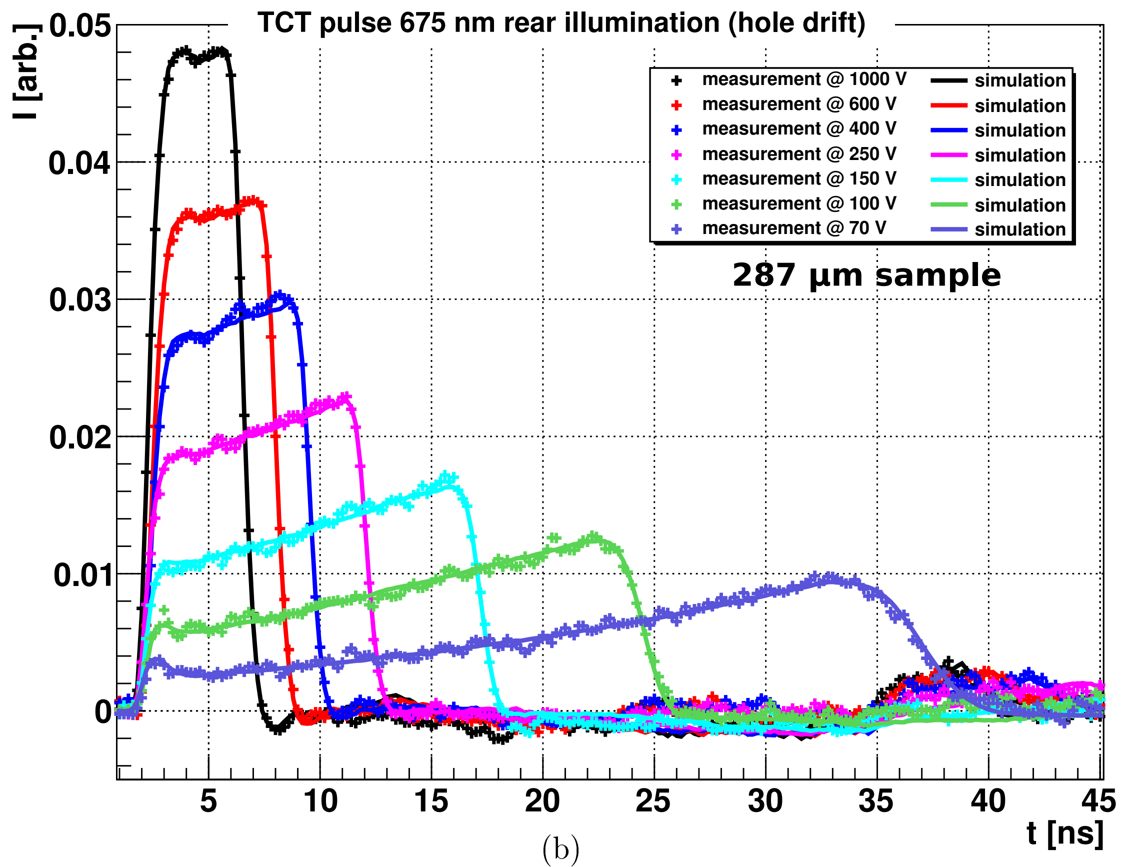

(b)

Figure 5.8.: TCT spectra (crosses) and drift simulation (lines) with the parameters obtained from the fit for hole drift at different bias voltages for the 200 µm sensor (a) and the 287 µm sensor (b).

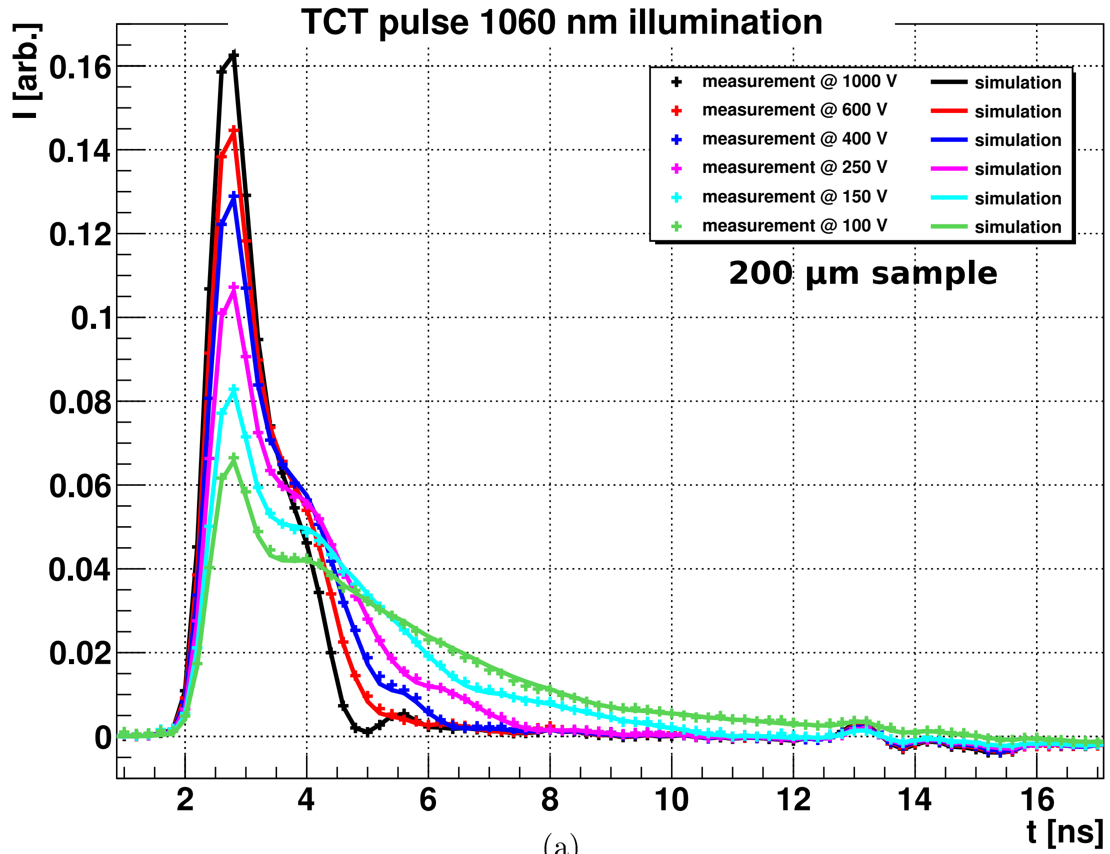

(a)

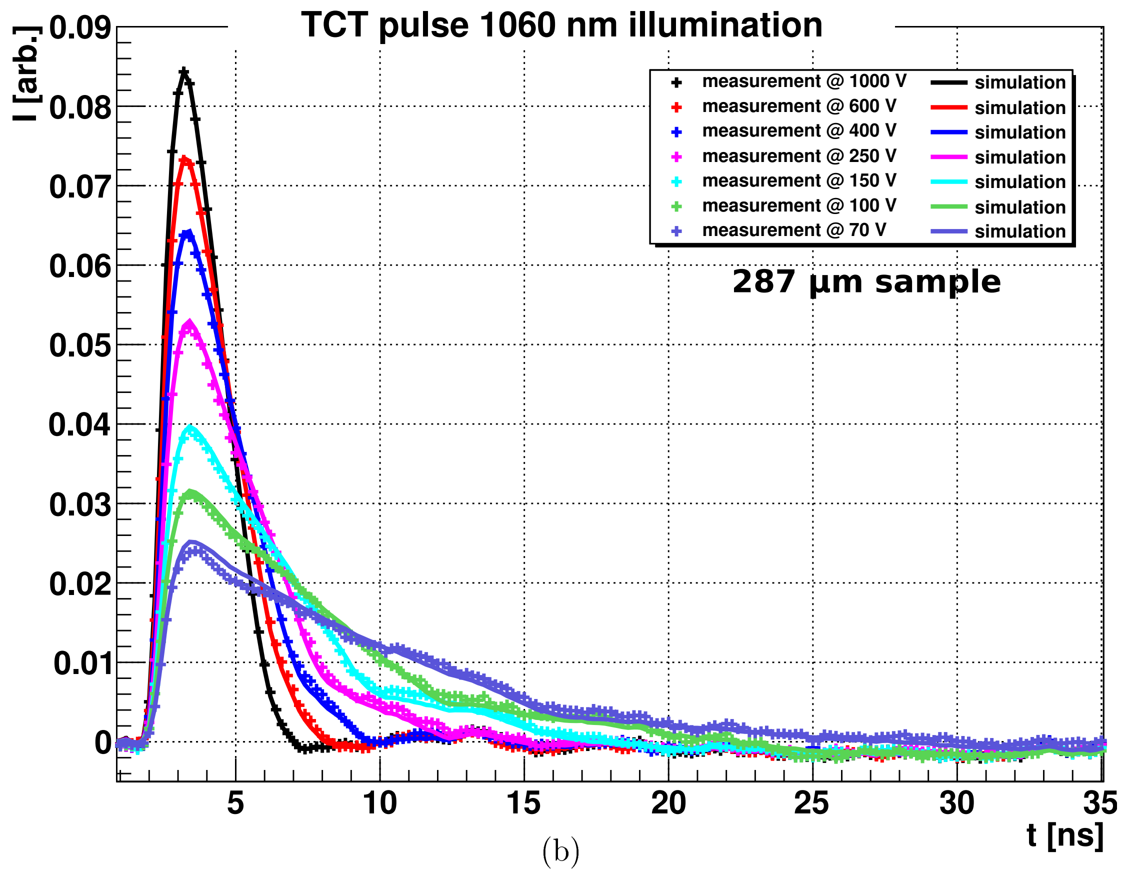

(b)

Figure 5.9.: TCT spectra (crosses) and drift simulation (dashed lines) with the parameters obtained from the fit for illumination with the infrared laser resulting in simultaneous electron and hole drift at different bias voltages for the 200 µm sensor (a) and the 287 µm sensor (b).

5.2. Temperature dependence

The temperature dependence of the charge drift parameters was investigated for the 200 µm HPK sensor between $T = 233\,\mathrm{K}$ and $T = 333\,\mathrm{K}$ in steps of $\Delta T = 20\,\mathrm{K}$ and, additionally, for $T = 263\,\mathrm{K}$. The measurements were performed at bias voltages ranging from $U_{bias,min} = 100\,\mathrm{V}$ to $U_{bias,max} = 1000\,\mathrm{V}$ in steps of $\Delta U_{bias} = 10\,\mathrm{V}$[8]. The only exceptions were the following measurements

$T = 233\,\mathrm{K}$: $U_{bias,max} = 880\,\mathrm{V}$
$T = 263\,\mathrm{K}$: $U_{bias,max} = 980\,\mathrm{V}$
$T = 273\,\mathrm{K}$: $U_{bias,max} = 990\,\mathrm{V}$

For these measurements at low temperature remaining humidity led to an early breakdown. A short circuit was generated at high voltages by a thin layer of ice on the surface of the sensor. The current pulse shapes before breakdown were not affected by the layer of ice.

5.2.1. Single temperature results

At first the fit parameters were obtained for single temperatures[9]. For electrons the measurements were not sensitive to the constant part of the mobility in the investigated electric field and temperature range. Therefore, the expected constant low field part of the electron mobility is neglected ($E_0 = 0$) and the parametrization (eqn. 5.4) becomes

$$\mu_e(E) = \frac{\mu_0^e}{1 + \frac{\mu_0^e}{v_{sat}^e} \cdot E} \qquad (5.9)$$

the Trofimenkoff formula.

5.2.2. Global fit results

The temperature dependence of the mobility parameters was parametrized, according to literature [8, 17, 26], using a power law

$$par_i(T) = par_i(T = 300\,\mathrm{K}) \cdot \left(\frac{T\,[\mathrm{K}]}{300\,\mathrm{K}}\right)^{\alpha_i} \qquad (5.10)$$

where the values at room temperature $par_i(T = 300\,\mathrm{K})$ and the exponents α_i were used as fit parameters. The quadratic parameter c of the hole mobility was chosen independent of T. A certain temperature dependence of c would introduce another fit parameter and even stronger correlations between the parameters.

[8]Corresponding to a mean electric field between $\overline{E}_{min} = 5\,\mathrm{kV/cm}$ and $\overline{E}_{max} = 50\,\mathrm{kV/cm}$.
[9]See sections 5.1.3.2 and 5.1.3.3 for the results at $T = 313\,\mathrm{K}$.

		$par_i(T = 300\,\mathrm{K})$	α_i
Electrons	μ_0^e	$1430\,\mathrm{cm^2/Vs}$	-1.99
	v_s^e	$1.05 \cdot 10^7\,\mathrm{cm/s}$	-0.302
Holes	μ_0^h	$457\,\mathrm{cm^2/Vs}$	-2.80
	b	$9.57 \cdot 10^{-8}\,\mathrm{s/cm}$	-0.155
	c	$-3.24 \cdot 10^{-13}\,\mathrm{s/V}$	-
	E_0	$2970\,\mathrm{V/cm}$	5.63

Table 5.1.: The mobility parameters of eqn. 5.8, eqn. 5.9, and eqn. 5.10 for silicon of <100> orientation determined for electric field values ranging from $E = 5\,\mathrm{kV/cm}$ to $E = 50\,\mathrm{kV/cm}$ at temperatures between $T = 233\,\mathrm{K}$ and $T = 333\,\mathrm{K}$.

All bias voltages, all laser illumination types, and all temperatures were fitted simultaneously amounting in $1.6 \cdot 10^5$ measurement points. The results of the global fit are listed in Table 5.1[10].

Figure 5.10 shows the differences $\frac{v_d^{global} - v_d^{single}}{v_d^{single}}$ and $\frac{v_d^{global} - v_d^{tof}}{v_d^{tof}}$ between the drift velocity from the global temperature fit v_d^{global} (tab. 5.1) and both v_d^{single} and v_d^{tof}, from the single temperature fits and the tof method respectively. The drift velocity results from the single T fits are not constrained by a parametrization of the temperature dependence. Therefore, the drift velocity from the single T fits is expected to show a better match with the tof results than v_d^{global}. This is not seen for the electron drift velocity (continuous lines, filled crosses). Here the power law approximation (eqn. 5.10) is apparently very accurate. On the other hand, for holes the drift velocity from the single T fits shows a better match with the tof results than the global T fit results (dashed lines, open crosses). For the hole mobility parameters the power-law approximation is not as accurate as it is for the electron parameters.

The drift velocity from the tof method, that is sufficiently accurate only for $E > 15\,\mathrm{kV/cm}$, is systematically about 0.5 % higher than v_d^{global} for both electrons and holes. In the investigated electric field range the difference between v_d^{global} and both v_d^{single} and v_d^{tof} is always below 3 %. For electrons the difference between the results of the global T fit and the single T fits is below 1 %. For holes the difference is below 3 %. Limited sensitivity of the measurement and strong correlation between the parameters μ_0^h and E_0 of the hole mobility lead to large differences for $E < 5\,\mathrm{kV/cm}$. At low temperatures ($T < 273\,\mathrm{K}$) both the single T and the tof results exhibit a higher hole drift velocity at high electric fields. Here the approach of $c(T) = const$ is probably not justified.

[10]See appendix A.2 for the correlation matrix of the fit.

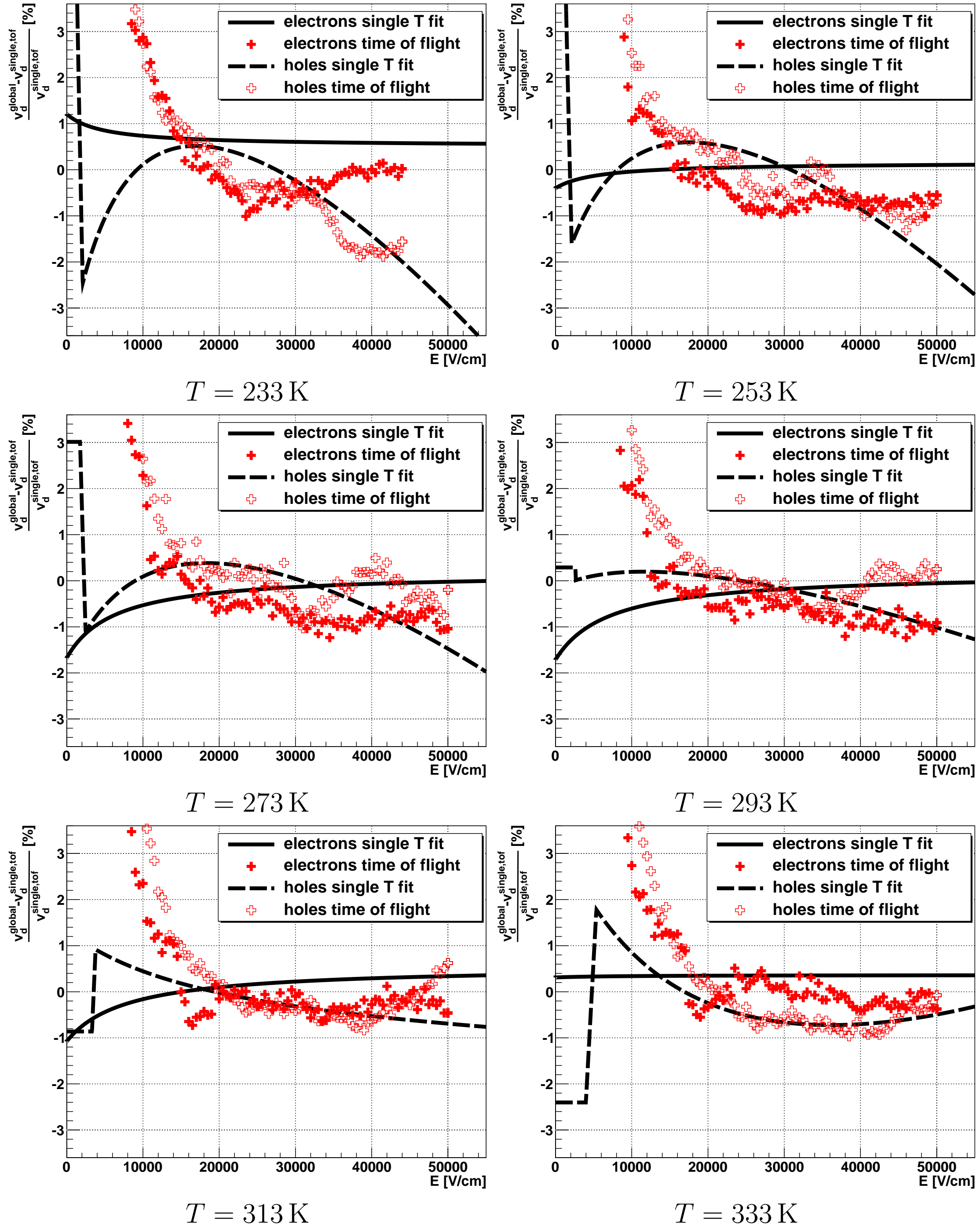

Figure 5.10.: The drift velocity from the global T fit is compared to the results of the single T fits as $\frac{v_d^{global} - v_d^{single}}{v_d^{single}}$ (lines) and to the tof results as $\frac{v_d^{global} - v_d^{tof}}{v_d^{tof}}$ (crosses) in percent. The differences are always below 3 % in the electric field ranges of $\overline{E} = (5 - 50)\,\mathrm{kV/cm}$ for v_d^{single} and $\overline{E} = (15 - 50)\,\mathrm{kV/cm}$ for v_d^{tof}.

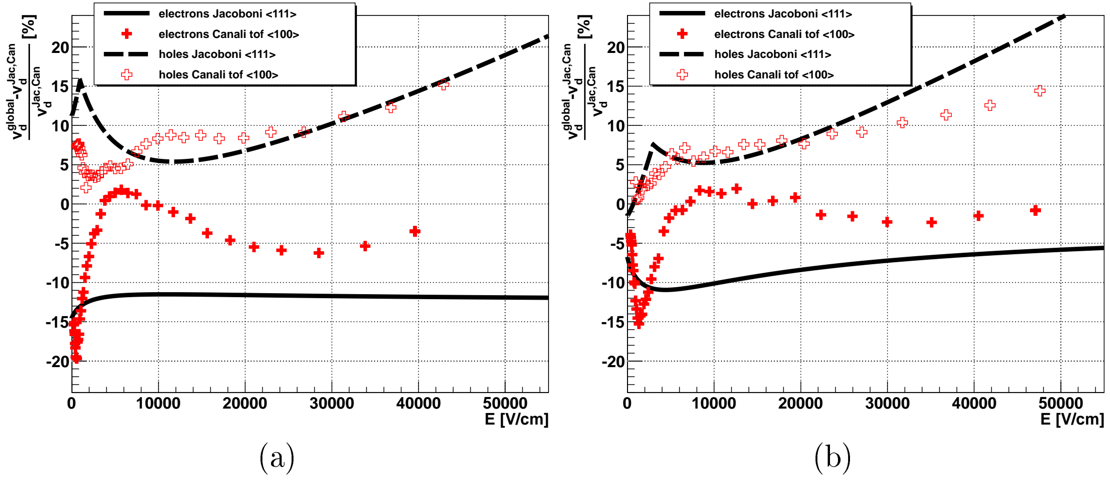

Figure 5.11.: Differences $\frac{v_d^{global}-v_d^{Jacoboni,Canali}}{v_d^{Jacoboni,Canali}}$ [%] of v_d^{global} and both the drift velocity by Jacoboni for the <111> orientation (lines) and the tof measurements by Canali for the <100> orientation (crosses) at $T = 245\,\mathrm{K}$ (a) and at $T = 300\,\mathrm{K}$ (b).

The measured transient current pulse shapes for both lasers and the simulated pulse shapes for the global fit results (tab. 5.1) at all temperatures and selected U_{bias} are shown in appendix A.3. Additionally, the measurements of the 287 µm sensor at $T = 313\,\mathrm{K}$ are compared to the simulation with the global fit results (fig. A.14 and fig. A.15).

5.2.3. Comparison with the literature values

The parameters by Jacoboni et al. [17] for the <111> crystal orientation are most widely used for the simulation of silicon devices. These parameters (using eqn. 5.1) are based on the <111> tof measurements by Canali et al. [10] who published measurements for the <100> orientation as well.

Figure 5.11 shows the differences $\frac{v_d^{global}-v_d^{Jacoboni}}{v_d^{Jacoboni}}$ and $\frac{v_d^{global}-v_d^{Canali}}{v_d^{Canali}}$ between the global fit results and both the <111> Jacoboni values and the <100> measurements by Canali. It should be noted that these values do not represent the actual measurements by Canali but values that were extracted from the plots of the original publication [10]. There might be differences of up to 5 % between these values and the actual measurements since the original plots are in logarithmic scale spanning several orders of magnitude. Nevertheless, the extracted Canali <100> values are compared to the fit results. In the investigated electric field range the extracted electron drift velocity from Canali is up to 6 % higher than our fit values at $T = 245\,\mathrm{K}$ and consistent with the fit values at $T = 300\,\mathrm{K}$. For $E < 5\,\mathrm{kV/cm}$ the electron drift velocity from Canali is significantly higher than our values for both temperatures. Our measurements were not sensitive to the constant low field

mobility of electrons which is clearly seen in the Canali values at $T = 300\,\mathrm{K}$ for $E < 1.3\,\mathrm{kV/cm}$ (see fig. 5.3). The hole drift velocity extracted from the Canali plots is at least 5 % lower than our results for $E > 5\,\mathrm{kV/cm}$ and shows a maximum difference of 14 % at $E \approx 50\,\mathrm{kV/cm}$.

A significant difference between the fit and the Jacoboni <111> values is observed. At $T = 245\,\mathrm{K}$ and $T = 300\,\mathrm{K}$ the Jacoboni values of the electron drift velocity are at least 6 % higher than our results. The hole drift velocity is more than 5 % lower than our results and shows a maximum difference of 24 %. This was expected due to the anisotropy of the charge carrier drift velocity in silicon.

The electron drift velocity for the Jacoboni <111> parameters is similar to the extracted <100> values from Canali at $E \approx 0$, but less at high fields[11]. For the hole drift velocity the Jacoboni values are similar to the Canali values even at high fields at both temperatures. This was not expected since the difference between the hole drift velocity for the <111> and for the <100> orientation is about 15 % at high fields in the Canali measurements.

While the differences between our results for the <100> orientation and the Jacoboni <111> values were expected, the differences between our results and the Canali <100> values were not. The measurements performed by Canali et al. were similar to our measurements. Canali used high resistivity $\rho = (30 - 200)\,\mathrm{k\Omega cm}$ surface barrier n-type diodes without implants. The capacitance of the diodes is given as 1 pF. The rise time of the electronics is given as 100 ps which is $5 - 8$ times faster than our setup. For the time of flight t_{tof} the full width at half maximum of the current pulses was determined rather than the points of maximum slope. Short pulses (70 ps) of $E_k = 40\,\mathrm{keV}$ electrons with a penetration depth of 7 µm in silicon were used for the generation of charge carriers instead of lasers. A pulsed bias voltage rather than continuous U_{bias} was applied. Both the high resistivity of the sensors and the fast rise time of the setup used by Canali are beneficial with respect to the determination of the charge carrier drift velocity. However, this does not explain the differences observed between the hole drift velocities concerning the similar results for the electron drift velocities.

Figure 5.12 shows the differences $\frac{v_d^{global} - v_d^{Becker}}{v_d^{Becker}}$ and $\frac{v_d^{global} - v_d^{Canali}}{v_d^{Canali}}$ between the fit results and both the drift velocity for the <100> crystal orientation determined by Becker et al. [8] and the Canali <100> measurements. Becker investigated three different electric field values $\overline{E} = (3.8,\ 7.1,\ 17.9)\,\mathrm{kV/cm}$. At these particular electric field values the maximum difference between our values and the Becker

[11] Canali proposed $\mu_0^{e,h}$ and v_s^e to be independent of the crystal orientation.

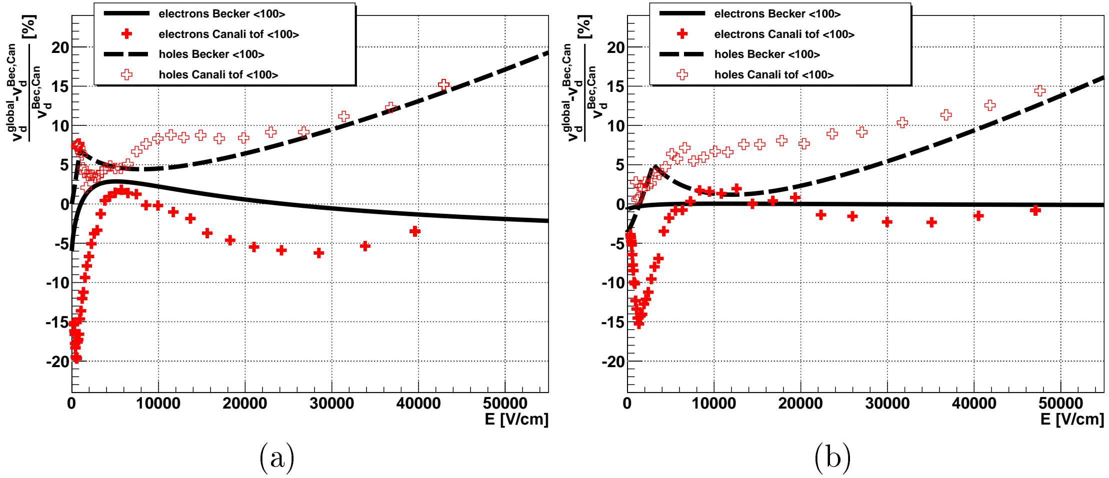

(a) (b)

Figure 5.12.: Differences $\frac{v_d^{global} - v_d^{Becker,Canali}}{v_d^{Becker,Canali}}$ [%] of v_d^{global} and both the drift velocity for the Becker parameters (lines) and the Canali tof values (crosses) both for <100> orientation at $T = 245\,\mathrm{K}$ (a) and at $T = 300\,\mathrm{K}$ (b).

values is 3 % for the electron drift velocity and 6 % for the hole drift velocity. At $T = 300\,\mathrm{K}$ the electron drift velocity determined by Becker matches with our values in the whole electric field range investigated here (the maximum difference is 0.2 %). The drift velocity Becker determined shows a better match with the Canali values than our fit results for both electrons and holes. The same simulation was used for Becker's results and the results of this thesis, but Becker did not acquire the time of flight. Becker investigated a CiS sensor similar to the 287 µm sensor we used, but with a considerably higher oxygen concentration.

5.3. Discussion

The mobility parameters obtained in this thesis describe the measured current pulses and match with the tof results of the current pulses. Comparison with literature data shows significant differences, though. The maximum difference between the electron drift velocity determined here and the values from Canali is 6 % at $T = 245\,\mathrm{K}$ and 2 % at $T = 300\,\mathrm{K}$ in the electric field range we investigated. For the Becker values the maximum difference is 3 % at $T = 245\,\mathrm{K}$ and 0.2 % at $T = 300\,\mathrm{K}$. Both the Canali and the Becker values exhibit a higher electron drift velocity at high fields. On the other hand, the hole drift velocity determined by Canali and Becker is at least 1 % lower than our values in the investigated electric field range both at $T = 245\,\mathrm{K}$ and $T = 300\,\mathrm{K}$. The maximum difference is 14 % at high fields. The difference between the literature values and our results is much smaller for the electron drift velocity than for the hole drift velocity, and the sign of the deviations is different for electrons and for holes. The reason for the higher

hole drift velocity we observed is not clear and the results should be confirmed by other experiments.

Due to the limited electric field range $\overline{E} = (5 - 50)\,\mathrm{kV/cm}$ that was investigated here, the fit parameters $\mu_0^{e,h}$ were not directly accessible and may not be confused with the literature values of the low field mobility. The parametrization we used for the mobility and for the temperature dependence of the mobility parameters is only an approximation. Especially for the temperature dependence of parameter E_0 of the hole mobility the power law approximation might not be justified. The results of the single temperature fits show large deviations of up to 66 % from the global fit results for this parameter. Additionally, the parameters are strongly correlated. For the single temperature fits the maximum difference between the low field mobility of holes determined by Jacoboni and the fit parameter μ_0^h was 5 %. In contrast, the maximum difference was 15 % for the global fit results. Therefore, extrapolation beyond the investigated electric field and temperature range may yield significantly wrong results. The Canali measurements suggest the electron drift velocity at low fields to be up to 20 % higher than the fit values. For the hole mobility the parameter c of the quadratic term (eqn. 5.8) prevents the hole drift velocity from saturation at high electric fields. Consequently, the mobility parametrization is probably not suitable for $E < 5\,\mathrm{kV/cm}$ and, especially for holes, for $E > 50\,\mathrm{kV/cm}$ with the parameters we determined. The current pulses of the 287 µm sensor are well described (±3 %) at $\overline{E} = 2.4\,\mathrm{kV/cm}$, though.

Concerning our results as well as the Canali values for the <100> direction, the inverse mobilities of electrons and holes are expected to be constant at low fields. Above a certain electric field the slope is expected to increase. At high electric fields the slope is expected to decrease, and finally to approach the inverse saturation velocity $1/v_s^{e,h}$. A more sophisticated parametrization of the charge carrier mobility would be needed in order to describe these hypothetical properties.

5.3.1. Sources of error

Sensor thickness

The uncertainty of the sensor thickness is estimated to be 1 % for both samples since the thickness determined for the HPK sensor is supposed to be very accurate (see sec. 3.1). Additionally, the difference between the results of the electron drift velocity for both sensors is only 0.1 % (fig. 5.6). For the tof results an error of 1 % for the thickness corresponds directly to a systematic error of ±1 % regarding the drift velocity. For the fit results the situation is slightly different mainly because the parametrization is not optimal and the parameters are correlated. A global fit

of the mobility for $w\pm1\,\%$ yields a maximum deviation of the drift velocity of $\pm2\,\%$. Therefore, the systematic error of the drift velocity related to the uncertainty on the sensor thickness is estimated to 2 % for the fit results.

Temperature

The error of T is estimated to $\pm0.5\,$K (see section 3.2.3). However, there might have been systematic differences of up to $+2\,$K at $T = 233\,$K because the setup was constantly flooded with room temperature dry air. The resulting error of the drift velocity for the fit and the tof results is estimated to be $^{+0.3}_{-1.7}\,\%$ at $T = 233\,$K and $\pm0.3\,\%$ for $T \geq 253\,$K.

Plasma effect

Plasma effects were supposedly observed for the hole drift at low U_{bias} for the 200 µm sensor, but not for the 287 µm sensor. The maximum difference between the hole drift velocities determined for both sensors was 1 % at low fields. Therefore, the influence of the plasma effect on the determined drift velocity is estimated to be less than 1 % for the fit. The tof values for low U_{bias} are not used.

Electric field

With the approximation of constant N_{eff} a linear electric field model is used in the simulation. However, at low bias voltages the electric field is probably not linear anymore (see section 4.2.2). Differences between the measured and the simulated current pulse shapes at low U_{bias} were observed for the 200 µm sensor. Differences were observed for both electron and hole drift. The observed differences for hole drift might be partly attributed to plasma effects. For the 287 µm sensor the current pulses at low U_{bias} are well described. The maximum difference between the drift velocities determined for both sensors was 0.1 % and 1 %, for electrons and holes respectively. Therefore, the error related to the electric field model is estimated to be less than 1 % for the fit results.

Initial charge distribution

The attenuation coefficient $\alpha_s(T)$ is not well known for both the red and the infrared laser. However, the measured current pulse shapes are well described by the model, and a variation of the attenuation parameters shows little impact on the fit results. For the infrared laser the attenuation length is comparable to the sensor thickness at high temperatures and reflection at the rear of the sensor might be an issue. Again, little impact on the fit results was seen for a variation of the

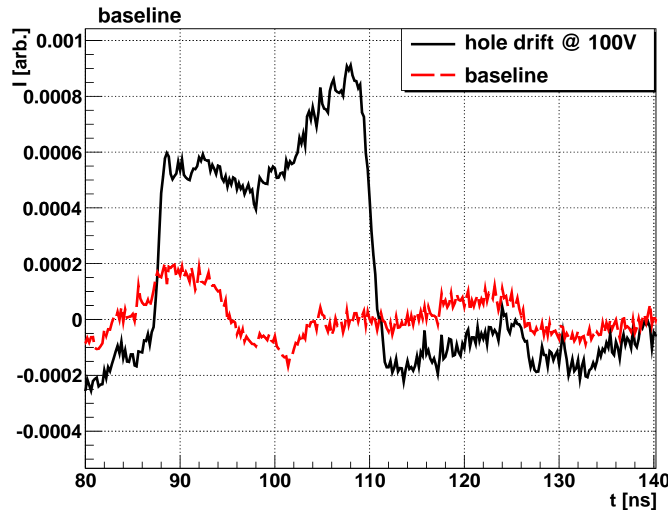

Figure 5.13.: Average baseline (4092 measurements at 8 different U_{bias}) recorded for the 287 µm sensor (dashed line) and the current pulse for hole drift without baseline correction at $U_{bias} = 100$ V (continuous line).

reflection coefficient. For this reason, reflection was neglected. The resulting error of the fit results is estimated to be less than 1 %.

Baseline

For the $w = 287$ µm sensor TCT measurements were performed at very low laser intensity. The noise in the obtained current pulses is higher than for the $w = 200$ µm sensor since less charge is deposited and the sensor is thicker[12]. Additionally, systematic modulations of the baseline of the setup (see Figure 5.13) have proved problematic; consequently, this was accounted for. The baseline was obtained performing a measurement without connecting the laser light fiber. Several measurements were averaged and the baseline was subtracted from the TCT measurements of the 287 µm sensor. Modulations in the current pulses were strongly diminished, but the noise, which was rather high anyway, was slightly increased.

The baseline was not subtracted for the 200 µm sensor. Since the laser intensity was higher than for the measurements performed with the 287 µm sensor the effects of a possible baseline modulation are small compared to the signal and were neglected.

Response function

The response function was determined in several iterations from the transient current pulse for illumination with the infrared laser at $T = 313$ K and $U_{bias} = 1000$ V. First the response function was obtained with the literature mobility values. Then

[12]The induced current is $I \propto q/w$.

the mobility parameters of the new parametrization were fitted. Again the response function was determined and the mobility parameters were fitted. This was repeated until the results were stable after just two to three iterations. Different initial mobility models and model parameters yield similar results within 0.1 %. However, clearly there are differences in the goodness of the description of the current pulse shapes for illumination with the red laser (front and rear) and infrared illumination. This difference is probably due to the three effects discussed in section 5.1.3.3. The error introduced by these effects is supposedly negligible since the length of the current pulses is, at the most, slightly prolonged. Additionally, the measurements with both lasers are simultaneously used for the fit. But the impact of these effects on the drift velocity was not fully evaluated.

As discussed earlier, the attenuation coefficient is not well known and reflection might be an issue for $T \geq 313\,\mathrm{K}$ where $\alpha_s^{-1} \approx w$. Therefore, a wrong initial charge distribution might have been used for the determination of the response function. A global fit using the response function determined at $T = 253\,\mathrm{K}$ showed a maximum deviation of the drift velocity of 0.25 % compared to the results for the response function determined at $T = 313\,\mathrm{K}$[13]. However, the global description of the current pulses was better for the response function determined at $T = 253\,\mathrm{K}$ and χ^2 was reduced by 20 %. Unfortunately, this was noticed late and because of the similar results the response function determined at $T = 313\,\mathrm{K}$ was used.

The main contribution to the response function is from the capacitance of the sensor under test. The capacitance is supposed to be constant for $U_{bias} > U_{dep}$. However, it is slightly decreasing with increasing U_{bias}. Capacitance measurements have shown a change of $C(U_{bias} = 100\,\mathrm{V}) - C(U_{bias} = 1000\,\mathrm{V}) = 0.14\,\mathrm{pF}$ corresponding to 4.5 % for the $w = 200\,\mu\mathrm{m}$ sensor. The corresponding error is supposedly insignificant, though. Most of the change of the capacitance happens for low U_{bias}. The transient current pulses at low U_{bias} are slow; therefore, they are less affected by the response of the electronic circuit. In conclusion, the error of the drift velocity from the fit introduced by the response function is estimated to be 1 %.

Synchronization and binning

The cell size was $\Delta x = 100\,\mathrm{nm}$ for all simulations discussed here. In some cases at low U_{bias} and high T the condition $v_d \cdot \Delta t > \Delta x/2$ was not true for hole drift (for example at $U_{bias} = 100\,\mathrm{V}$ and $T = 333\,\mathrm{K}$ for about 9 % of the sensor width).

[13] At $T = 253\,\mathrm{K}$ the initial charge distribution is essentially constant within the sensor and independent of reflection since $\alpha_s^{-1} \gg w$.

Here rounding errors are introduced. However, insignificant differences in the pulse shape, the pulse duration, and χ^2 are seen when decreasing Δx.

For the fit the simulation and the measurement are synchronized in steps of the time step size of the simulation $\Delta t = 10\,\mathrm{ps}$. Therefore, the accuracy of the fit is limited[14] and discontinuities in χ^2 arise if the variation of a parameter changes the synchronization at a certain U_{bias} at a certain T for one time step Δt. Because of the large amount of measurements the discontinuities supposedly do not influence the fit result, at least if only single measurements are affected. However, for a realistic error estimation the fit algorithm did not converge, possibly due to these discontinuities. Additionally, the sample acquisition time of the oscilloscope is assumed to be infinitely short and the instant values at the center of a time bin of the simulation were used to calculate χ^2. The resulting error on the drift velocity is estimated to be 1 %.

Summary of the errors

The squared sum of the errors discussed here[15] results in an error of $\pm 1.5\,\%$ at $T = 293\,\mathrm{K}$ and of $^{+1.5}_{-2.3}\,\%$ at $T = 233\,\mathrm{K}$ for the drift velocity determined with the tof method for $\overline{E} \geq 15\,\mathrm{kV/cm}$. This is only true for the 200 µm sensor, for the 287 µm sensor the error is about $\pm 4\,\%$ due to higher noise.

For the fit results the summed error of the drift velocity is $\pm 2.5\,\%$ at $T = 293\,\mathrm{K}$ and $^{+2.5}_{-3.0}\,\%$ at $T = 233\,\mathrm{K}$. The statistical error is supposedly negligible since the amount of measurements is large ($1.6 \cdot 10^5$ measurement points of 622 individual current pulses).

[14] $\Delta t = 10\,\mathrm{ps}$ corresponds to $\sim 0.5\,\%$ of the pulse length for the fastest current pulses we observed.
[15] Including the error discussed in section 4.1.

6. Conclusion

The drift velocities of electrons and holes in high-ohmic n-type silicon of <100> crystal orientation were experimentally investigated. Differences of up to 14 % from literature values for <100> orientation and up to 24 % from literature values for <111> orientation are observed. A new parametrization of the charge carrier mobility of electrons and holes is presented that describes the measurements by Canali et al. better than the commonly used parametrization by Caughey and Thomas with the parameters from Jacoboni et al. The mobility parameters of the new parametrization were fitted to our measurements as a function of the electric field and the temperature.

Experimental technique

Transient Current Technique (TCT) measurements were performed using two high resistivity (1.5 kΩcm and 5.5 kΩcm) p^+-n-n^+ silicon pad diodes of <100> crystal orientation from different vendors. Free charge carriers in silicon were generated by fast laser pulses. A red laser ($\lambda = 675\,\text{nm}$) was used to investigate the drift of electrons and holes in electric fields separately, and an infrared laser ($\lambda = 1063\,\text{nm}$) for the simultaneous electron and hole drift. Measurements were performed at seven different temperatures between 233 K and 333 K. Only one sensor was measured at all given temperatures. The investigated range of the mean electric field in the sensor is between 5 kV/cm and 50 kV/cm.

Analysis

Two different methods were used to determine the drift velocity. The simple time-of-flight method was used to determine the apparent velocity of the charge carriers directly from the pulse duration of TCT measurements with the red laser. Additionally, a simulation of charge drift in silicon was compared to the TCT measurements with the red and the infrared laser, and the mobility parameters were fitted by a χ^2 minimization.

Results

A parametrization for the drift of charge carriers in silicon is presented. An inverse linear expression is used for the mobility of electrons

$$\mu_e(E) = \frac{\mu_0^e}{1 + \frac{\mu_0^e}{v_{sat}^e} \cdot E} \tag{6.1}$$

which is the Trofimenkoff parametrization. For the mobility of holes a more complex expression is required

$$\mu_h(E) = \frac{1}{\max[1/\mu_0^h\,,\ 1/\mu_0^h + b \cdot (E - E_0) + c \cdot (E - E_0)^2]} \tag{6.2}$$

which is constant for $E < E_0$ and an inverse second degree polynomial for $E \geq E_0$.

The temperature dependence of the new parameters is modeled as a power law

$$par_i(T) = par_i(T = 300\,\mathrm{K}) \cdot \left(\frac{T\,[\mathrm{K}]}{300\,\mathrm{K}}\right)^{\alpha_i} \tag{6.3}$$

and the parameters at room temperature $par_i(T = 300\,\mathrm{K})$ and the exponents α_i were obtained by a fit to our measurements. The parameter c of the hole mobility is chosen to be independent of T.

The mobility parameters we have determined are listed in Table 5.1. The global error of the drift velocity $v_d^{e,h}(E) = \mu_{e,h}(E) \cdot E$ is estimated to be $\pm 2.5\,\%$. It should be noted that these values are only valid in the electric field and temperature range that was investigated here. The results were obtained for n type silicon but are supposedly valid for high-ohmic p-type silicon as well.

The current transients that were simulated with the parametrization discussed above are consistent with the measured ones. Additionally, the time of flight results are consistent with the results from the fit. The maximum difference between the results of the two methods is $2\,\%$.

Comparison with literature values

In the investigated electric field and temperature range our results are compared to literature values for the <100> direction as well as the literature values by Jacoboni et al. for the <111> direction, since these values are widely used for simulations of <100> silicon devices as well.

The determined electron drift velocity is similar to the values by Canali et al. and Becker et al.; the maximum difference is 6 %. However, our results are always below the Jacoboni <111> values with a maximum difference of 13 %.

The determined hole drift velocity is always higher than the Canali and the Becker values; the maximum difference is about 15 % for both of them. Compared to the Jacoboni <111> values our results are always higher and the maximum difference is 24 %.

Relevance of the results

The charge carrier mobility in silicon is of particular interest for device modeling and simulation. There are many applications using high-ohmic silicon of <100> crystal orientation. For example the CMS tracker uses this material. Our results may help to improve the interpretation of TCT and edge-TCT measurements in order to determine the electric field in irradiated silicon sensors. We have demonstrated that using the <111> mobility values by Jacoboni for simulations of <100> silicon devices may yield an error of up to 24 %. Our results allow for higher precision simulations and a better understanding of the most important semiconductor material: silicon.

A. Appendix

A.1. Laser pulse time spectra

Shown here are the time spectra of the red laser with (fig. A.1) and without (fig. A.2) an afterpulse and of the infrared laser (fig. A.3). The measurements are taken from [6].

A.2. Correlation matrix

Given in Table A.1 is the rescaled correlation matrix assuming $\frac{\chi^2}{n} = 1$ with the number of individual measurement points $n = 1.555 \cdot 10^5$.

A.3. Current pulse shapes

Shown below are the measured and the simulated transient current pulses at different bias voltages at for all temperatures investigated. For the simulation the charge carrier mobility was calculated using the values listed in Table 5.1 and equations 5.8, 5.9, and 5.10. The current pulses for the 200 µm sensor and the 287 µm sensor are shown in Figures A.4-A.13, A.15 and Figures A.14, A.15 respectively.

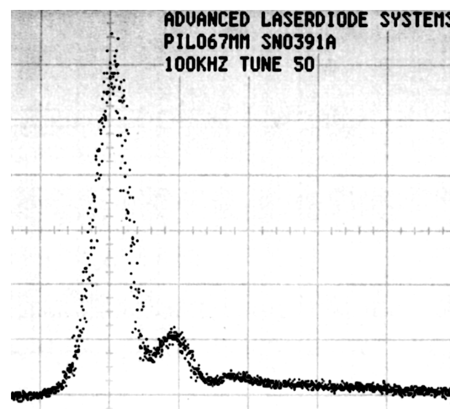

Figure A.1.: Pulse spectrum of the red laser with afterpulse. Measurement with an oscilloscope with 50 ns/div in x and 20 mV/div in y direction.

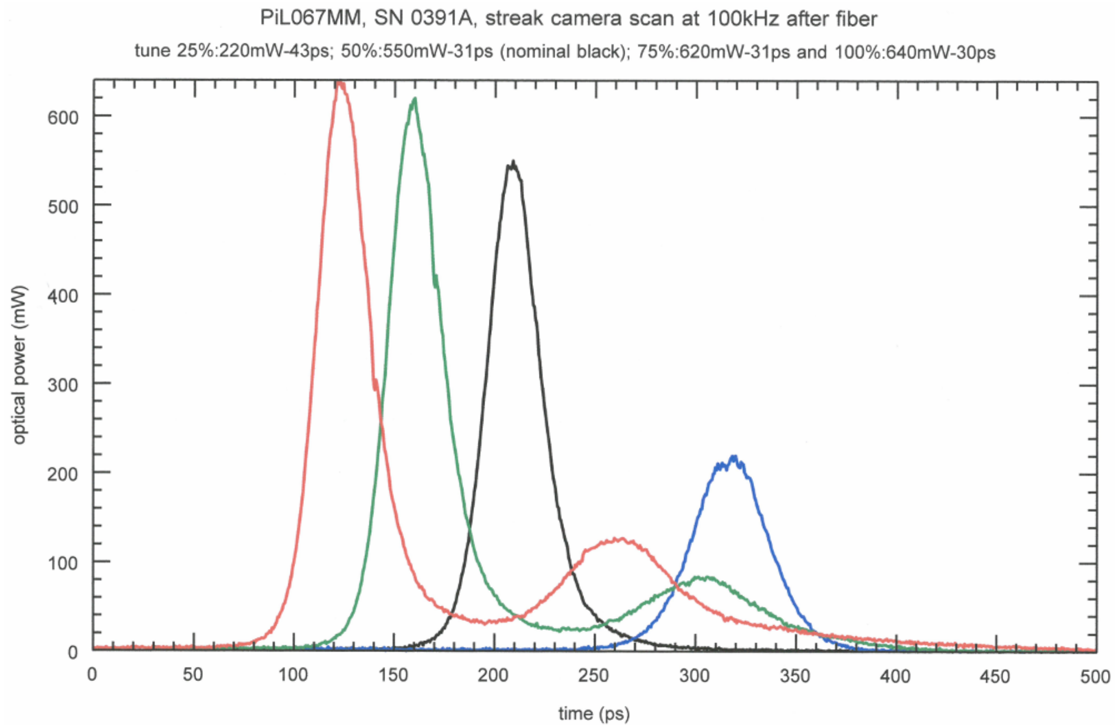

Figure A.2.: Pulse spectrum of the red laser from a streak camera without after-pulse. A tune of 50 % (black line) was used.

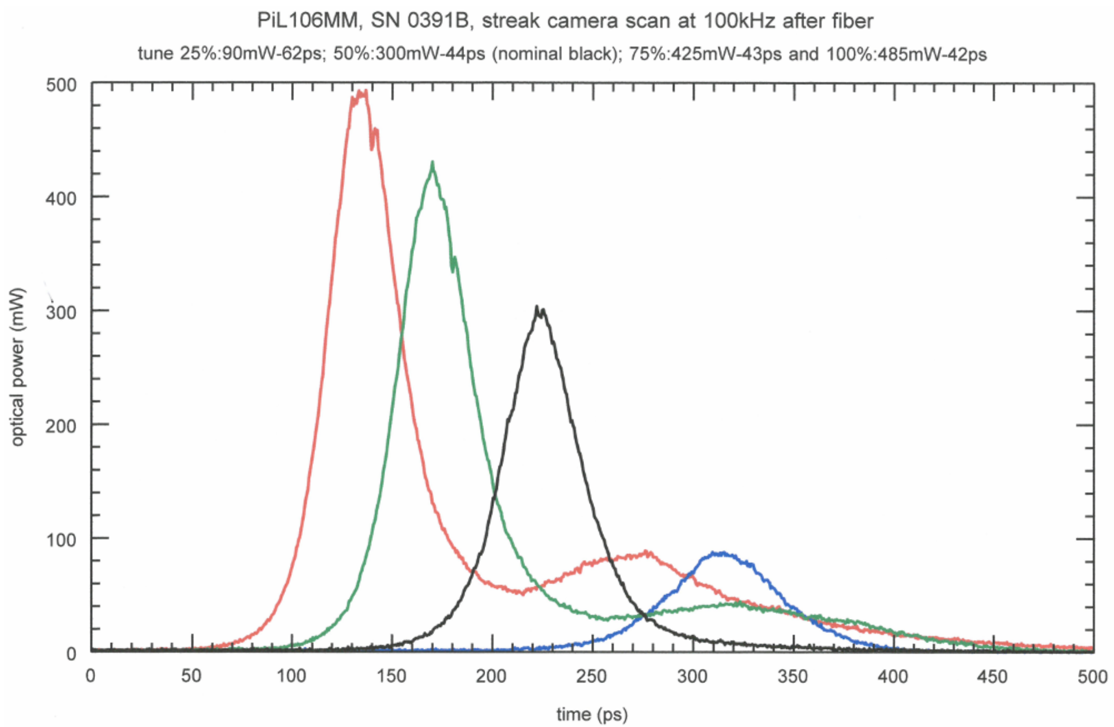

Figure A.3.: Pulse spectrum of the infrared laser from a streak camera. A tune of 50 % (black line) was used.

	$\alpha_{v_s^e}$	v_s^e	$\alpha_{\mu_0^e}$	E_0	b	c	$\alpha_{\mu_0^h}$	α_{E_0}	μ_0^e	μ_0^h	α_b
$\alpha_{v_s^e}$	3.46E-5	1.44E-6	-1.01E-4	2.03E-5	3.61E-6	6.77E-7	2.55E-5	5.78E-4	-5.15E-6	2.38E-6	2.61E-5
v_s^e	1.44E-6	6.63E-8	-4.17E-6	8.42E-7	1.50E-7	2.71E-8	1.06E-6	2.40E-5	-2.16E-7	9.88E-8	1.08E-6
$\alpha_{\mu_0^e}$	-1.01E-4	-4.17E-6	3.00E-4	-5.92E-5	-1.05E-5	-1.97E-6	-7.43E-5	-1.68E-3	1.55E-5	-6.94E-6	-7.59E-5
E_0	2.03E-5	8.42E-7	-5.92E-5	1.33E-5	2.16E-6	2.59E-7	1.54E-5	3.47E-4	-3.03E-6	1.40E-6	1.57E-5
b	3.61E-6	1.50E-7	-1.05E-5	2.16E-6	3.88E-7	8.60E-8	2.71E-6	6.11E-5	-5.37E-7	2.53E-7	2.77E-6
c	6.77E-7	2.71E-8	-1.97E-6	2.59E-7	8.60E-8	6.80E-7	3.42E-7	1.00E-5	-1.01E-7	2.32E-8	2.67E-7
$\alpha_{\mu_0^h}$	2.55E-5	1.06E-6	-7.43E-5	1.54E-5	2.71E-6	3.42E-7	2.12E-5	4.36E-4	-3.80E-6	1.82E-6	2.02E-5
α_{E_0}	5.78E-4	2.40E-5	-1.68E-3	3.47E-4	6.11E-5	1.00E-5	4.36E-4	9.91E-3	-8.61E-5	4.07E-5	4.46E-4
μ_0^e	-5.15E-6	-2.16E-7	1.55E-5	-3.03E-6	-5.37E-7	-1.01E-7	-3.80E-6	-8.61E-5	8.52E-7	-3.55E-7	-3.88E-6
μ_0^h	2.38E-6	9.88E-8	-6.94E-6	1.40E-6	2.53E-7	2.32E-8	1.82E-6	4.07E-5	-3.55E-7	1.78E-7	1.85E-6
α_b	2.61E-5	1.08E-6	-7.59E-5	1.57E-5	2.77E-6	2.67E-7	2.02E-5	4.46E-4	-3.88E-6	1.85E-6	2.06E-5

Table A.1.: Normalized correlation matrix of the global fit. The diagonal elements are the squared errors of the fit parameters. For the exponents α_i (eqn. 5.10) these errors are the absolute errors. For the mobility parameters $par_i(T = 300\,\mathrm{K})$ these errors are approximately the relative errors.

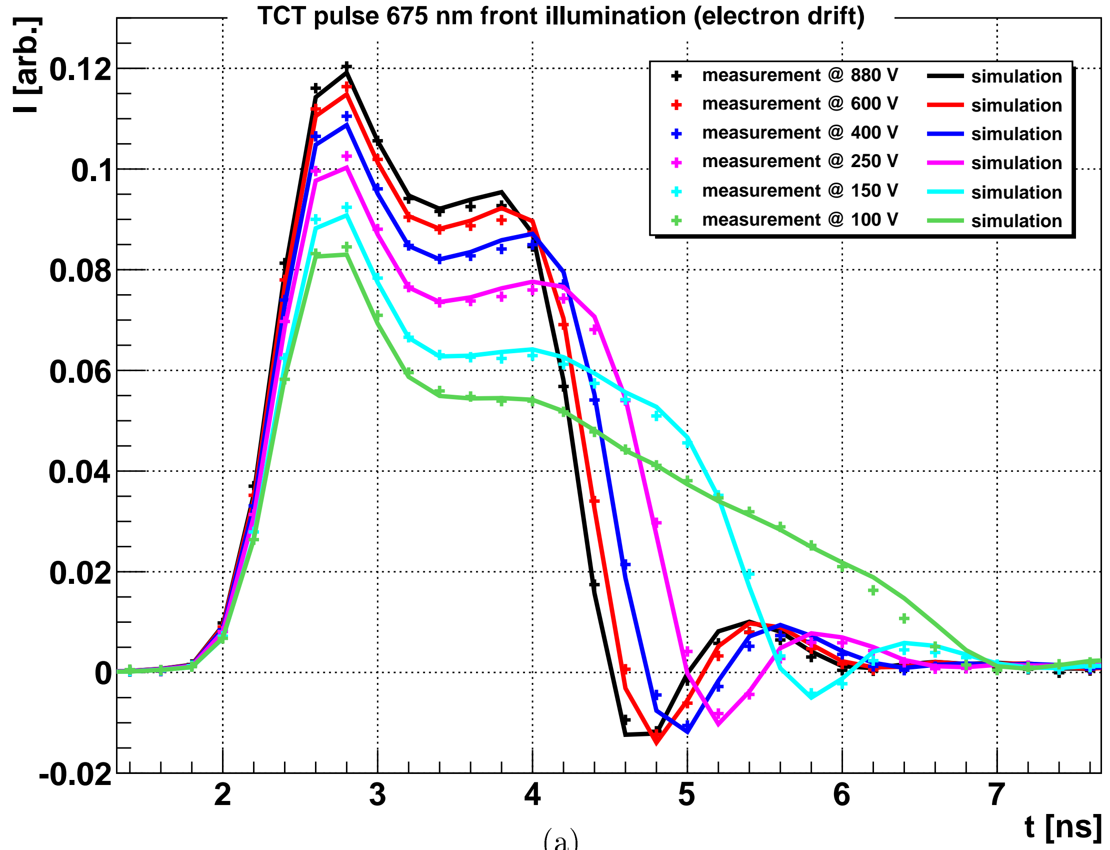

(a)

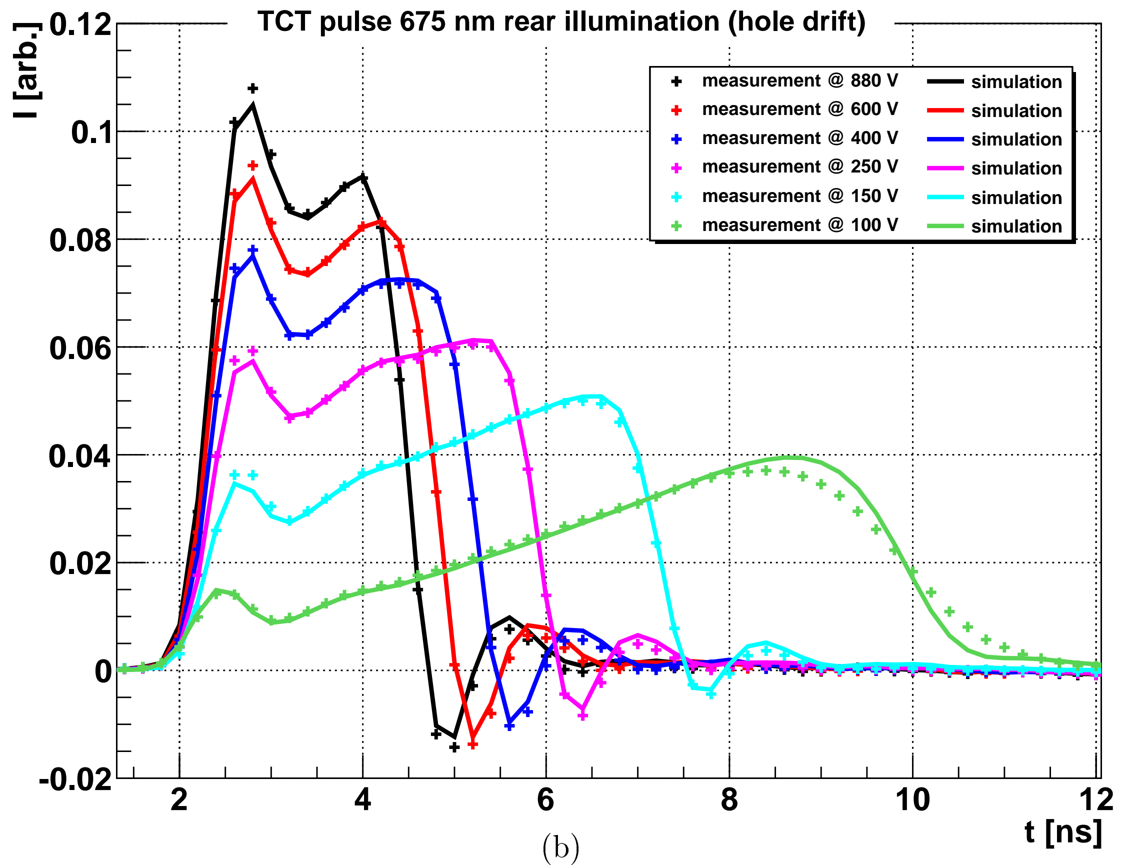

(b)

Figure A.4.: TCT spectra (crosses) and drift simulation (lines) for the 200 µm sensor at 233 K with the parameters obtained from the global fit for electron drift (a) and hole drift (b).

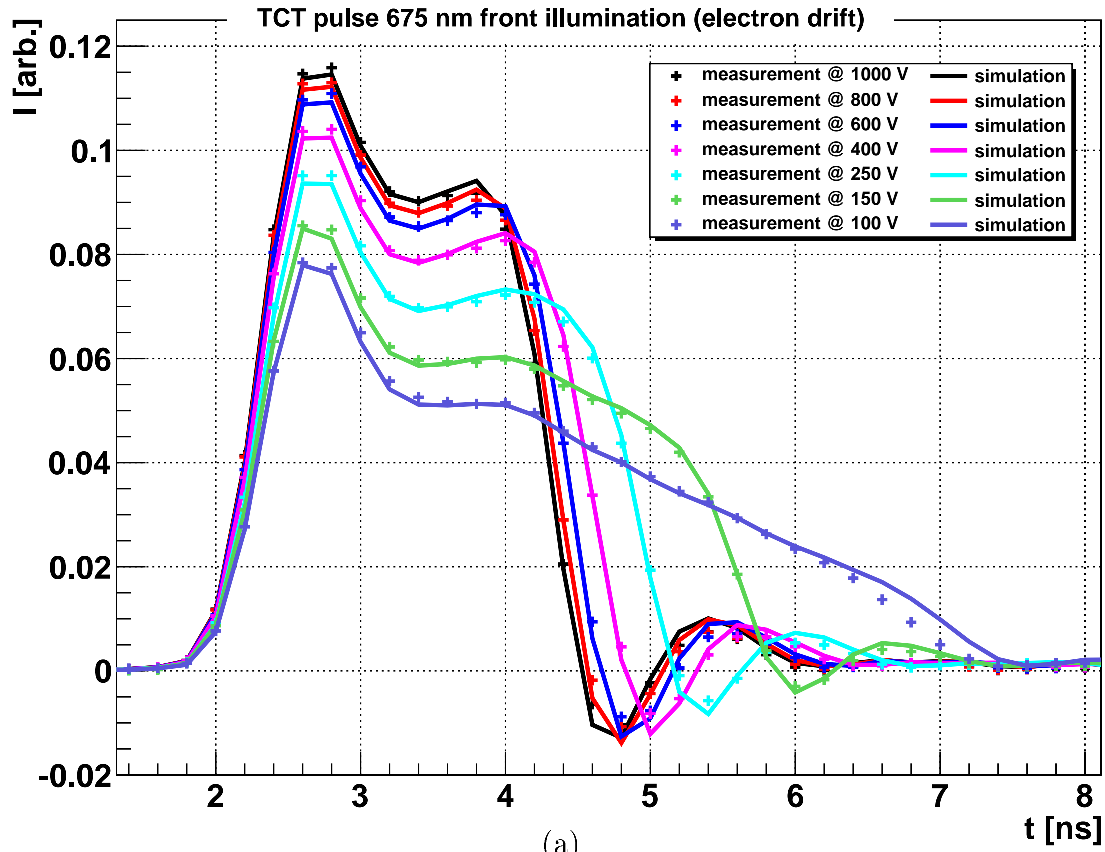

(a)

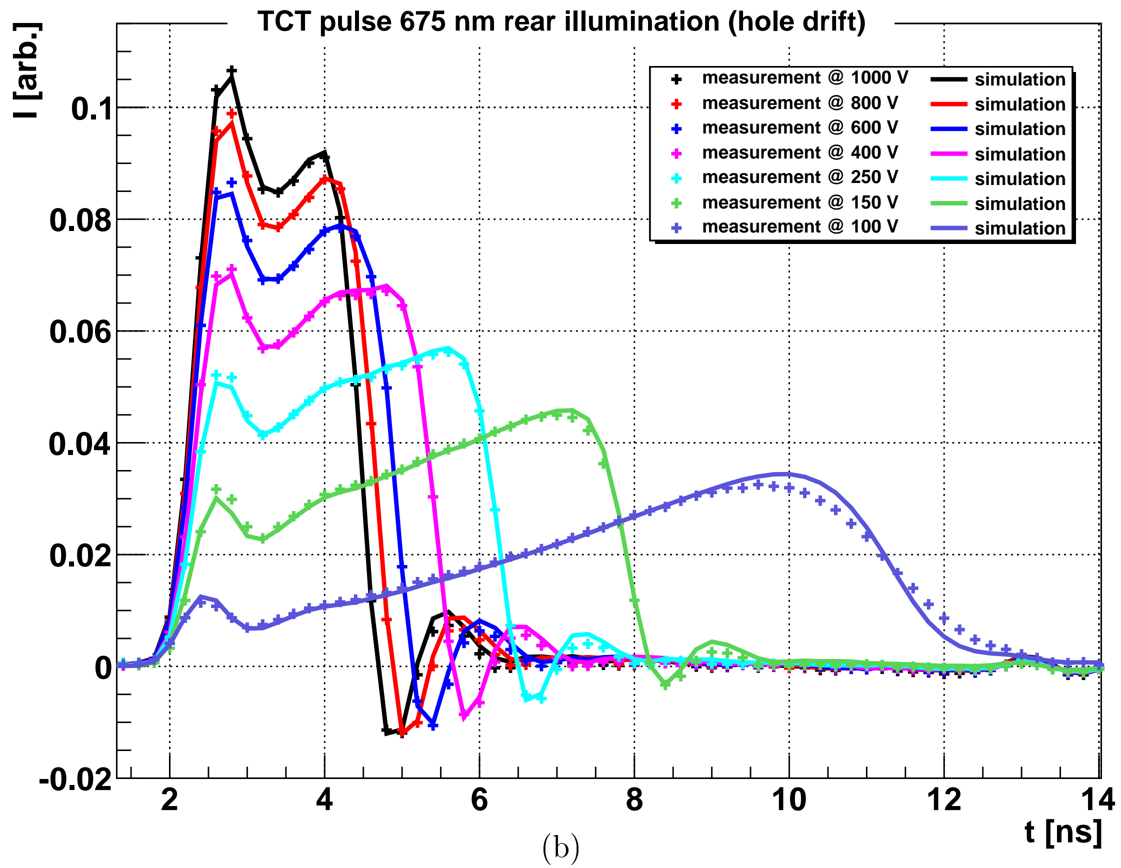

(b)

Figure A.5.: TCT spectra (crosses) and drift simulation (lines) for the 200 µm sensor at 253 K with the parameters obtained from the global fit for electron drift (a) and hole drift (b).

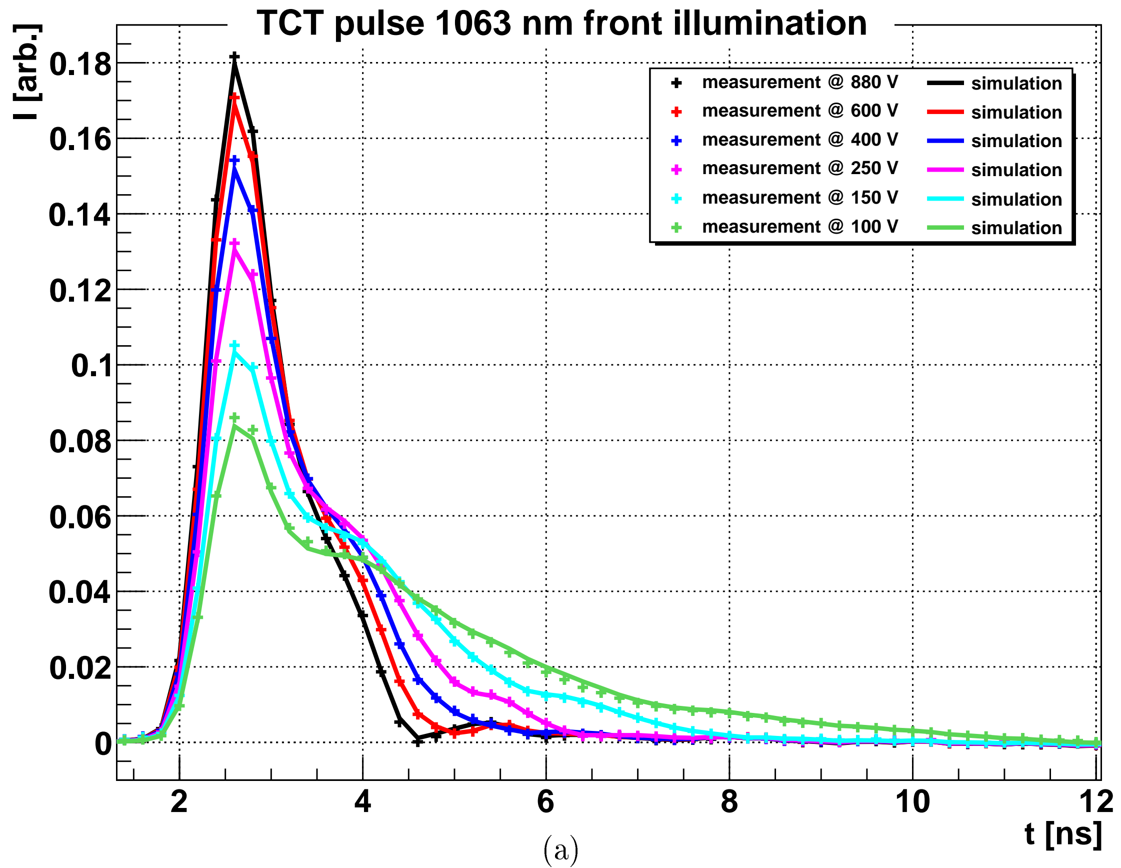

(a)

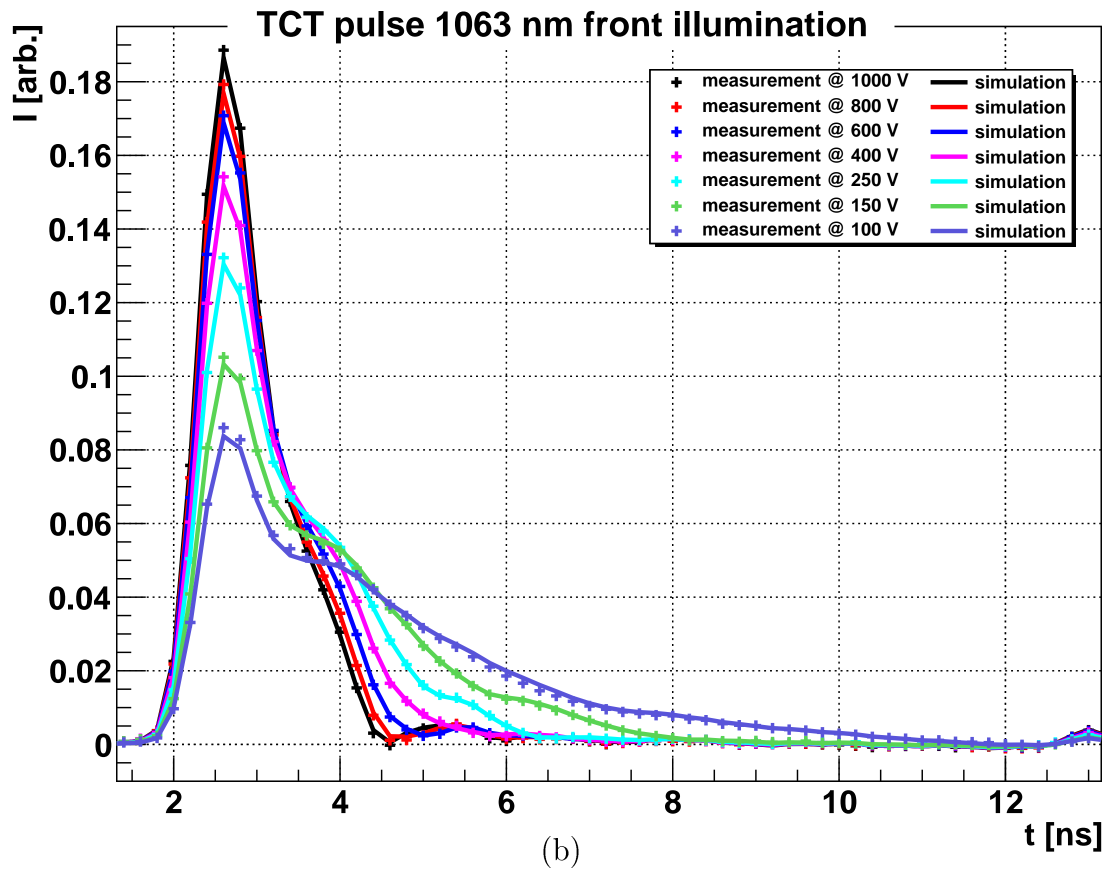

(b)

Figure A.6.: TCT spectra (crosses) and drift simulation (lines) for the 200 µm sensor with the parameters obtained from the global fit for illumination with the infrared laser at 233 K (a) and at 253 K (b).

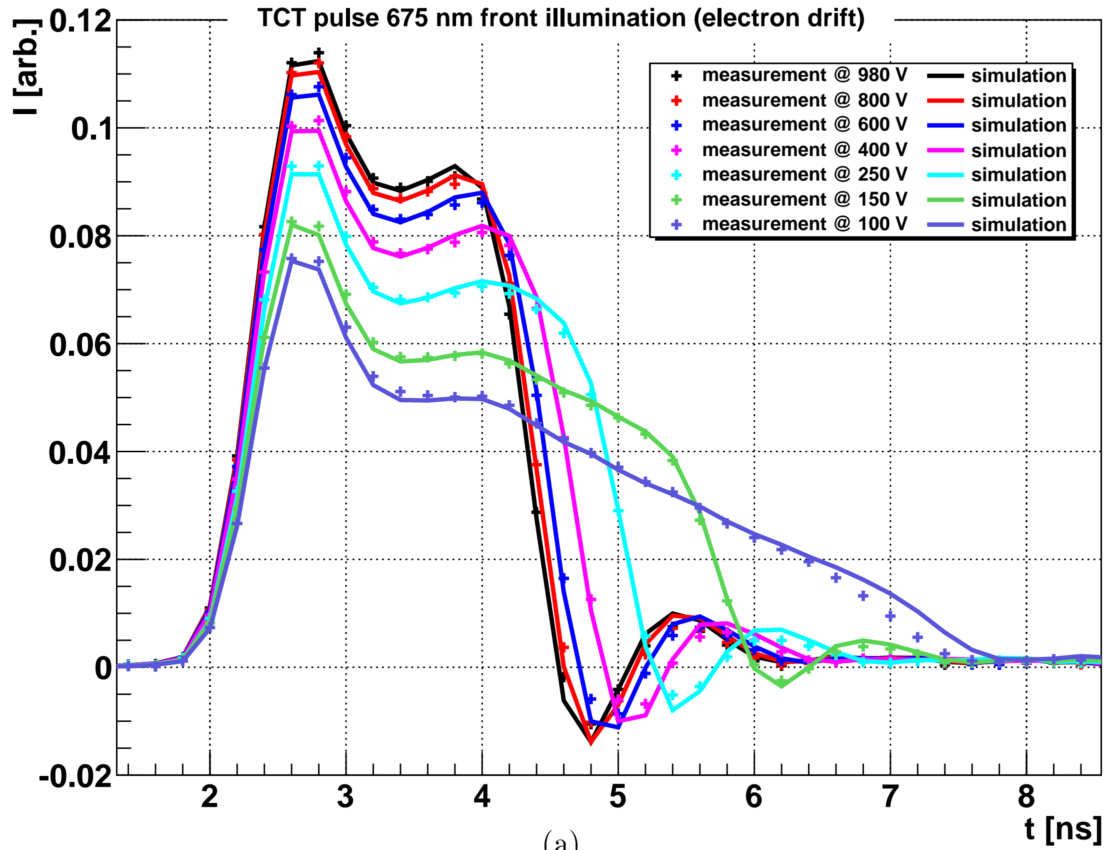

(a)

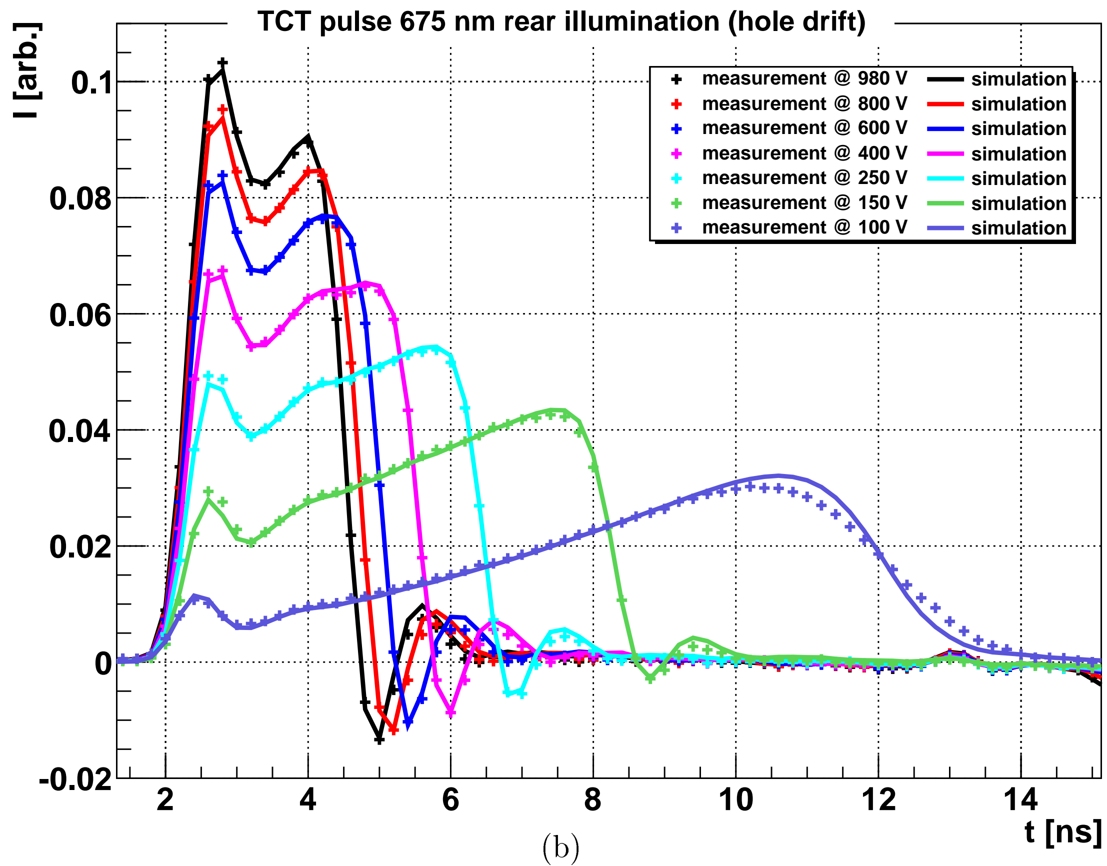

(b)

Figure A.7.: TCT spectra (crosses) and drift simulation (lines) for the 200 µm sensor at 263 K with the parameters obtained from the global fit for electron drift (a) and hole drift (b).

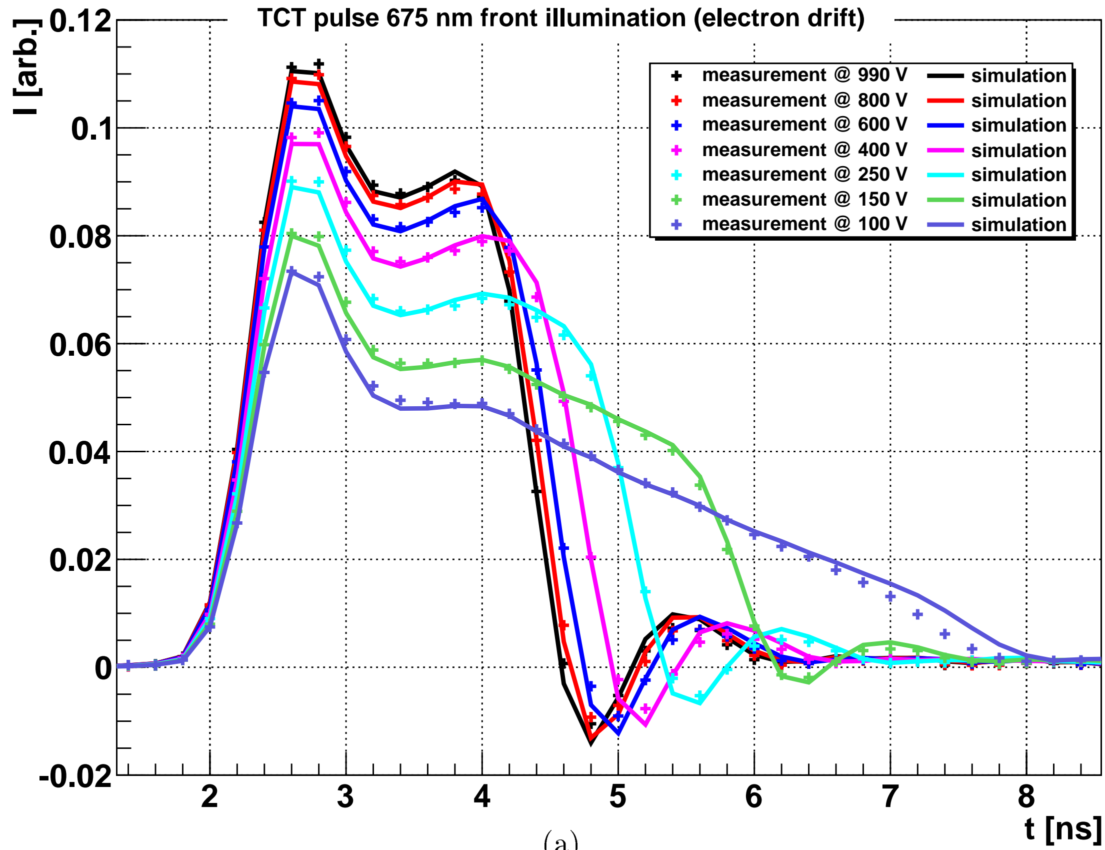

(a)

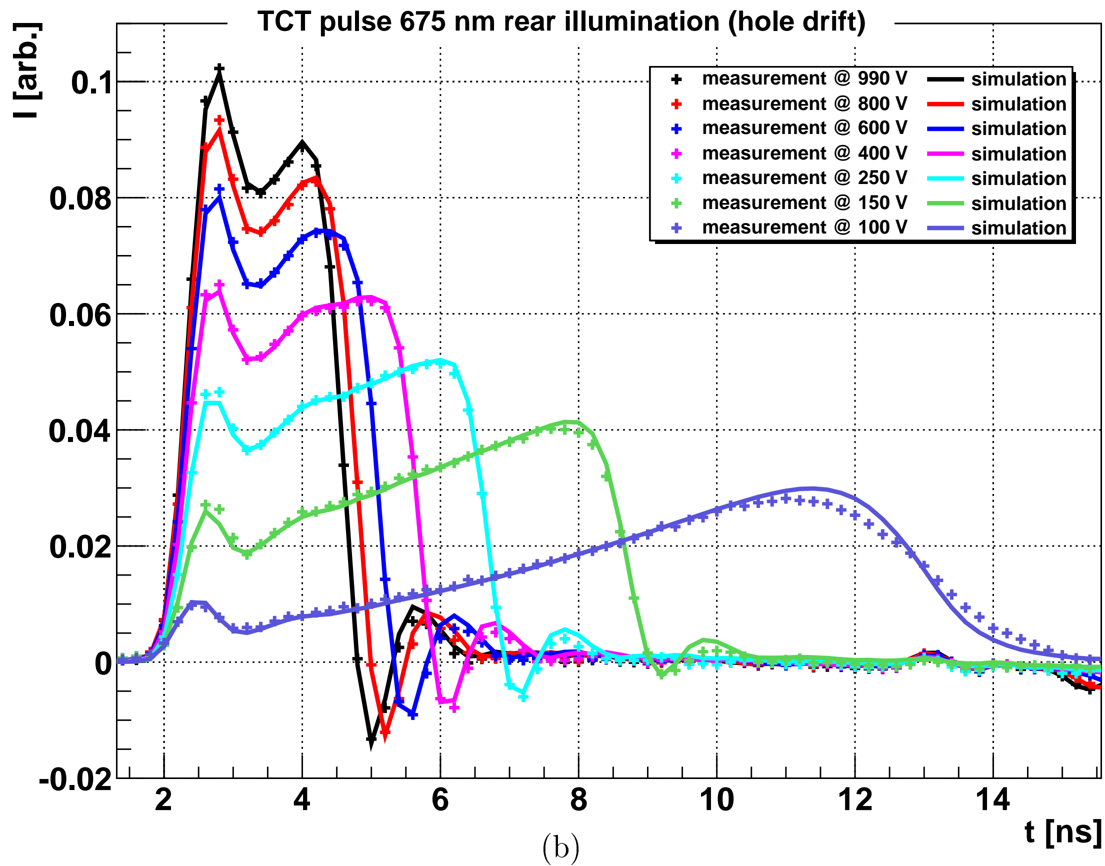

(b)

Figure A.8.: TCT spectra (crosses) and drift simulation (lines) for the 200 µm sensor at 273 K with the parameters obtained from the global fit for electron drift (a) and hole drift (b).

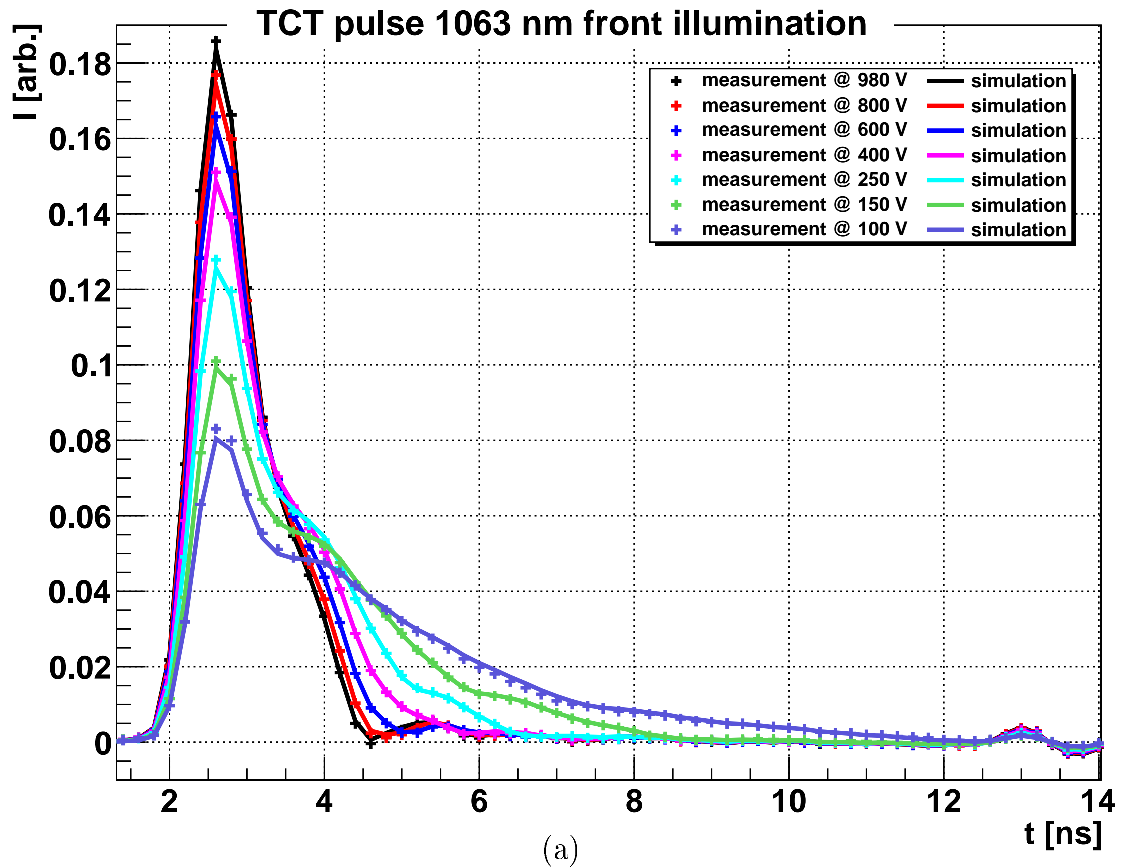

(a)

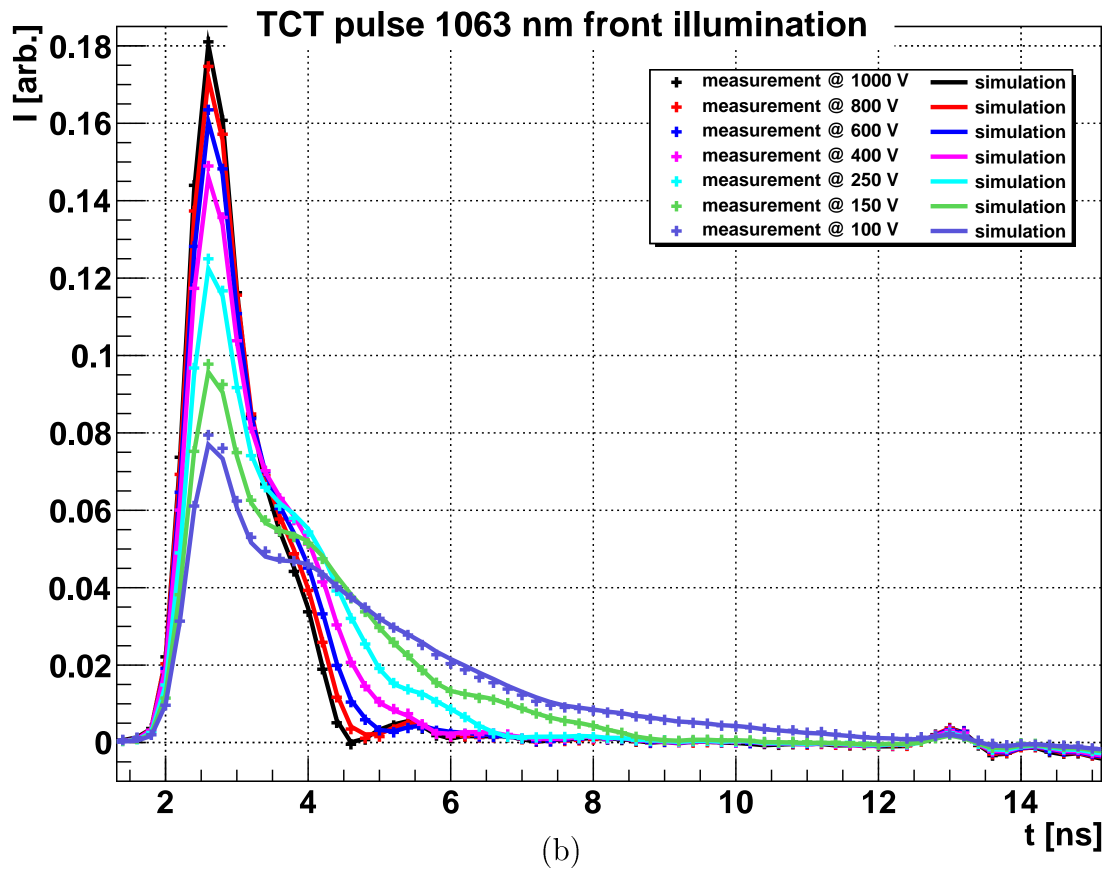

(b)

Figure A.9.: TCT spectra (crosses) and drift simulation (lines) for the 200 µm sensor with the parameters obtained from the global fit for illumination with the infrared laser at 263 K (a) and at 273 K (b).

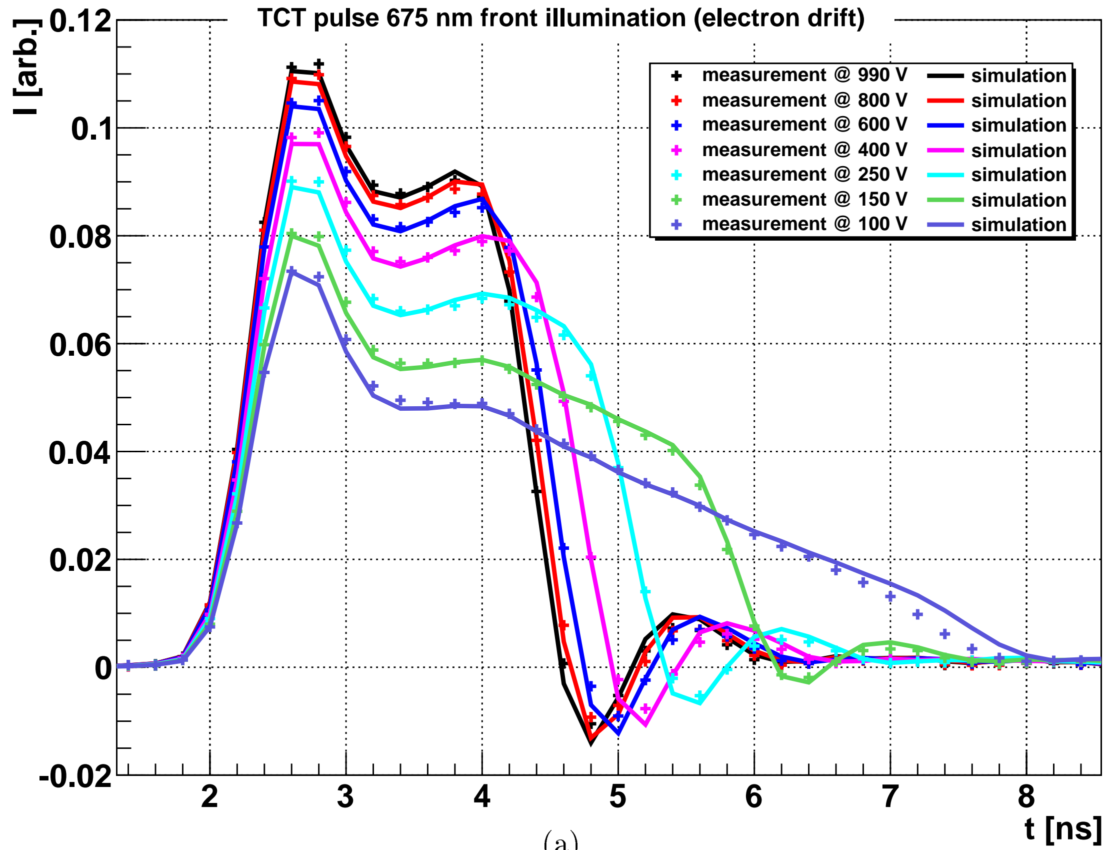

(a)

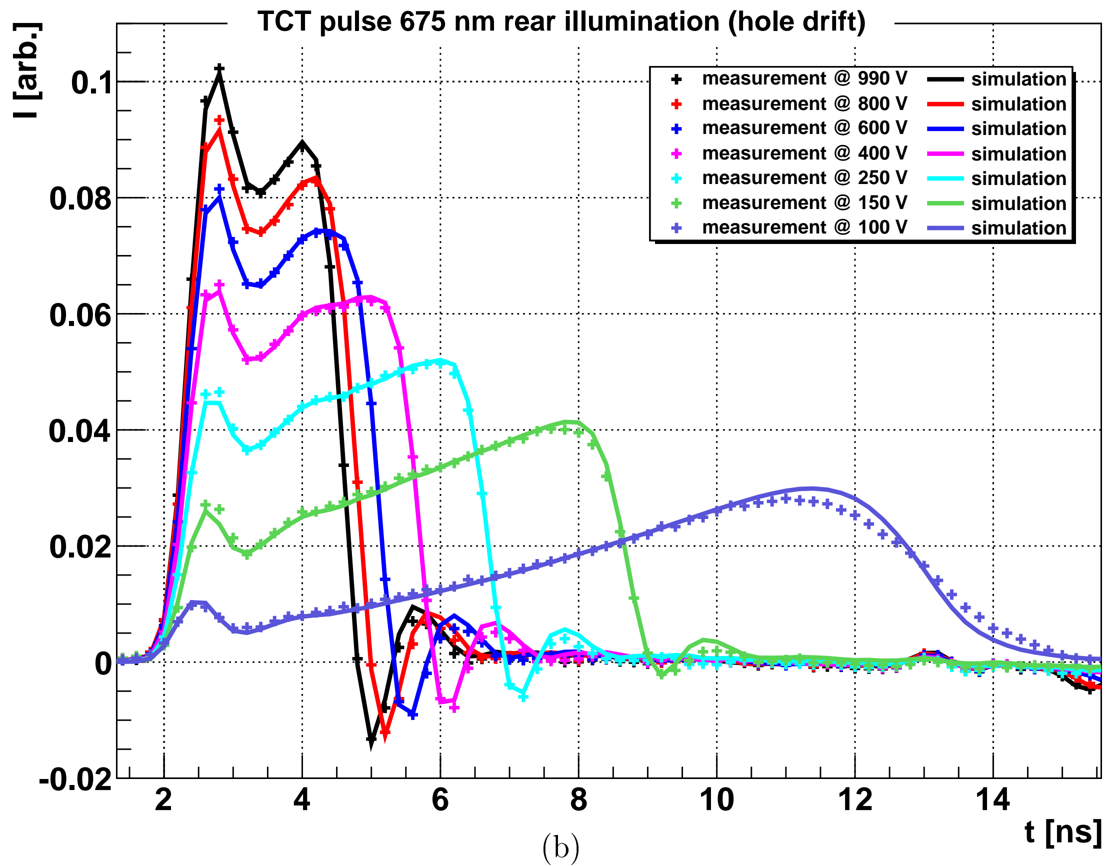

(b)

Figure A.10.: TCT spectra (crosses) and drift simulation (lines) for the 200 µm sensor at 293 K with the parameters obtained from the global fit for electron drift (a) and hole drift (b).

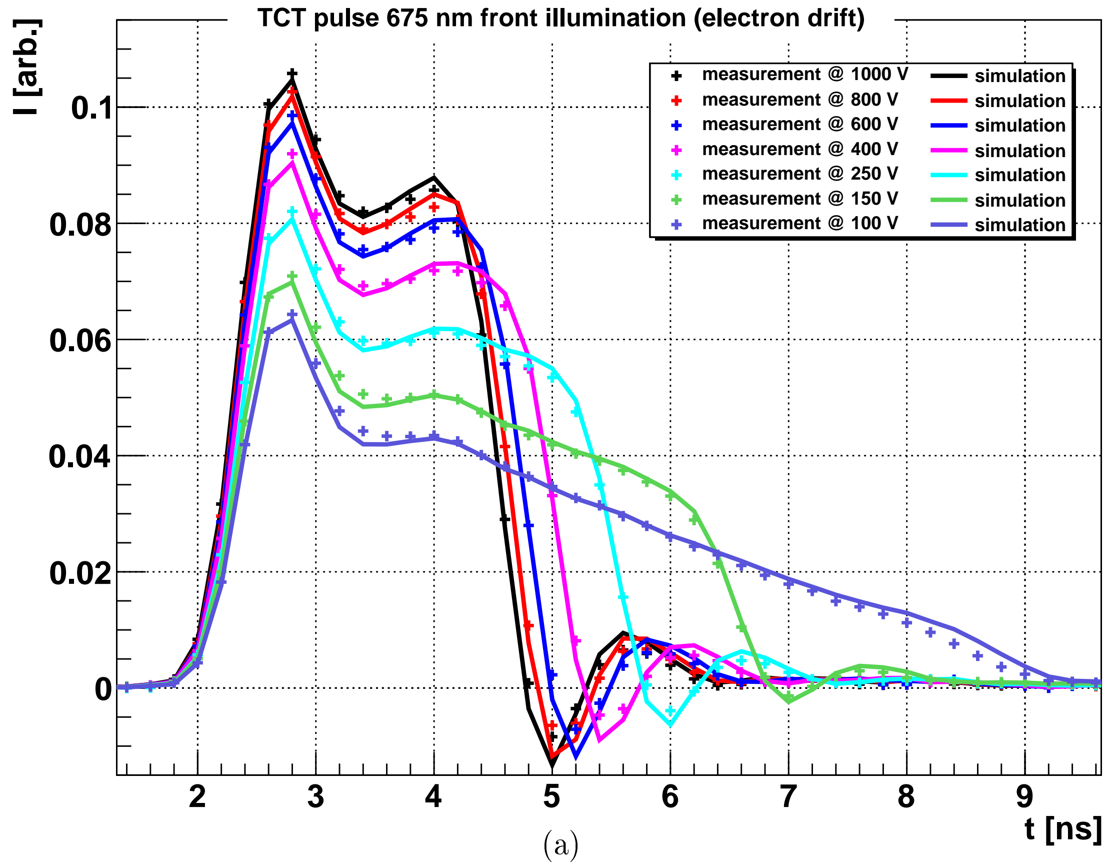

(a)

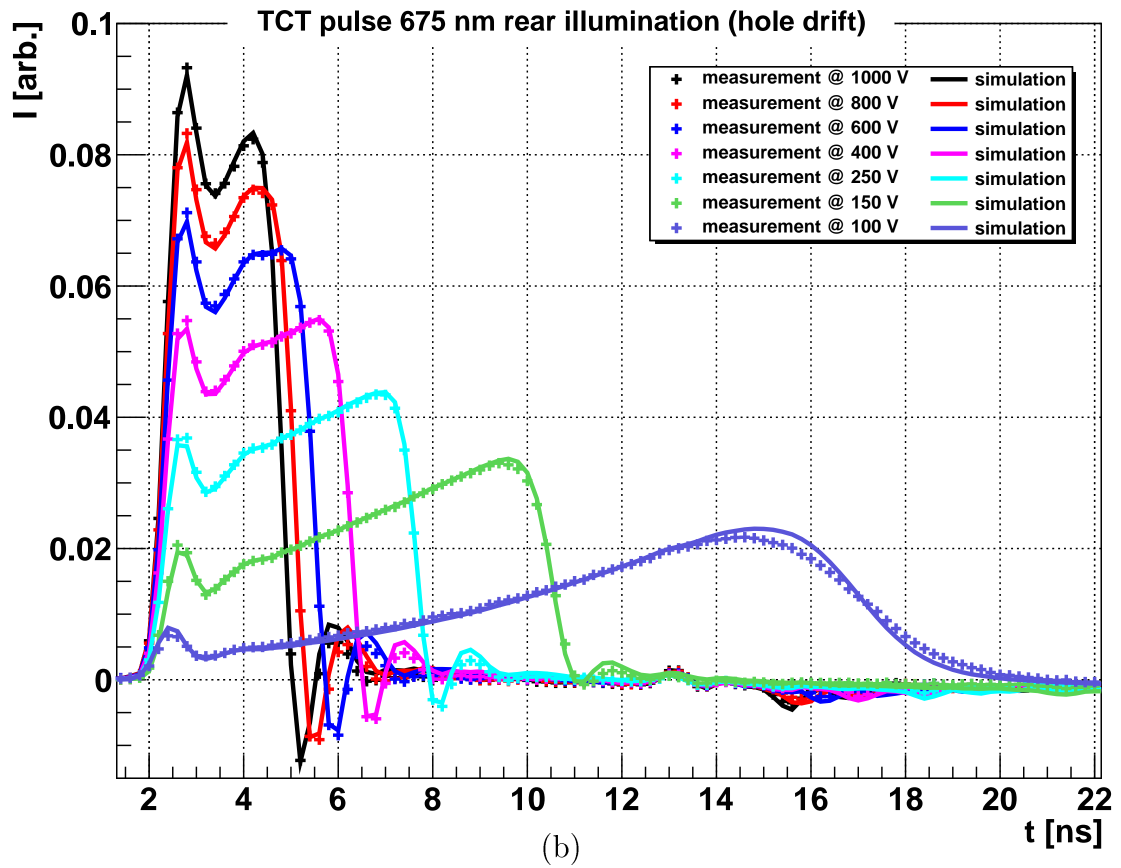

(b)

Figure A.11.: TCT spectra (crosses) and drift simulation (lines) for the 200 µm sensor at 313 K with the parameters obtained from the global fit for electron drift (a) and hole drift (b).

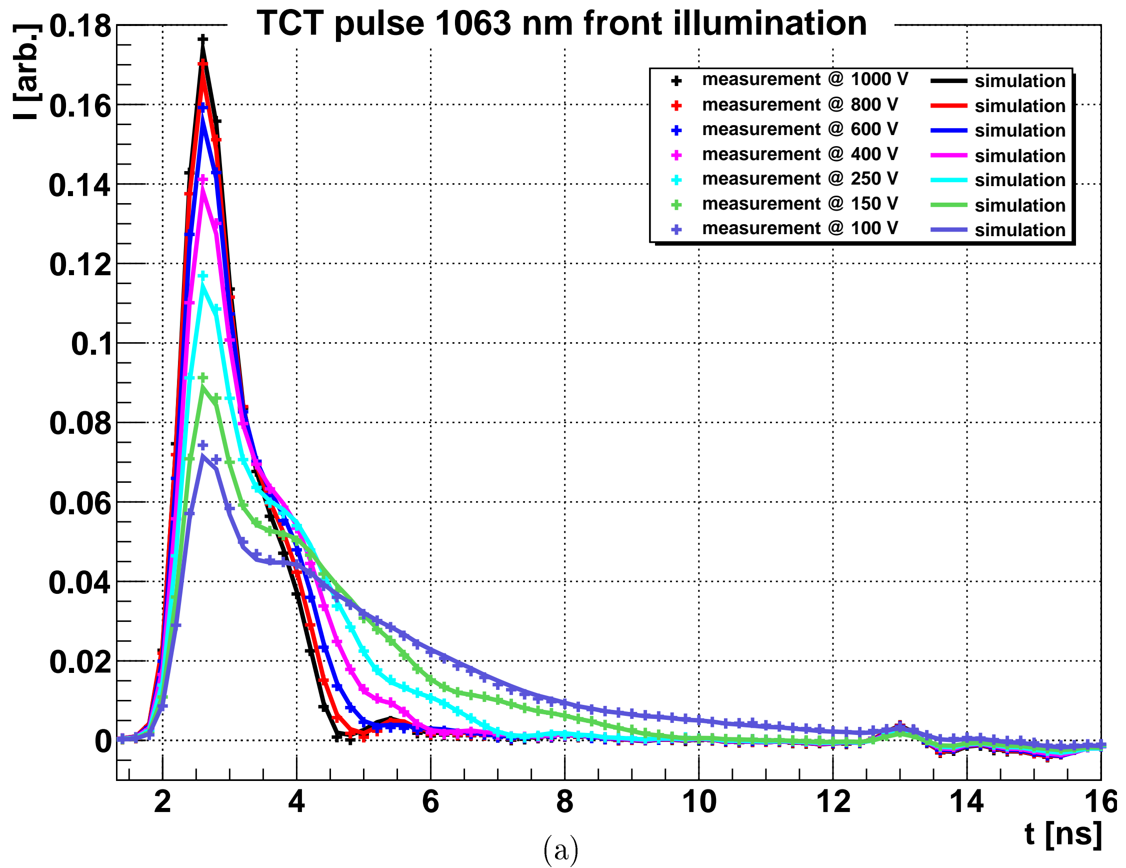

(a)

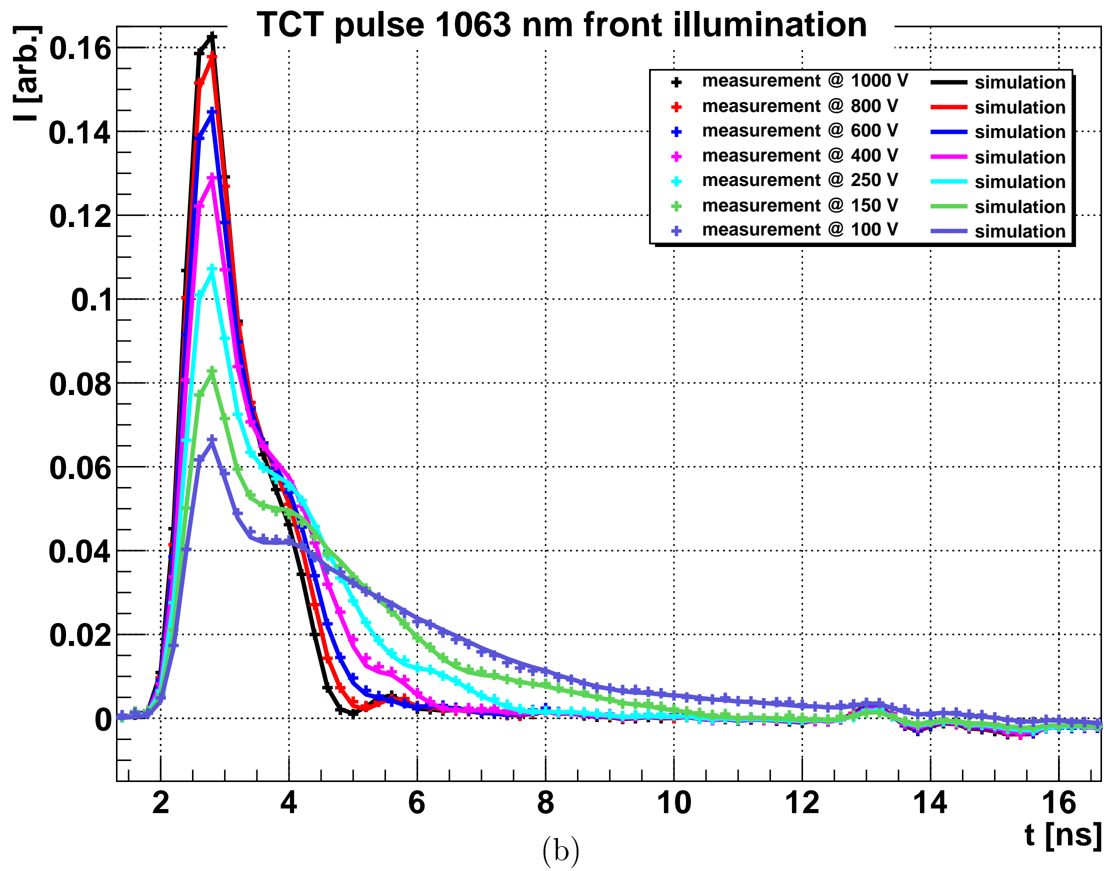

(b)

Figure A.12.: TCT spectra (crosses) and drift simulation (lines) for the 200 µm sensor with the parameters obtained from the global fit for illumination with the infrared laser at 293 K (a) and at 313 K (b).

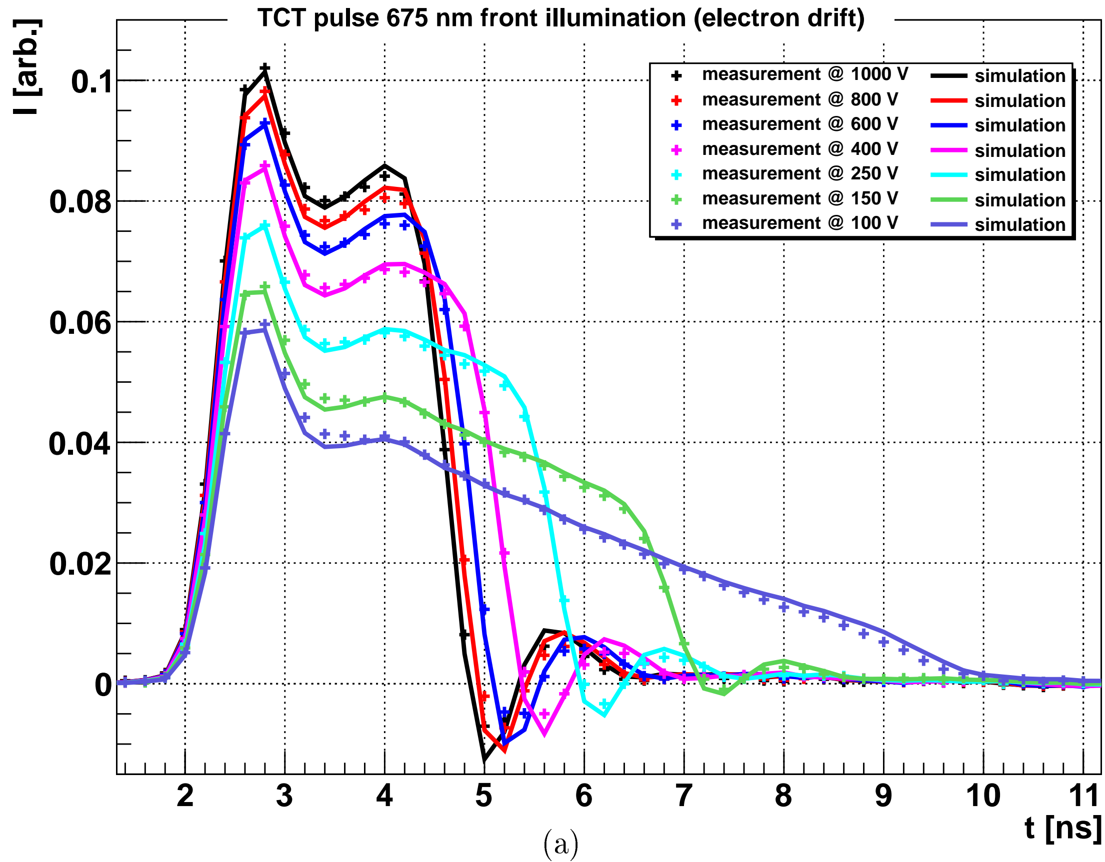

(a)

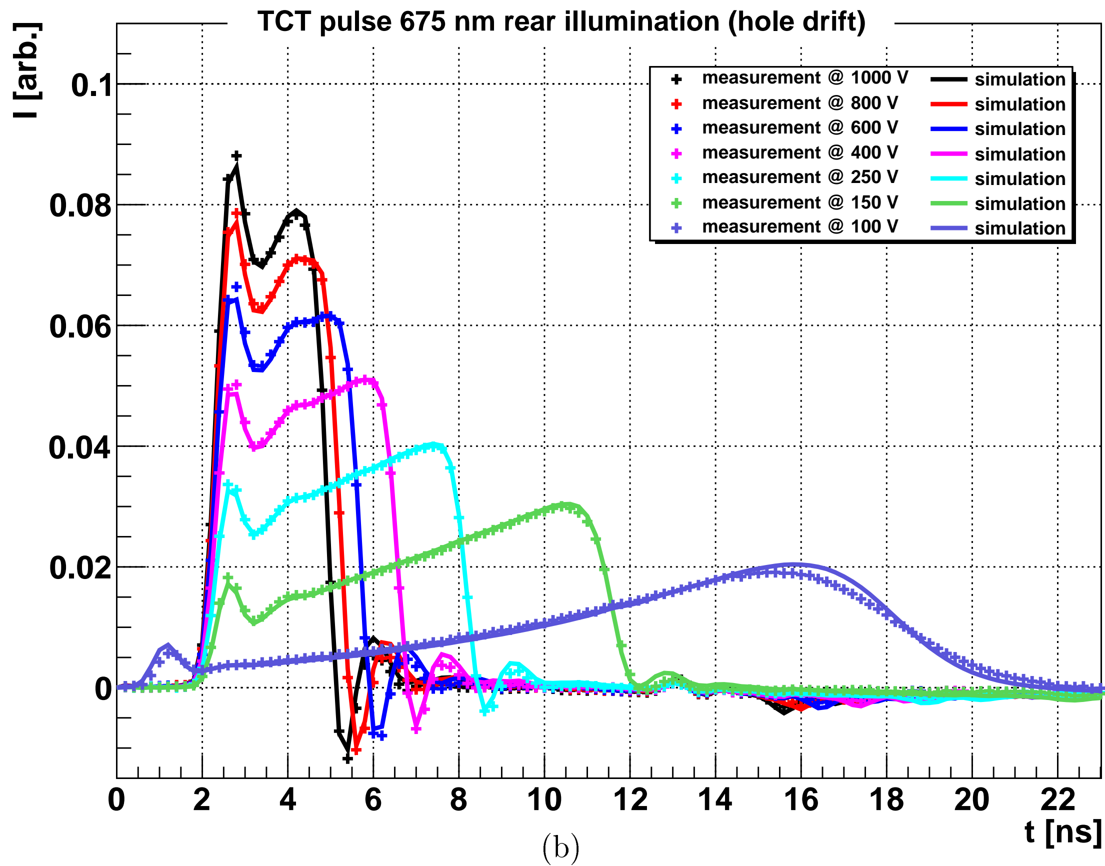

(b)

Figure A.13.: TCT spectra (crosses) and drift simulation (lines) for the 200 µm sensor at 333 K with the parameters obtained from the global fit for electron drift (a) and hole drift (b).

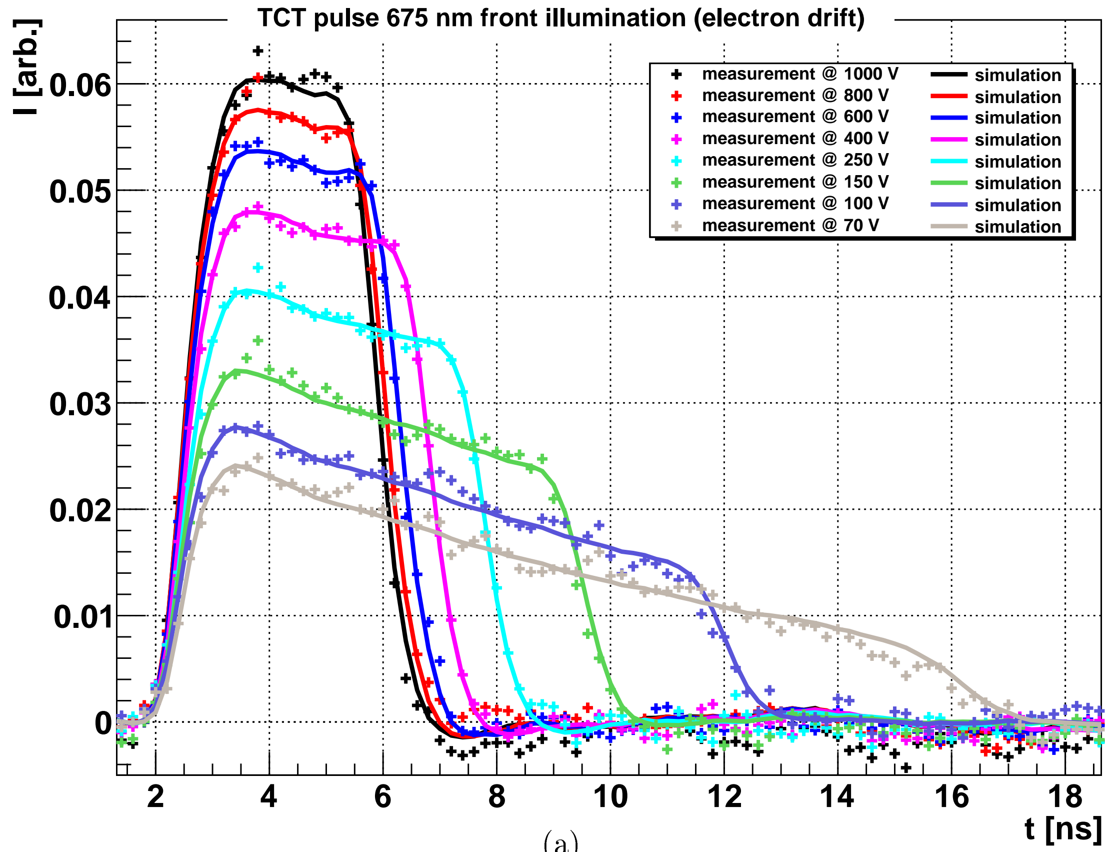

(a)

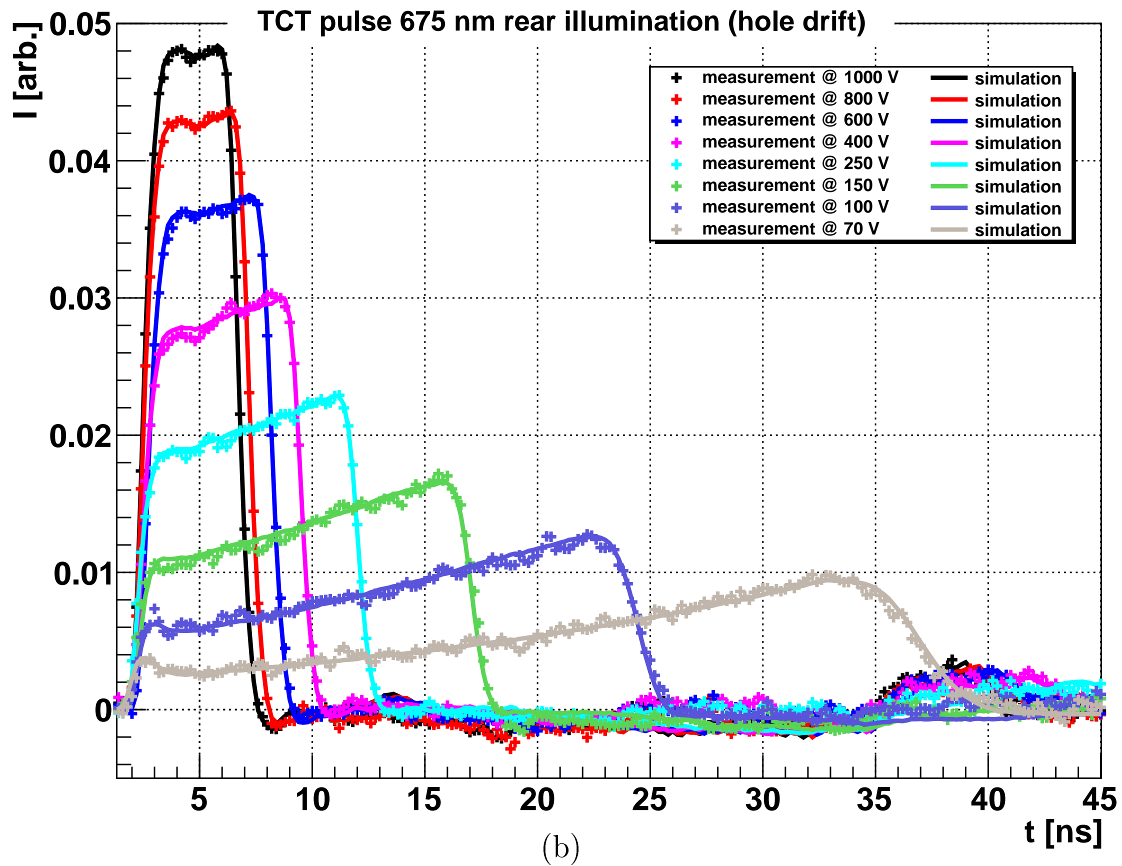

(b)

Figure A.14.: TCT spectra (crosses) and drift simulation (lines) for the 287 µm sensor at 313 K with the parameters obtained from the global fit for electron drift (a) and hole drift (b).

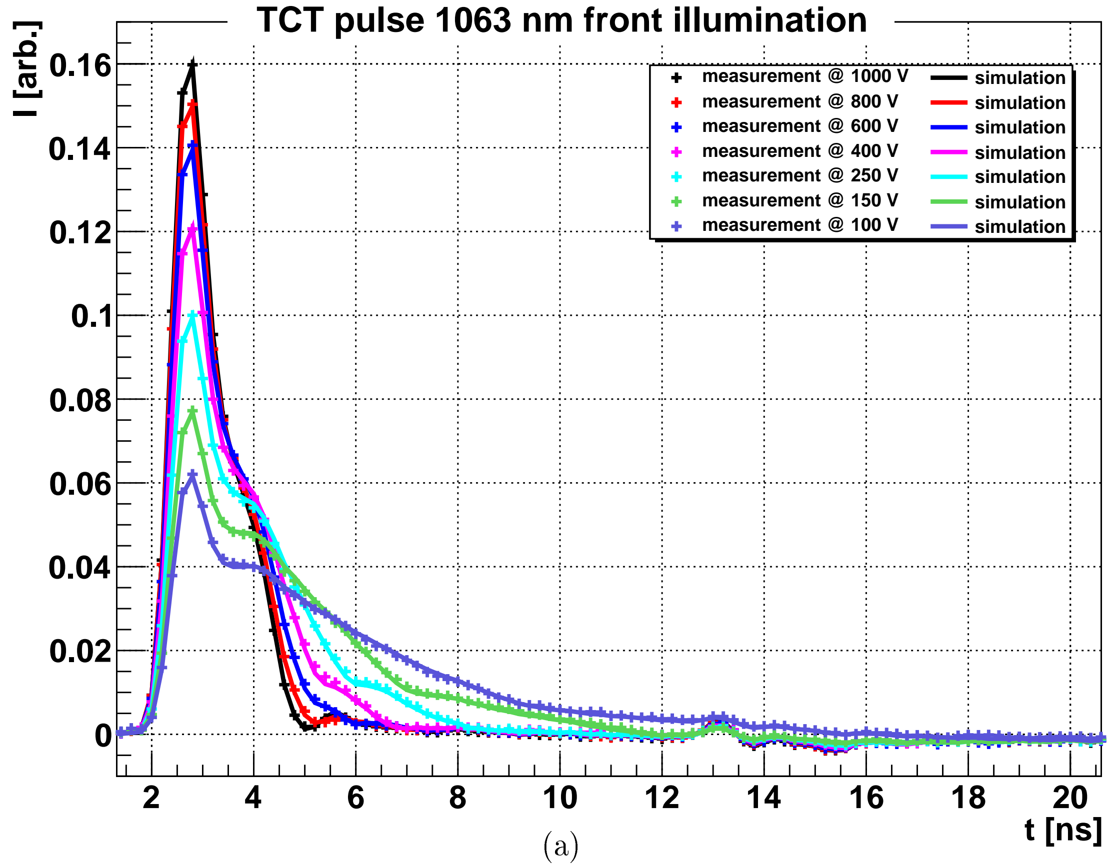

(a)

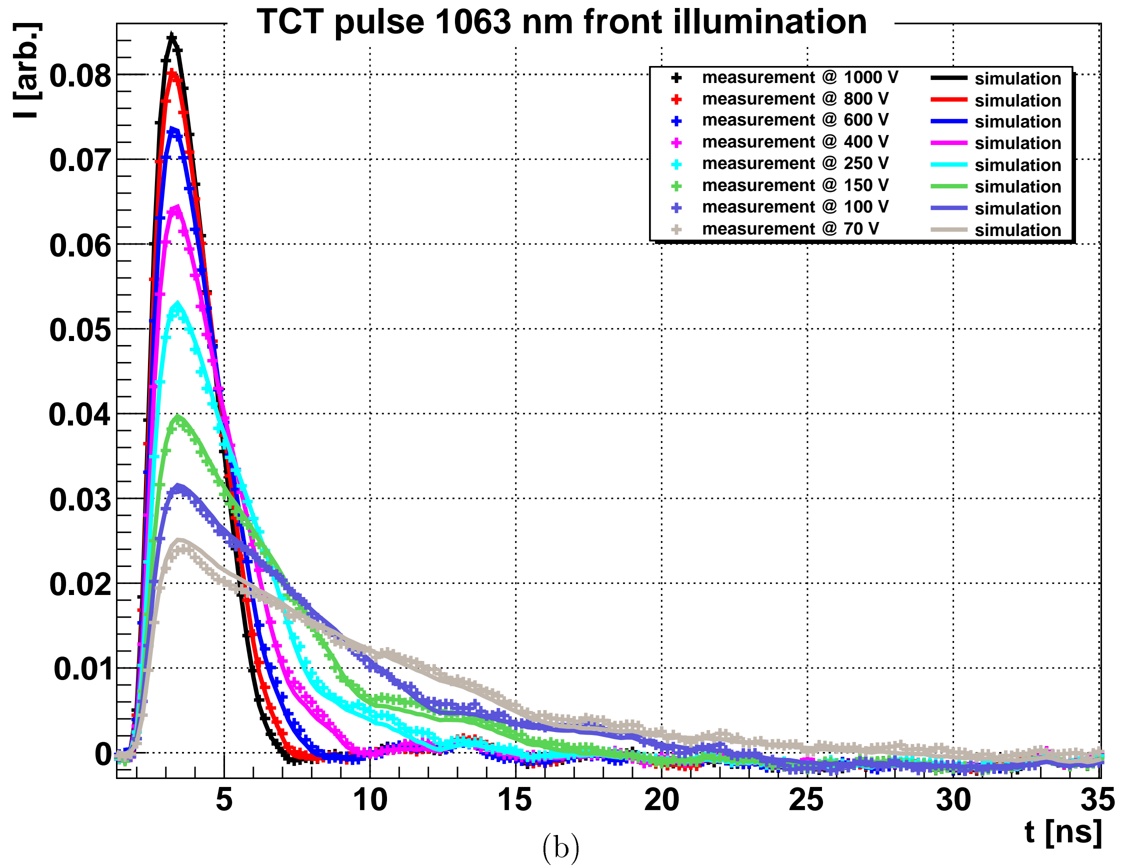

(b)

Figure A.15.: TCT spectra (crosses) and drift simulation (lines) with the parameters obtained from the global fit for illumination with the infrared laser at 333 K for the 200 μm sensor (a) and at 313 K for the 287 μm sensor (b).

List of Figures

2.1. An asymmetric p-n junction in thermal equilibrium. 3

3.1. Schematic cross section of a silicon diode. 6
3.2. Simplified illustration of the TCT setup. 8
3.3. Schematic of the initial distribution of electron-hole pairs and subsequent charge carrier drift in an electric field $\vec{E}$ for front illumination with the red and the infrared laser. 9
3.4. Simulation of a transient current pulse. 10

4.1. Determination of t_{tof} for electron drift in the 200 µm sensor at $U_{bias} = 200\,\mathrm{V}$ and $T = 313\,\mathrm{K}$. 12
4.2. Schematic of one time step of the drift simulation. 14
4.3. Electric field from a TCAD simulation for a diode with a total thickness of 203 µm. 15
4.4. Determination of the response function. 18
4.5. Fourier transforms of the measurement and the simulation. 19
4.6. Example for the performance of the convolution method. 20

5.1. TCT measurements are compared to the simulations using the Jacoboni [17] parameters for <111> crystal orientation. 23
5.2. Experimental values and the parametrization for <111> crystal orientation for electrons and for holes from [17]. 24
5.3. Inverse mobility for electrons and holes by Canali [10] at $T = 300\,\mathrm{K}$ for the <100> crystal orientation. 26
5.4. TCT spectra for hole drift compared with the simulation for the linear and the quadratic mobility parametrization at $T = 233\,\mathrm{K}$. . . 27
5.5. Inverse mobility of electrons and holes at $T = 313\,\mathrm{K}$ from the fit and the tof method for the 200 µm sensor and the 287 µm sensor. . 28
5.6. Difference between the drift velocity of each sensor for the best fitting parameters at $T = 313\,\mathrm{K}$. 28
5.7. TCT spectra and the drift simulation with the results at $T = 313\,\mathrm{K}$ for front illumination with the red laser for the 200 µm sensor and the 287 µm sensor. 32

5.8. TCT spectra and the drift simulation with the results at $T = 313\,\mathrm{K}$ for rear illumination with the red laser for the 200 µm sensor and the 287 µm sensor. 33
5.9. TCT spectra and the drift simulation with the results at $T = 313\,\mathrm{K}$ for illumination with the infrared laser for the 200 µm sensor and the 287 µm sensor. 34
5.10. The drift velocity from the global T fit is compared to the results of the single T fits as well as the time of flight results. 37
5.11. Differences of v_d^{global} and both the Jacoboni values for the <111> orientation and the tof values by Canali for the <100> orientation at $T = 245\,\mathrm{K}$ and $T = 300\,\mathrm{K}$. 38
5.12. Differences of v_d^{global} and both the drift velocity for the Becker parameters and the Canali tof values at $T = 245\,\mathrm{K}$ and $T = 300\,\mathrm{K}$. . . 40
5.13. Average baseline recorded for the 287 µm sensor and the current pulse for hole drift without baseline correction. 43

A.1. Pulse spectrum of the red laser with afterpulse. Measurement with an oscilloscope. 50
A.2. Pulse spectrum of the red laser from a streak camera without afterpulse. 51
A.3. Pulse spectrum of the infrared laser from a streak camera. 51
A.4. TCT spectra (red laser) for the 200 µm sensor at 233 K. 53
A.5. TCT spectra (red laser) for the 200 µm sensor at 253 K. 54
A.6. TCT spectra (infrared laser) for the 200 µm sensor at 233 K and 253 K. 55
A.7. TCT spectra (red laser) for the 200 µm sensor at 263 K. 56
A.8. TCT spectra (red laser) for the 200 µm sensor at 273 K. 57
A.9. TCT spectra (infrared laser) for the 200 µm sensor at 263 K and 273 K. 58
A.10. TCT spectra (red laser) for the 200 µm sensor at 293 K. 59
A.11. TCT spectra (red laser) for the 200 µm sensor at 313 K. 60
A.12. TCT spectra (infrared laser) for the 200 µm sensor at 293 K and 313 K. 61
A.13. TCT spectra (red laser) for the 200 µm sensor at 333 K. 62
A.14. TCT spectra (red laser) for the 287 µm sensor at 313 K. 63
A.15. TCT spectra (infrared laser) at 333 K for the 200 µm sensor and at 313 K for the 287 µm sensor. 64

List of Tables

3.1. Physical properties of the test structures we investigated. 7

4.1. Parameters for the attenuation coefficient $\alpha_s(T) = a_1 + b_2 \cdot T$ at different λ. 14

5.1. The mobility parameters of eqn. 5.8, eqn. 5.9, and eqn. 5.10 for silicon of <100> orientation determined for electric field values ranging from $E = 5\,\mathrm{kV/cm}$ to $E = 50\,\mathrm{kV/cm}$ at temperatures between $T = 233\,\mathrm{K}$ and $T = 333\,\mathrm{K}$. 36

A.1. Normalized correlation matrix of the global fit. The diagonal elements are the squared errors of the fit parameters. 52

Bibliography

[1] CiS Forschungsinstitut für Mikrosensorik und Photovoltaik GmbH. http://www.cismst.org/.

[2] Hamamatsu Photonics K.K. http://www.hamamatsu.com/.

[3] ROOT - A Data Analysis Framework. http://root.cern.ch/drupal/.

[4] SPICE (Simulation Program with Integrated Circuit Emphasis). http://www.ngspice.com/.

[5] The CMS Collaboration. http://cms.web.cern.ch/.

[6] Advanced Laser Diode Systems A.L.S. GmbH. Picosecond Injection Laser (PiLas) Owner's Manual. http://alsgmbh.de/.

[7] J Becker. *Signal development in silicon sensors used for radiation detection.* PhD thesis, University of Hamburg, 2010. DESY-thesis-2010-33.

[8] J Becker, E Fretwurst, and R Klanner. Measurements of charge carrier mobilities and drift velocity saturation in bulk silicon of< 111> and< 100> crystal orientation at high electric fields. *Solid-State Electronics*, 56(1):104–110, 2011.

[9] C Canali, G Majni, R Minder, and G Ottaviani. Electron and hole drift velocity measurements in silicon and their empirical relation to electric field and temperature. *Electron Devices, IEEE Transactions on*, 22(11):1045–1047, 1975.

[10] C Canali, G Ottaviani, and A Alberigi Quaranta. Drift velocity of electrons and holes and associated anisotropic effects in silicon. *Journal of Physics and Chemistry of Solids*, 32(8):1707–1720, 1971.

[11] DM Caughey and RE Thomas. Carrier mobilities in silicon empirically related to doping and field. *Proceedings of the IEEE*, 1967.

[12] WC Dash and R Newman. Intrinsic optical absorption in single-crystal germanium and silicon at 77 K and 300 K. *Physical Review*, 99(4):1151, 1955.

[13] A Einstein. Über die von der molekularkinetischen Theorie der Wärme geforderte Bewegung von in ruhenden Flüssigkeiten suspendierten Teilchen. *Annalen der Physik*, 322(8):549–560, 1905.

[14] MA Green. Intrinsic concentration, effective densities of states, and effective mass in silicon. *Journal of Applied Physics*, 67(6):2944–2954, 1990.

[15] AS Grove. *Physics and Technology of Semiconductor Devices*. Wiley, New York, 1967.

[16] W Hänsch and M Miura-Mattausch. The hot-electron problem in small semiconductor devices. *Journal of applied physics*, 60(2):650–656, 1986.

[17] C Jacoboni, C Canali, G Ottaviani, and A Alberigi Quaranta. A review of some charge transport properties of silicon. *Solid-State Electronics*, 20(2):77–89, 1977.

[18] Y Katznelson. *An introduction to harmonic analysis*. Cambridge University Press, 2004.

[19] G Kramberger. *Signal development in irradiated silicon detectors*. PhD thesis, University of Ljubljana, 2001. Appendix F.

[20] GG Macfarlane, TP McLean, JE Quarrington, and V Roberts. Fine structure in the absorption-edge spectrum of Si. *Physical Review*, 111(5):1245, 1958.

[21] W Maes, K De Meyer, and R Van Overstraeten. Impact ionization in silicon: A review and update. *Solid-State Electronics*, 33(6):705 – 718, 1990.

[22] G Ottaviani, C Canali, and A Alberigi Quaranta. Charge carrier transport properties of semiconductor materials suitable for nuclear radiation detectors. *Nuclear Science, IEEE Transactions on*, 22(1):192–204, 1975.

[23] R Quay, C Moglestue, V Palankovski, and S Selberherr. A temperature dependent model for the saturation velocity in semiconductor materials. *Materials Science in Semiconductor Processing*, 3(1):149–155, 2000.

[24] S Ramo. Currents induced by electron motion. *Proceedings of the IRE*, 27(9):584–585, 1939.

[25] DJ Roulston, ND Arora, and SG Chamberlain. Modeling and measurement of minority-carrier lifetime versus doping in diffused layers of n+-p silicon diodes. *Electron Devices, IEEE Transactions on*, 29(2):284–291, Feb 1982.

[26] S Selberherr, W Hänsch, M Seavey, and J Slotboom. The evolution of the minimos mobility model. *Solid-state electronics*, 33(11):1425–1436, 1990.

[27] SE Swirhun, YH Kwark, and RM Swanson. Measurement of electron lifetime, electron mobility and band-gap narrowing in heavily doped p-type silicon. In *Electron Devices Meeting, 1986 International*, volume 32, pages 24–27, 1986.

[28] Synopsis TCAD. http://www.synopsys.com/Tools/TCAD/.

[29] SM Sze and KK Ng. *Physics of semiconductor devices.* Wiley, New York, third edition, 2007.

[30] Tektronix, Inc. Tektronix Serie 4000 Digital-Phosphor-Oszilloskope Benutzerhandbuch. http://www.tek.com/.

[31] W Treberspurg, T Bergauer, M Dragicevic, and B Lutzer. Analysis of test structures and process technology. HEPHY Vienna, 2013. Workshop on Silicon Strip Sensors for the CMS Phase II Upgrade.

[32] FN Trofimenkoff. Field-dependent mobility analysis of the field-effect transistor. *Proceedings of the IEEE*, 53(11):1765–1766, 1965.

[33] RN Williams and EM Lawson. The plasma effect in silicon semiconductor radiation detectors. *Nuclear Instruments and Methods*, 120(2):261 – 268, 1974.

Acknowledgements

First of all I would like to thank my mentor Robert Klanner for lots of time, help and very useful impulses. Then I would like to thank Joachim Erfle for lots of help mastering the computer part: ROOT, Ubuntu, and especially C++. Additionally I would like to thank Jörn Schwandt for providing the TCAD simulation and inside knowledge of silicon devices, and Eckhard Fretwurst for help with the CiS diode.

And of course I would like to thank Julian Becker for providing the code and a crash course of his simulation program. Many thanks also to Erika Garutti, Thomas Pöhlsen, Peter Buhmann, Michael Matysek, and all those people from the Uni Hamburg detector group who provided help and knowledge along the way. Special thanks to Moritz Habermehl for proofreading the thesis.

Finally, I would like to thank my wife Verena Raketa Buttmann-Scharf for her continuous support.

Hiermit bestätige ich, dass die vorliegende Arbeit von mir selbständig verfasst wurde und ich keine anderen als die angegebenen Hilfsmittel - insbesondere keine im Quellenverzeichnis nicht benannten Internet-Quellen - benutzt habe und die Arbeit von mir vorher nicht in einem anderen Prüfungsverfahren eingereicht wurde. Die eingereichte schriftliche Fassung entspricht der auf dem elektronischen Speichermedium. Ich bin damit einverstanden, dass die Master-Arbeit veröffentlicht wird.

Hamburg den 10.02.2014

Christian Scharf